/
Article / Book Information

( )	
Title(English)	Seismic Performance of Flexural Reinforced Concrete Walls with Confined Boundaries
( )	TALEB RAFIK
Author(English)	Rafik Taleb
( )	: ( ), : 10837 , :2018 3 26 , : , : , , , ,
Citation(English)	Degree:Doctor (Engineering), Conferring organization: Tokyo Institute of Technology, Report number: 10837 , Conferred date:2018/3/26, Degree Type:Course doctor, Examiner:,,,,
( )	
Type(English)	Doctoral Thesis

TOKYO INSTITUTE OF TECHNOLOGY

Seismic Performance of Flexural Reinforced Concrete Walls with Confined Boundaries

by

Rafik Taleb

Supervisor: Pr. Susumu Kono

A dissertation submitted in partial fulfillment of the requirements for the Degree of Doctor of Engineering

December 2017

ABSTRACT

Observed damages in reinforced concrete wall buildings following some recent earthquakes raised concerns about the seismic performance of rectangular RC walls with confined boundaries. A research program was developed to understand and improve the seismic behavior of reinforced concrete (RC) walls with confined boundary regions.

The research is divided into three phases: The first phase uses experimental research methods to evaluate the seismic performance of RC walls with confined regions. The first phase explored the effects of detailing of both transverse and longitudinal reinforcement, cross-section slenderness and loading type on the compressive confined strength, the damages and failure modes of rectangular RC prism members that simulate the boundary element of RC walls. Based on experimental results, design and detailing rules to prevent global buckling and reinforcement bar buckling in confined boundaries were evaluated. A longitudinal-to-transverse reinforcement index was proposed as an anti-buckling design rule for longitudinal reinforcement. The proposed longitudinal-to-transverse reinforcement index along with the ratio of transverse reinforcement spacing to longitudinal bar diameter present an effective anti-buckling measures of reinforcement. An analytical model that include bar buckling was also proposed to predict cyclic response of tested specimens. The analytical model captures reasonably well the measured response, and was able to predict the compressive strength reduction for specimens failing due to reinforcing bar buckling.

In the second phase, scaled RC structural walls designed to fail in flexure were tested under cyclic reversed loading to investigate the effects of end region shape and detailing in RC structural walls on the damage process, failure modes and deformation capacity. Primary test variables were cross sectional shape (rectangular and barbell shapes), transverse reinforcement ratio in confined end regions, shear span to wall length ratio, and axial load ratio. A fiber-based model was developed based on plastic hinge length and moment-curvature analysis to estimate the total lateral load-displacement hysteresis. The total lateral displacement of a RC wall was obtained by the summation of the flexural, the shear and the strain penetration displacements. The developed fiber model well simulated the hysteretic behavior of the tested wall specimens. The proposed model was compared with 2D and 3D finite elements (FE) models to simulate ultimate deformation under monotonic loading. The fiber-based model was able to provide relatively accurate backbone curves with very good estimation of ultimate drift and with less computational cost compared to FE analysis.

An analytical equation for RC wall ultimate displacement prediction was proposed and verified based on existing experimental results and fiber-based analysis. Key design parameters affecting displacement capacity were identified. It is demonstrated that

boundary transverse reinforcement, axial load, and wall length are the main affecting parameters. Based on proposed ultimate displacement equation, accuracy of existing plastic hinge length equations for ultimate displacement estimation were evaluated. Bohl and Adebar (2011) plastic hinge length equation for RC walls was modified to take effect of boundary transverse reinforcement into account. The modified equation was able to predict ultimate displacement with good accuracy compared to existing plastic hinge equations.

ACKNOWLEDGEMENTS

TABLE OF CONTENTS

LIST OF FIGURES

LIST OF TABLES

LIST OF SYMBOLS

Roman upper case letters

A_c	cross-sectional area of concrete gross section
A_{ch}	area of confined end region
A_g	concrete gross section area
A_l	longitudinal reinforcement area
A_s	cross-sectional area of longitudinal reinforcement
A_{sc}	area of longitudinal bars in compression
A_{st}	area of longitudinal bars in tension
A_t	transverse reinforcement area
A_w	areas of transverse reinforcement
D	wall length
E	Young's modulus of concrete
H	wall height
I	the second moment of inertia of the wall section
Mu	design moment
N	axial load
N_c	compressive load capacity
$_eN_{max}$	experimental peak load in prism element
$_sN_{max}$	simulated peak load of prism element without buckling effect
$_{sb}N_{max}$	simulated peak load of prism element with buckling effect
Q	is the lateral load
$_cQ_{mu}$	Calculated flexural capacity of wall
$_cQ_{su}$	Calculated shear capacity of wall
K	factor that accounts for the strength increase due to confinement
L_p	plastic hinge length
L_{sp}	strain penetration length
R	Drift angle
R_{ana}	analytical lateral drift
R_{exp}	experimental lateral drift
R_f	Flexural drift angle
V	shear force
Vu	Design shear

Roman lower case letters

a	shear span length
a_s	shear span-to-wall length ratio
a_t	area of longitudinal reinforcement in the wall boundary region
a_{wv}	area of longitudinal web reinforcement
b	Cross-section width
b_{cr}	critical wall boundary thickness
c	neutral axis depth
d	effective length of wall
d_b	longitudinal reinforcing bar diameter
d_t	transverse reinforcing bar diameter
f'_c	concrete compressive strength
f'_{cc}	the compressive strength of confined concrete
f_{it}	stress in the tension envelope corresponding to strain at the intermediate point

f_l	tensile strength orthogonal to the crack
f_{wv}	yield strength of vertical and horizontal web reinforcement
f_y	yield strength of reinforcement
f_{yh}	yield stress of transverse reinforcement
h_0	clear height
h_w	total wall height
j_d	lever arm between compression and tensile resultants
j	lever arm length
l	Cross-section length
l_p	the plastic hinge length
m	mechanical reinforcing ratio
p	ratio of wall area to floor-plan area
p_{te}	equivalent tensile reinforcement ratio
p_{wc}	boundary longitudinal reinforcement area ratio
p_{wh}	horizontal web reinforcement ratio
p_{wv}	vertical web reinforcement ratio
s	transverse reinforcement spacing
t_e	equivalent wall thickness
t_w	wall thickness

Greek letters

Δf	Flexural displacement
Δfe	elastic component of the flexural displacement
Δfp	plastic component of the flexural displacement
Δ_s	Shear displacement
Δsp	displacement due to strain penetration
α	coefficient that takes into account strain hardening in reinforcing bars
α	Kato's transverse reinforcement index
β	effective depth parameter for longitudinal reinforcement
β	crack angle
δu	roof displacement expected under the design earthquake
ε_{cu}	Ultimate concrete compressive strain
ε_i	strain at the intermediate point
ε_m	axial strain at the center of the wall section
ε_{nom}	nominal axial strain
ε_{sc}	current compressive strain of reinforcing bar
ε_{sm}	maximum tensile strain prior to compressive load
ε_{sm}	the fracture strain of confining reinforcement
ε_y	Reinforcing bar yielding strain
ϕ	curvature of the wall section
ϕ_p	plastic curvature
ϕ_y	the yield curvature
η	axial load ratio
ρ_l	longitudinal reinforcement ratio
ρ_s	volumetric ratio of transverse reinforcement in confined end regions
ρ_t	transverse reinforcement ratio
σ_0	average axial stress for gross cross-sectional area
σ_t	stresses in the tension envelope corresponding to current compressive strain

ξ parameter related to mechanical reinforcement ratio

PUBLICATIONS AND PRESENTATIONS

Taleb, R., Watanabe, H., Kono, S., (2018), Numerical Study on the Ultimate Deformation of RC Structural Walls with Confined Boundary Regions, Periodica Polytechnica Civil Engineering: 62(1): 191-199

Netrattana, C., *Taleb, R.*, Watanabe H., Kono, S., Mukai, D., Tani, M., Sakashita, M, (2017), Assessment of Ultimate Drift Capacity of RC Shear Walls by Key Design Parameters, Bulletin of the New Zealand Society for Earthquake Engineering 50(4): 482-493.

Taleb, R., Tani, M., Kono, S., (2016), Performance of Confined Boundary Regions of RC Walls under Cyclic Reversal Loadings, Journal of Advanced Concrete Technology: 14(4): 108-124.

Netrattana C., *Taleb R.*, Watanabe H., Kono S., Mukai D., Tani M., Sakashita S., "Assessment of ultimate Drift Capacity of RC Shear Walls by Key Design Parameters", 19th Taiwan-Japan-Korea Joint Seminar on Earthquake Engineering for Building Structures (SEEBUS 2017), Korea,

Netrattana C., *Taleb, R.*, Watanabe, H., Kono, R., (2016), "Parametric Study on Drift Capacity of RC Shear Walls. Part 1: Validation of Fiber Model", Architectural Institute of Japan Annual Convention (AIJ2016), 24-26 August, Fukuoka, Japan.

Taleb, R., Netrattana C., Watanabe, H., Kono, R., (2016), "Parametric Study on Drift Capacity of RC Shear Walls. Part 2: Parametric Study", Architectural Institute of Japan Annual Convention (AIJ2016), 24-26 August, Fukuoka, Japan.

Taleb, R., Sakashita, M., Kono, S. (2015), "Ultimate Deformation of Reinforced Concrete Structural Walls with Confined Boundaries", 13th Arab Conference on Structural Engineering (13ASEC), 13-15 December, Blida, Algeria.

Taleb, R., Kono, S., Sakashita, M., Tani, M., (2014), "Effects of Boundary Regions Confinement on the Seismic Performance of Flexural RC Structural Walls", 2nd European Conference on Earthquake Engineering and Seismology (2ECEES), 25-29 August, Istanbul, Turkey.

Taleb, R., Kono, S., Tani, M., Sakashita, M., "Effect of End Region Confinement on Seismic Performance of RC Cantilever Walls", 10th U.S. National Conference on Earthquake Engineering (10NCEE), July 21-25, 2014, Anchorage, Alaska.

Taleb, R., Ogura, M., Kono, S., Tani, M., (2014), "Performance of Confined boundary regions of RC rectangular Walls under cyclic reversal loadings", Proceedings of the Annual Convention of the Japan Concrete Institute (JCI 2014), July 9-11, Takamatsu,

Japan.

Taleb, R., Kono, S., (2013), "Nonlinear Finite Element Analysis of Reinforced Concrete Cantilever Structural Walls under Lateral Loading", Architectural Institute of Japan Annual Convention (AIJ2013), Aug. 30 - Sep. 1, Sapporo, Hokkaido, Japan.

CHAPTER 1 INTRODUCTION

1.1. Background

Reinforced concrete structural walls are commonly used as primary lateral-load resisting system in medium and high-rise buildings located in earthquake-prone regions. RC Structural walls have a high in-plane stiffness that contribute in decreasing structural damage by limiting the inter-story drift during seismic events. The superior performance of buildings with RC structural walls in past earthquakes is well documented in the literature. During the 1985 Chilean earthquake, buildings in which lateral force resistance was provided by structural walls showed excellent performance (Wood *et al.*, 1987), although detailing requirements for the Chilean wall system as of 1985 were less strict compared to those of the US or Japan. In addition, during the 1988 Armenia earthquake, it was observed that even poorly designed and constructed buildings that incorporated concrete walls as the main lateral force resisting system performed substantially better than buildings built with other structural systems (Wyllie and Filson, 1989). Even during the most damaging earthquakes of recent times (e.g., 1994 Northridge earthquake in California, the 1995 Kobe earthquake in Japan, and the 1999 Kocaeli earthquake in Turkey), which altered the engineering community's view towards the earthquake engineering, no building incorporating shear walls as lateral load resisting system, collapsed. Further detailed literature review on previous performance of RC walls is presented in references (Fintel 2002, Holden *et al.* 2003).

When properly designed and detailed to meet current code requirements, RC walls are expected to behave in a ductile flexural manner to resist high seismic demands. This

expected behavior is based on the practice of detailing reinforced concrete structural walls to be tension-controlled. To achieve this goal, lateral instability, fracture or buckling of longitudinal reinforcement should be prevented (Paulay 1986).

A common practice in the design of structural walls in Japan and some other countries is the use of barbell shape cross sections with confined boundary columns that can carry a large amount of axial load. However, modern architecture and design practices promoted the use of slender rectangular walls with the confidence that these planar walls with uniform wall thickness can insure adequate ductility when designed to current code requirements.

However, following the 2010 Chile and the 2011 New Zealand earthquakes, observed damages in RC wall buildings raised concerns about the seismic performance of rectangular RC walls. In these earthquakes, severe damages happened to RC walls in numerous walled buildings leading to partial or total collapse (Kato *et al.* 2010, Moehle *et al.* 2010) indicating that the behavior of RC structural walls may not meet design assumptions. Reconnaissance missions following these earthquakes reported that RC Wall damage included spalling and crushing of concrete at boundaries that often spread over the entire wall width, buckling of longitudinal reinforcement under compression and fracture under tension at boundaries (Westenenk *et al.* 2012, Wallace *et al.* 2012). Global wall buckling was also observed in some damaged buildings. These observations suggest that additional research is needed to address issues related to RC walls failures observed following these recent earthquakes as well as the actual seismic design provisions for RC structural walls.

This thesis deals with the effects of confined boundaries detailing of RC walls on their seismic performance. The results of a two-phase experimental program. The first phase includes uniaxial test of sixteen (16) reinforced concrete rectangular prisms that are intended to simulate the confined boundary regions of RC structural wall with behavior dominated by flexure. The second phase includes cyclic testing of seven (7) 40%-scale RC wall specimens with different cross sectional shape (rectangular and barbell shape).

1.2. Scope and objectives

The purpose of this research is to investigate and improve the compressive performance of boundary elements of RC structural walls through both experimental testing and analytical simulation. The specific research objectives are to:

- Evaluate the compressive performance of reinforced concrete rectangular sections that simulate boundary elements within reinforced concrete seismic structural walls, and develop new design recommendations for boundary element detailing to better meet the expectations and suppress undesirable failure modes;
- Investigate the influence of different confined boundary elements detailing on the cyclic lateral load behavior of reinforced concrete structural walls;
- Using a developed fiber based analytical program, study the analytical response of the tested RC walls under cyclic lateral loading. Analytically quantify the deformation contributions due to flexure, shear, strain penetration and comparing them with the respective components obtained experimentally.
- Evaluate ultimate displacement capacity of the tested walls and comparison with the results of Finite Element Method (FEM). This investigation will be of greater interest for the development of performance-based engineering for structural systems with structural walls.
- Analytical evaluation of displacement capacity and plastic hinge length at ultimate and comparison with existing experimental data.

1.3. Thesis outline

This thesis consists of six chapters including the general introduction presented in this chapter. The following chapter reviews the available literature on previous studies relevant to the investigation of RC confined boundary elements and RC structural walls. Various modeling and analysis techniques that have been used to analyze structural walls are also summarized in this chapter.

Chapter 3 presents the experimental study on the behavior of confined boundary regions in RC structural walls subjected to lateral loading. Sixteen (16) RC prism elements that idealize confined boundaries of RC walls were tested to investigate the influence of longitudinal and transverse reinforcement detailing, cross-section slenderness and

3

loading type (monotonic and cyclic) on their compressive capacity, damage process and failure modes. It was found that the tensile strain prior to compressive strain affected the performance of thin wall boundaries and may lead to different failure modes when subjected to cyclic loading. It was also found that dense transverse reinforcement detailing in thin confined boundaries did not improve their compressive capacity.

Chapter 4 presents analytical and numerical studies on confined boundary elements. A longitudinal-to-transverse reinforcement index was proposed as an anti-buckling design rule for longitudinal reinforcement. The longitudinal-to-transverse reinforcement index along with the ratio of transverse reinforcement spacing to longitudinal bar diameter present a simple but effective anti-buckling measures of reinforcement.

A numerical model that takes into account buckling of reinforcement was proposed to simulate response curves of cyclically tested specimens. The model showed the influence of reinforcement buckling behavior on reducing the compressive capacity for elements with buckling of reinforcement failure.

In Chapter 5, experimental study under cyclic reversed loading was conducted on seven 40%-scale RC structural walls designed to fail in flexure. Considered walls included two walls with barbell shape section and five walls with rectangular cross-section and having different transverse reinforcement ratio at their confined end regions. Primary test variables were cross sectional shape (rectangular and barbell shapes), transverse reinforcement ratio in confined end regions, shear span-to-wall length ratio, and axial load ratio. The main objective of this study was to investigate the effects of end region detailing of RC structural walls on their seismic performance. Test results showed that concrete crushing spread widely over the plastic hinge region with buckling of longitudinal reinforcement at final loading stage for rectangular walls, while for walls with barbell shape, crushing of concrete was essentially limited within boundary columns but leading to a more brittle failure than that of rectangular walls. Walls with barbell-shape showed the efficiency of boundary columns in increasing deformation capacity and reducing damage level in the wall panel. It was also shown that the damage region was limited in height and tends to spread more horizontally toward wall center. Test results also made clear that end regions should be well confined when a structural wall, especially rectangular walls, is expected to sustain large deformation.

A fiber-based sectional analysis based on the plastic hinge length and moment-curvature analysis is proposed to simulate lateral load-displacement hysteresis for flexure, shear and strain hardening. The total top displacement of a RC wall is obtained by the sum of three displacement components: the flexural and shear displacements of the wall as well as the displacement due to strain penetration in the form of fixed-end rotation of the wall base.

Chapter 6 "Numerical Study on Ultimate Deformation and plastic hinge length of RC Structural Walls with Confined Boundary Regions", numerical investigations were carried out on barbell and rectangular RC walls with confined boundaries to evaluate response curves and ultimate deformations. A nonlinear 2D and 3D finite elements (FE) models were built in order to simulate the load-deformation relations under monotonic loading as well as cracking and damage patterns of previously tested walls. The FE models were able to simulate the backbone curves with good accuracy as well as the ability of boundary columns in reducing damage level. The 3D FE model simulated very well the ultimate deformation compared to 2D models. A fiber-based model combined with plastic hinge length and shear displacement component is proposed in order to simulate the backbone curves and the ultimate displacement with less computational cost compared to 3D FE analysis. The model was able to provide relatively accurate backbone curves with very good estimation of ultimate drift.

An analytical equation for RC wall ultimate displacement prediction was proposed and verified based on existing experimental results and fiber-based analysis. Key design parameters affecting displacement capacity were identified. It is demonstrated that boundary transverse reinforcement, axial load, and wall length are the main affecting parameters. Based on proposed ultimate displacement equation, accuracy of existing plastic hinge length equations for ultimate displacement estimation were evaluated. Bohl and Adebar (2011) plastic hinge length equation for RC walls was modified to take effect of boundary transverse reinforcement into account. The modified equation was able to predict ultimate displacement with good accuracy compared to existing plastic hinge equations.

Finally, Chapter 7 "Conclusions and Recommendations" summarizes the main results stated in each chapter and the conclusions obtained from this research. In addition, some suggestions for seismic design of RC walls and for future works are stated.

References

1. Fintel, M., "Performance of Buildings with Shear Walls in Earthquakes of the Last Thirty Years", *PCI Journal*, 2002, Vol. 40, No. 3, pp. 62-80.

2. Holden, T., Restrepo, J., and Mander, J. B. (2003), "Seismic Performance of Precast Reinforced and Prestressed Concrete Walls". *ASCE structural Journal*, 2003.

3. Kato, H., Tajiri, S. and Mukai, T., (2010). "Preliminary reconnaissance report of the chile earthquake 2010", Building Research Institute, Japan.

4. Moehle J., Berger J., Bray J., Dengler L., Greene M., Mitrani-Reiser J. and Siembieda W., (2010). "The 27 February 2010 central south Chile earthquake: emerging research needs and opportunities", Earthquake Engineering Research Institute.

5. Paulay, T., (1986). "The design of ductile reinforced concrete shear walls for earthquake resistance", *Earthquake Spectra*, (4), 783–823.

6. Wallace J. W., Massone L. M., Bonelli P., Dragovich J., Lagos R., Lüders C. and Moehle J., (2012). "Damage and implications for seismic design of RC structural wall buildings", *Earthquake Spectra*, 28(S1), S281–S299.

7. Westenenk B., Llera J. C., Besa J. J., Jünemann R., Moehle J., Lüders C., Inaudi J. A., Elwood K. J. and Hwang S. J., (2010). "Response of reinforced concrete buildings in concepción during the Maule earthquake", *Earthquake Spectra*, 28(S1), S257–S280.

8. Wood, S. L., Wight, J. K., & Moehle, J. P. (1987). "1985 Chile Earthquake – Observations on Earthquake-Resistant Construction in Vina Del Mar". In *Civil Engineering Studies, Structural Research Series (University of Illinois at Urbana-Champaign*.

9. Wyllie, L.A. and Filson, J.R., Armenia Earthquake Reconnaissance Report, *Earthquake Spectra*, Special Supplement, 1989.

CHAPTER 2 LITERATURE REVIEW

2.1   Introduction

This research project was initiated following observations on the seismic performance of RC walls in recent earthquakes that have demonstrated the vulnerability of RC rectangular walls. The research was undertaken to study the influence of confinement details in wall boundary on strength and deformation of structural RC walls. In particular, there is concern about the compressive response of confined boundary elements of flexural RC walls. This chapter is organized into three main parts:

- Review of performance of RC walls in recent earthquakes;
- Review of experimental testing on structural RC walls and wall boundary elements;
- Review of actual design practices for RC walls.

Prior research is presented and discussed with focuses on the existing experimental testing on rectangular and barbell shape reinforced concrete walls as well as prism compression members simulating confined boundary regions. The objective of this review is to ensure that the experimental research program does not duplicate existing tests, and to identify gaps in the literature.

2.2   Performance of structural RC walls in recent earthquakes

2.2.1.   Observation of structural RC Wall Damage following Chile (2010) earthquake

The majority of large buildings in Chile are constructed using reinforced concrete structural wall systems. Figure 2.1 shows an example of typical walled buildings in Chile (EERI, 2010). This type of building layout resulted in asymmetric (i.e., T-shaped or L-shaped) wall sections that were often under 20cm thick due to the lower demands (i.e., shear and axial load) in a more redundant system as compared with a core-wall type

structure. Asymmetric wall sections are typically associated with larger compression demands due to unbalanced normal forces and higher extreme strains.

The 2010 Chile earthquake resulted in severe damage to concrete walls in numerous buildings; some walled buildings collapsed partially or completely. This widespread damage to concrete walls has left some interrogations about the design and the expected performance of RC walls for earthquake loading designed in compliance with modern seismic design codes. Numerous buildings exhibited apparent compression failures in the lower floors "transverse" walls. These failures typically included crushing of the concrete core along the full length of the wall, as well as longitudinal bar buckling or bar fracture. Examples of this failure mechanism are shown in Figure 2.2 and Figure 2.3.
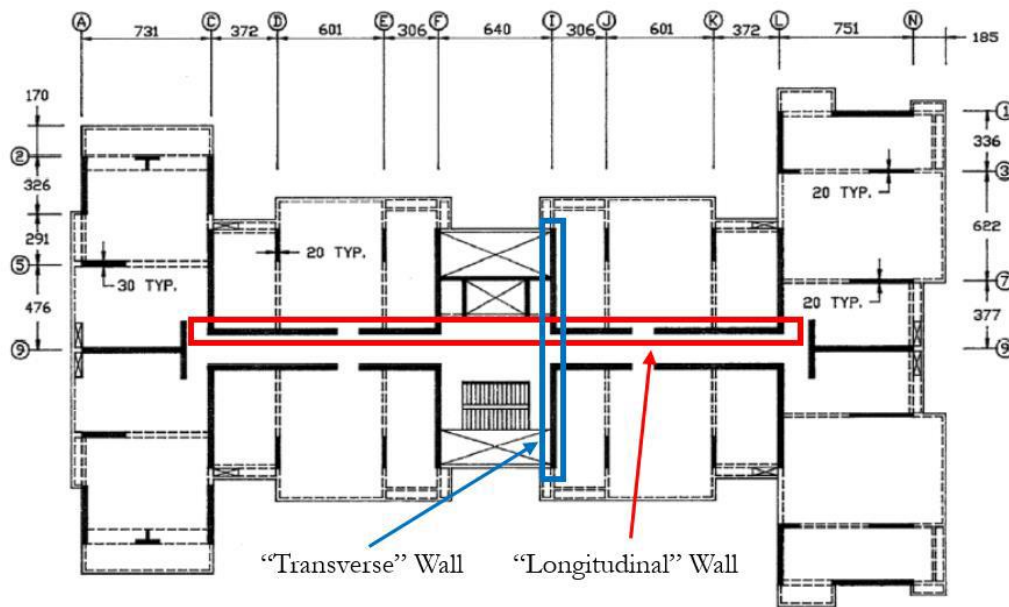
Figure 2.1 – Typical floor plan layout of Chilean walled buildings (Wallace, 2011).

The final damage state consistently appears to be a combination of core crushing and bar buckling, as shown in the additional photos in Figure 2.4. This observation suggests a strong relationship between the strength/deformation capacity of structural walls, and the stability of the longitudinal reinforcement and the integrity of the confined core.

(a) Out-of-plane buckling   (b) Concrete crushing over wall width

(c) Reinforcement fracture   (d) Concrete crushing and reinforcement buckling

Figure 2.2 - Typical walls damage in the 2010 Chile earthquake (Wallace *et al.* 2012)

(a) Credit : J. Wallace   (b) Credit :J. Dragovich

Figure 2.3 - Wall damage in Santiago, Chile (NEEShub Database)

(a) Credit : F. Naeim   (b) Credit : F. Naeim
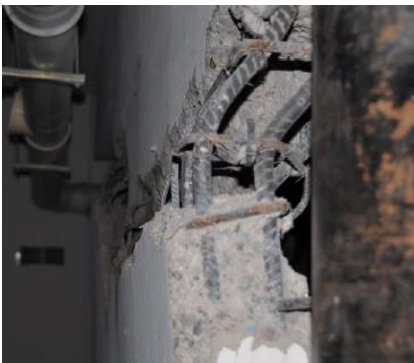
(c) Credit : J. Dragovich   (d) Credit : J. Moehle
Figure 2.4 - Chilean wall damage

Some damaged walls appeared to exhibit evidence of large tensile strains prior to compressive failures. Large tension cycles near the extreme boundary fibers of a wall typically result in significant horizontal cracking and yielding of longitudinal reinforcement, which may result in reducing wall compressive capacity (Wallace *et al.*, 2012). An example of this behavior is shown in Figure 2.5.

Figure 2.5 - Wall damages with evidence of large tensile strains prior to compressive failures (NEEShub Database)

Research on construction practice trends in Chile (Massone, *et al.* 2012) identified an important trend for mid-rise and high-rise RC wall buildings: while average building heights have increased over the past few decades, the ratio of wall area to floor plan area has remained relatively constant, cross-sections have become thinner, and axial stress ratios have increased. Based on the extent of damage observed in Chile and New Zealand, it is likely that performance limits for slender walls have been reached by current design and construction practice. It is important to understand the behavior limitations of walls designed for large ductility demands.

2.2.2. Observation of structural RC Wall Damage following Christchurch, New Zealand (2010, 2011) earthquakes

The majority of buildings over four stories in Christchurch are reinforced concrete construction, typically using moment-frames or structural walls as the primary lateral-load resisting systems. These structures performed as intended during the earthquake, with the exception of a few compression failures. Failure examples are shown in Figure 2.6.

Figure 2.6 - Damage to reinforced concrete structural wall in Christchurch (Credit: Elwood)

The compression damage was extensive although walls have been properly detailed based on the existing requirements of the New Zealand concrete construction code (NZS 3101-1, 2006). The report specifically identified the lower floor of five to fifteen-story buildings as exhibiting the majority of compression failures. Figure 2.7 shows damage to an L-

shaped wall, where the ends experienced large tensile and compressive strains, due to its configuration, resulting in a compression failure mode.
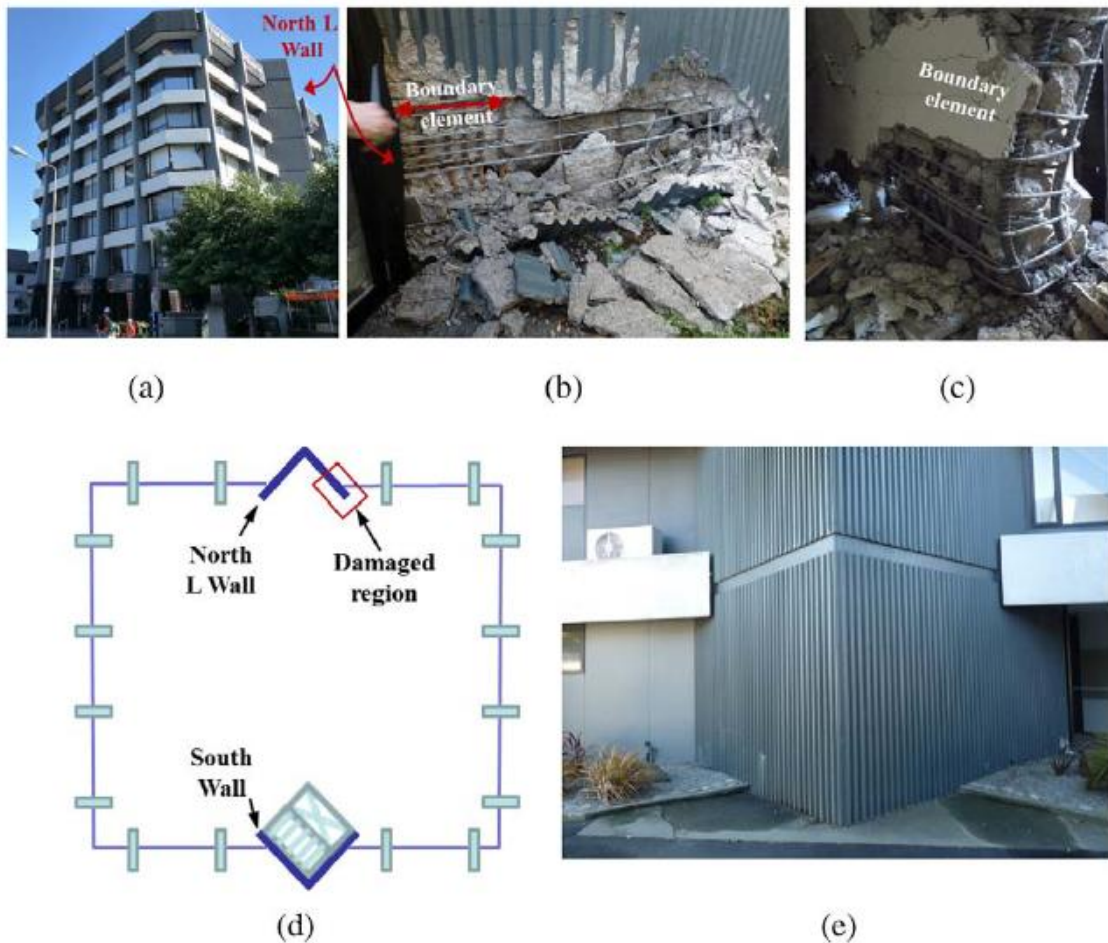
Figure 2.7 - A seven-story office building with wall damage. (a) Overall view; (b) damaged north L wall; (c) close-up of buckled region; (d) plan view (after Elwood 2011); (e) undamaged south L wall. (Sritharan *et al.*, 2014) (Credit: Elwood)

2.3 Previous experimental studies on RC confined boundaries Members (Prism test)

As the boundary element region primarily resists the flexural demands within a structural wall through tension and compression loading, uniaxial testing of rectangular reinforced concrete prism specimens were used to simulate the compressive performance of boundary elements. To better understand the prior literature on boundary elements, test data were collected and reviewed. The prism specimens were typically assumed to simulate the compressive boundary element region of a structural wall.

In the literature, detailing are usually classified based on the level of compliance with the requirements for boundary elements in special reinforced concrete structural walls

12

prescribed in ACI 318 (ACI 318-11 and ACI 318-14). ACI 318 provisions classify boundary elements into two categories: ordinary boundary elements (OBE) that meet the minimum requirements, and special boundary elements (SBE) that meet the requirements for special boundary elements within special reinforced concrete structural walls.

2.3.1. Chai and Elayer, (1999)

An experimental study was conducted by Chai and Elayer (Chai and Elayer, 1999) to examine the out-of-plane stability of reinforced concrete columns under large amplitude reversed cyclic tension and compression. The columns were designed to represent the end-regions of a ductile planar reinforced concrete wall (Figure 2.8).
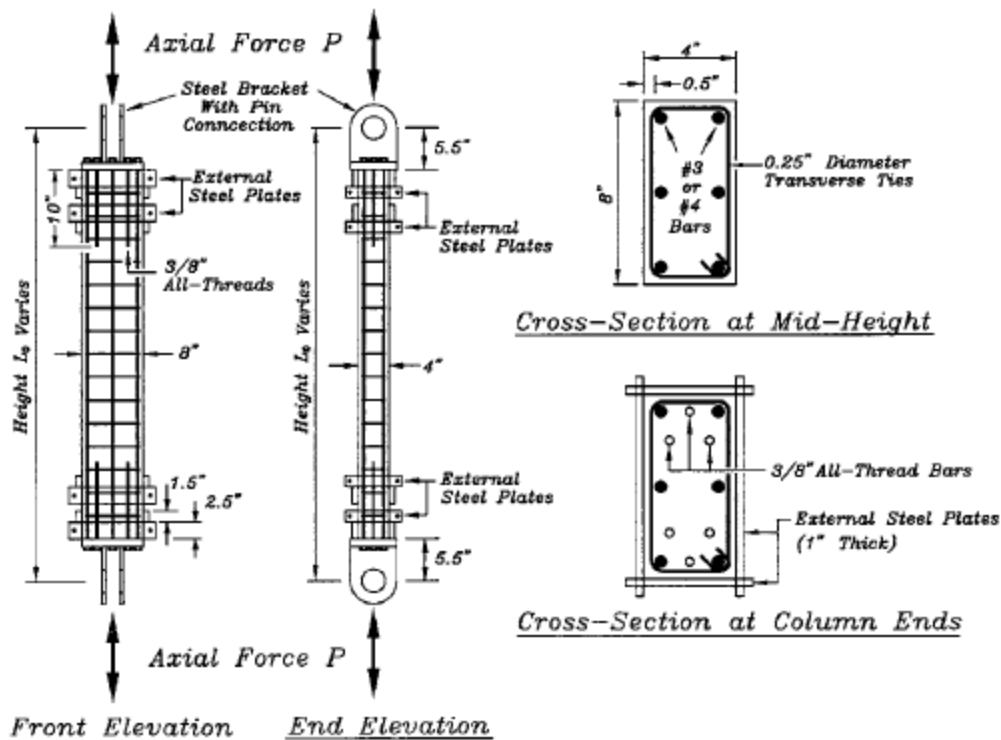
Figure 2.8 - Reinforcement details for test specimens by Chai and Elayer (1999) (1 in. = 25.4 mm).

The loading protocol for the test column imposed first a tensile half-cycle followed by a compression half-cycle with a compressive strain targeting about one seventh of the tensile strain amplitude. Amplitudes of the axial strain in the tensile half-cycle were 0.0078, 0.0108, 0.0133, and 0.0161. For axial tensile strains less than or equal to 0.0133, the test column was stable and it was able to fully develop the compressive force of 0.0161, however, significant out-of-plane displacement developed in the compression half-cycle, leading to column buckling. The stable column response following a tensile strain of 0.0133 can be seen in Figure 2.9(a), while the buckled column after a tensile strain of 0.0161 is shown in Figure 2.9(b).

13

The study confirmed the critical influence of the maximum tensile strain on the lateral stability of these members. Wide cracks developed resulting fro large yield excursion that must close before the compressive capacity of the column can be fully developed. A critical condition exists prior to closing of the cracks where an excessive out-of-plane displacement may occur, causing the column to become unstable. Photographs in Figure 2.8 show the condition of a reinforced concrete column under large tension/compression cycles. Thus, the tensile strain amplitude must be recognized as an important parameter governing the cyclic stability of reinforced concrete structural walls.
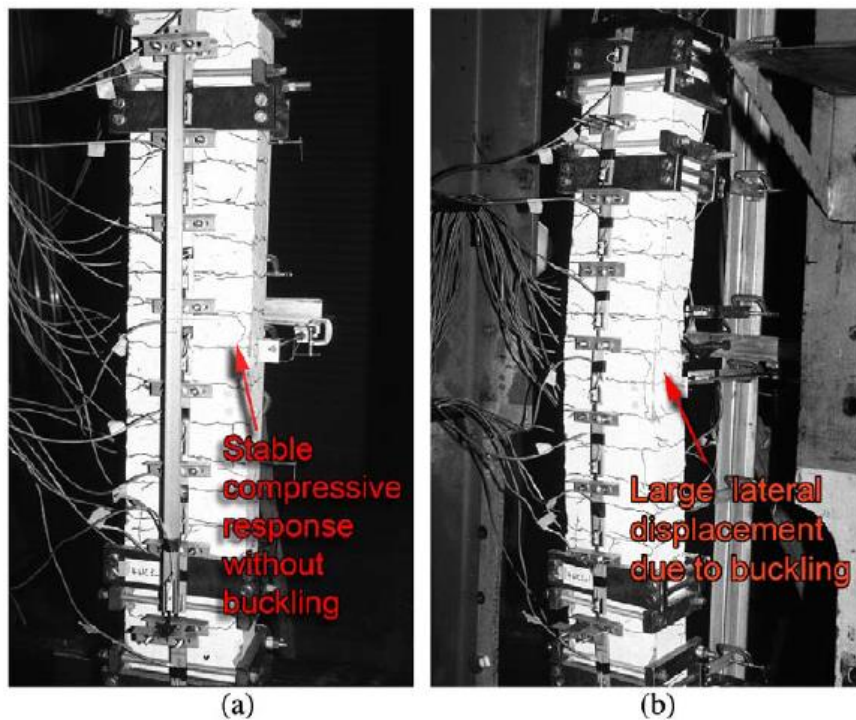
Figure 2.9 - Stability of a reinforced concrete column under tensile/compression cycles: (a) Stable compressive response up to $\varepsilon_a = 0.0133$ (b) unstable compressive response after $\varepsilon_a = 0.0161$ (Chai and Elayer, 1999).

2.3.2. Acevedo (2010)

An experimental study was carried out by Acevedo (2010) to study the effect of axial load reversals on boundary elements that meet the minimum ACI 318-08 provisions for ordinary boundary elements reinforced concrete structural walls. These boundary elements were similar to those of Chilean walls, which is representative of the detailing requirements in the Chilean code that was up-to-date at the time. The author assert that walls designed to barely meet ACI 318-08 provisions may experience similar damage behavior under seismic loads.

The experimental study included two rectangular reinforced concrete prism specimens (NS1 and NS2) intended to simulate the boundary elements of reinforced concrete structural walls.

14

The specimens measured about 15cm wide by 30cm long, with a clear height of about 90cm. The dimensions were intended to prevent out-of-plane instability of the specimen, and instead focus on any strength loss due to prior tension cycles. For each specimen, the vertical reinforcement ratio was 3.67%, and the transverse reinforcement consisted of #3 bars spaced at 20cm, for transverse reinforcement ratio of 0.6%.

Both specimens were subjected to uniaxial compressive load until failure, however specimen NS1 was loaded in tension to a strain of 4% prior to compression loading. During the tension excursion of specimen NS1, cracking occurred coincident with the transverse reinforcement spacing, eventually becoming closer than 20cm spacing as the tensile strain reached 4%. This limit tensile strain was selected based on multiplying an assumed wall drift capacity of 2% by an assumed plastic hinge length equal to one-half the wall length. The results indicate the significance of prior large tensile strain excursions on the performance of the section under compression. Figure 2.10(a) and Figure 2.10(b) show the failure modes of the two wall specimens, and Figure 2.11 shows the load-deflection results from the uniaxial compression tests. As shown, specimen NS1 exhibited compressive strength of only 20% that of NS2.

(a) NS1 (b) NS2
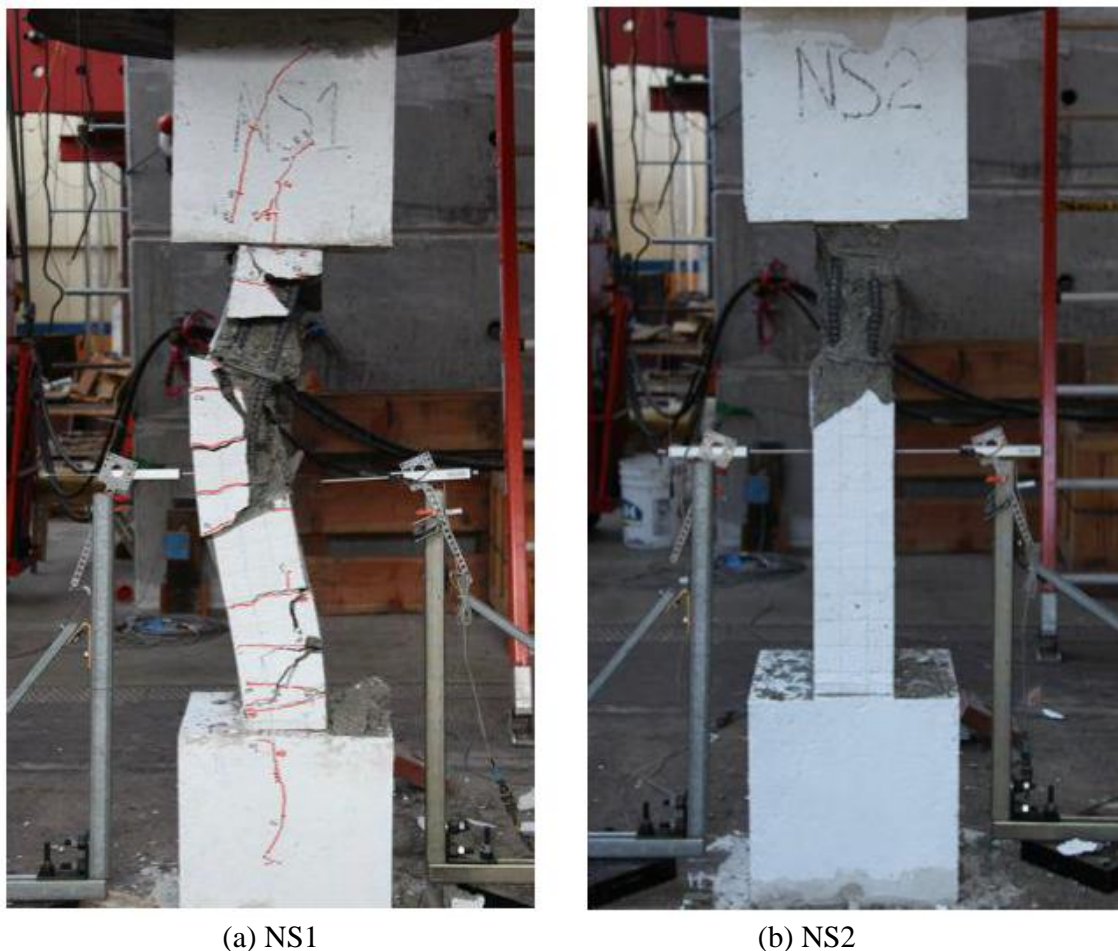
Figure 2.10 - Failure Mechanisms of Specimens (a) NS1 (Pre-Strain of 4%), and (b) NS2 (Acevedo, 2010)

15
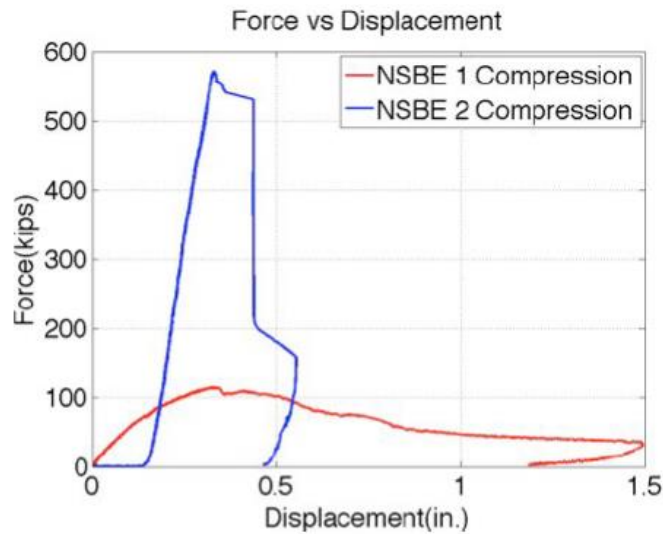
Figure 2.11 - Load-Deflection Compression Response of Test Specimens (Acevedo, 2010)

2.3.3. Creagh *et al.*, (2010)

Research was conducted by Creagh *et al.* (2010) in response to the compression damage in structural walls following the 2010 Chile earthquake. This study focused on the boundary elements of slender reinforced concrete walls, designed in accordance with the ACI 318-08 requirements for special boundary elements within special structural walls. The specimens were intended to be a comparison of special boundary performance (as detailed by ACI 318-08) to that of the detailing requirements in the Chilean code (NCh430.Of2008, which does not require special boundary elements (Acevedo *et al.*, 2010).

Two 15cm by 30cm test specimens (S1 and S2) were constructed with the same transverse and longitudinal reinforcement patterns, and were longitudinally reinforced with six (6) #6 bars (3.67%), and confined with #3 transverse bars at 5cm spacing. All bars were restrained; the outer bars were restrained with a continuous hoop, while the intermediate bars were restrained by a 90°-135° crosstie, as recommended in the code. A representative cross-section is shown in Figure 2.12.

16
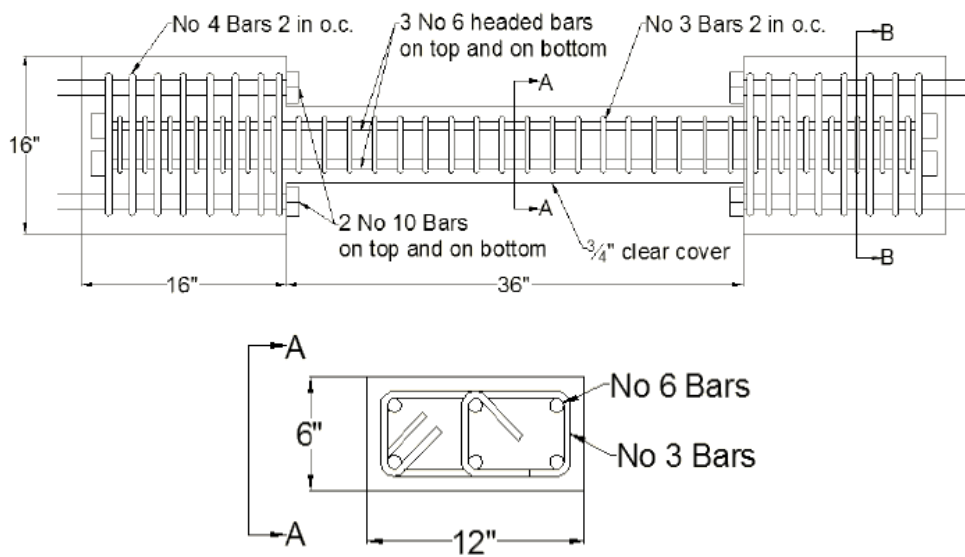
Figure 2.12 - Plan view and Cross-section of boundary element specimen [21]

Each specimen was tested to failure in compression, however Specimen S1 was first loaded in tension to 4% strain. Major horizontal cracks were spaced approximately equal to the section thickness. Additional cracking was coincident with the horizontal tie spacing of 5cm. The failure progression for specimen S1 is shown in Figure 2.13. A large vertical crack through the center of the section was followed immediately by overall section buckling. The authors noted that bar buckling within the transverse ties did not appear to be a factor, moreover the entire section buckled over at least half of the height of the specimen. Specimen S2, tested in compression only, surprisingly also failed in a brittle manner, consisting of overall section buckling at the top of the specimen, as shown in Figure 2.14.

Figure 2.13 - Failure progression of Specimen S1 (Compression Loading after 4% Tensile Excursion) (Creagh *et al.*, 2010)

17
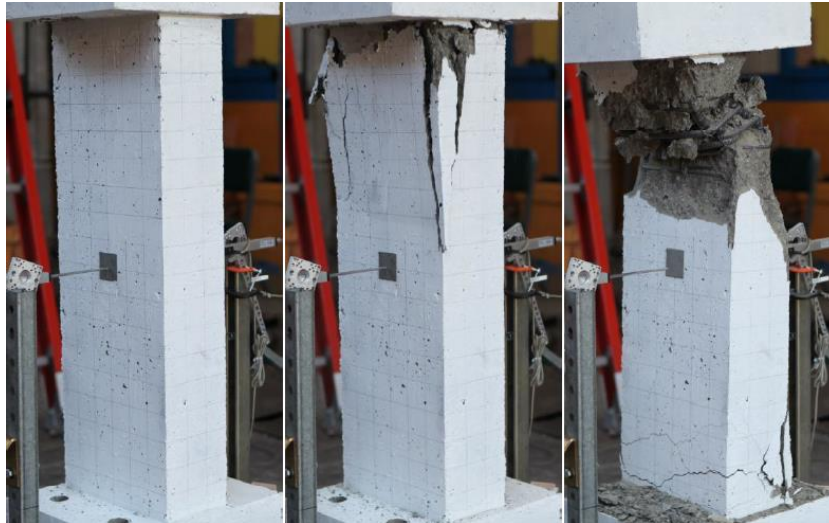
Figure 2.14 - Failure Progression of Specimen S2 (Compression Loading Only) (Creagh *et al.*, 2010)

Specimen S1 experienced a significant loss in compressive strength due to the previous tension excursion. As shown in Figure 2.15, the compressive capacity of specimen S1 was approximately 1/3 of the compressive capacity of Specimen S2. Although these specimens met the requirements for special boundary elements per ACI 318-11, they are considered ordinary boundary elements according to ACI 318-14.
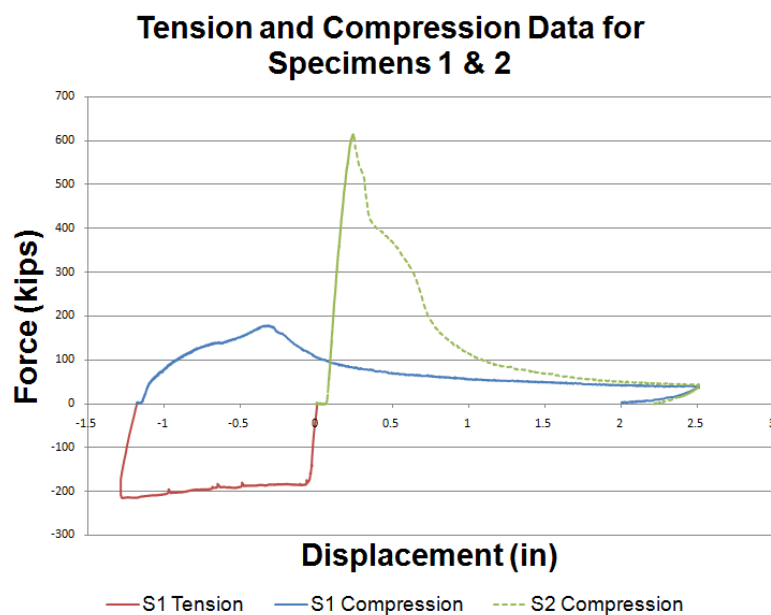
Figure 2.15 - Force-Displacement Results for Specimens S1 and S2 (Creagh *et al.*, 2010)

18

2.3.4. Chrysanidis and Tegos, (2012)

Chrysanidis and Tegos (2012) performed a suite of tests aimed at identifying the effect of tensile strain prior to significant compressive loading on the compressive performance of rectangular reinforced concrete prism members intended to represent boundary elements within structural walls.

The experimental program consisted of five (5) identical specimens of approximately 7.5cm thick, 15cm wide, and with an unbraced height of 76cm. The major axis transverse reinforcement ratio was 0.4%, and the spacing to bar diameter s/d_b ratio was 10.5 (Figure 2.16). The concrete compressive strength was 24.9MPa, and the yield strength of the longitudinal and transverse reinforcement was 604MPa. The first specimen, which served as a reference, was loaded solely in monotonic compression, while the other four specimens were subjected to tensile strains of 1%, 2%, 3% and 5% prior to monotonic compression loading to failure.
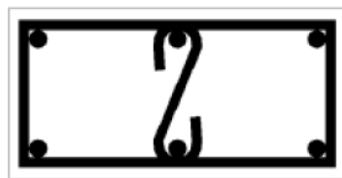
3 in. x 6 in.
$\varrho_2 = 0.4\%$
$s/d_b = 10.5$
$h_x = 2.5$ in.

Figure 2.16 - Representative Cross-Section Detail Configuration by Chrysanidis and Tegos (2012)

Figure 2.17 shows the compressive response of all five (5) specimens. In the figure, the x-axis is denoted as "normalized shortening", as a percentage of the overall specimen height (corresponding to 1/10 of average strain). The results of the suite of tests indicated that tensile strain prior to significant compression loading has an effect on compressive strength if the plastic pre-strain excursions exceed 3%.

19
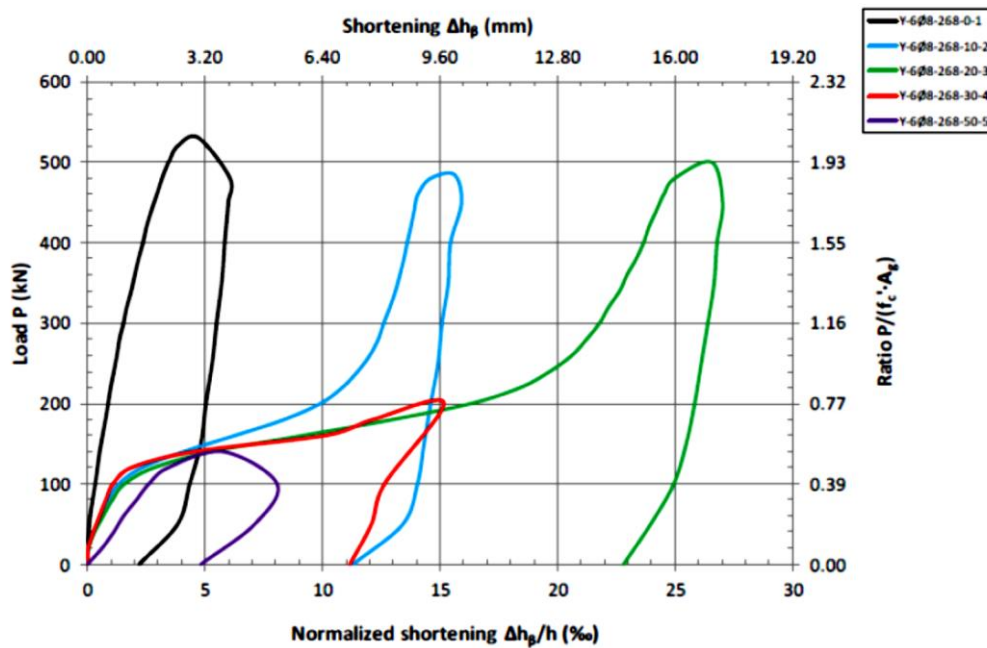
Figure 2.17 - Compressive Response of Specimens of Varying Tensile Pre-Strain Excursions by Chrysanidis and Tegos (2012)

2.3.5. Massone *et al.*, (2014)

Massone *et al.* (2014) conducted a series of tests in response to the compression failures observed following the 2010 Maule earthquake in Chile. The study attempted to reproduce the failures observed following the earthquake. Parameters of interest included thickness, quantity and configuration of the confining reinforcement, and tensile strain prior to compression loading.

Twenty-four specimens were built and tested using two protocols: one corresponds to a pure compression test and the other one consisted of a tensile strain (pre-strain) applied prior to the compression test. The specimens were 0.3m long, 1.0 and 1.6m height, and 0.13m, 0.25m and 0.18m thick and considered different confinement configurations (Figure 2.18). Depending on the confinement type, these specimens had 6 or 8-18mm diameter rebars, while all stirrups were 8mm in diameter. The test matrix is shown in Figure 2.18. All specimens had a central area with an average length of 400mm, where it is expected to concentrate most of the damage, and whose transverse reinforcement configuration changes from one specimen to another.

The results of the tests indicated that neither the cross-sectional aspect ratio nor the amount of confining steel had a substantial effect on compressive strength. Note that all specimens had a cross-sectional aspect ratio of 1.7, with the exception of P1 and P4 (2.3) and P3 and P6 (1.3). However, specimens with higher transverse reinforcement ratios and smaller vertical transverse reinforcement spacing exhibited slightly improved

20

deformation capacity. Figure 2.19(a) shows a comparison of unconfined specimens of various thicknesses; each specimen had the same length. Figure 2.19(b) shows a comparison of confined specimens of various thicknesses; each specimen had the same length. The detail configuration and spacing in these specimens were similar, and therefore the transverse reinforcement ratio along the minor axis (parallel to length) was highest in specimen P6 and lowest in specimen P4.

N°	Height [m]	Strain [%]	Conf.	s [mm]	Width [mm]	ρl [%]	ρtx [%]	ρty [%]
1	1	0	-	-	130	3,9	-	-
2	1	0	-	-	180	2,8	-	-
3	1	0	-	-	250	2,0	-	-
4	1	0	A	100	130	3,9	0,77	0,50
5	1	0	A	100	180	2,8	0,56	0,50
6	1	0	A	100	250	2,0	0,40	0,50
7	1	1	-	-	180	2,8	-	-
8	1	2	-	-	180	2,8	-	-
9	1,6	2	-	-	180	2,8	-	-
10	1	2	A	100	180	2,8	0,56	0,50
11	1,6	2	A	100	180	2,8	0,56	0,50
12	1,6	0	A	100	180	2,8	0,56	0,50
13	1	0	A	150	180	2,8	0,37	0,34
~~14~~	~~1~~	~~0~~	~~M~~	~~150~~	~~180~~	~~2,8~~	~~0,37~~	~~0,34~~
~~15~~	~~1~~	~~0~~	~~M~~	~~100~~	~~180~~	~~2,8~~	~~0,56~~	~~0,50~~
16	1	2	A	150	180	2,8	0,37	0,34
17	1	0	M	150	180	2,8	0,37	0,34
18	1	0	M	100	180	2,8	0,56	0,50
19*	1	0	A	100	180	2,8	0,56	0,50
20	1	0	A2	100	180	2,8	0,56	0,34
21	1	0	D1	100	180	3,8	0,56	0,50
22	1	0	D2	100	180	3,8	0,56	0,50
23	1	0	E1	100	180	3,8	0,56	0,67
24	1	0	E2	100	180	3,8	0,56	0,67

*10% eccentricity (e = 30 [mm])
ptx consistent with the short (width) direction
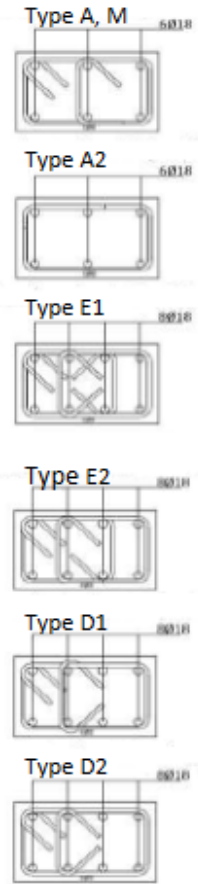
Figure 2.18 - Test matrix and confinement types for specimens tested by Massone *et al.* (2014)
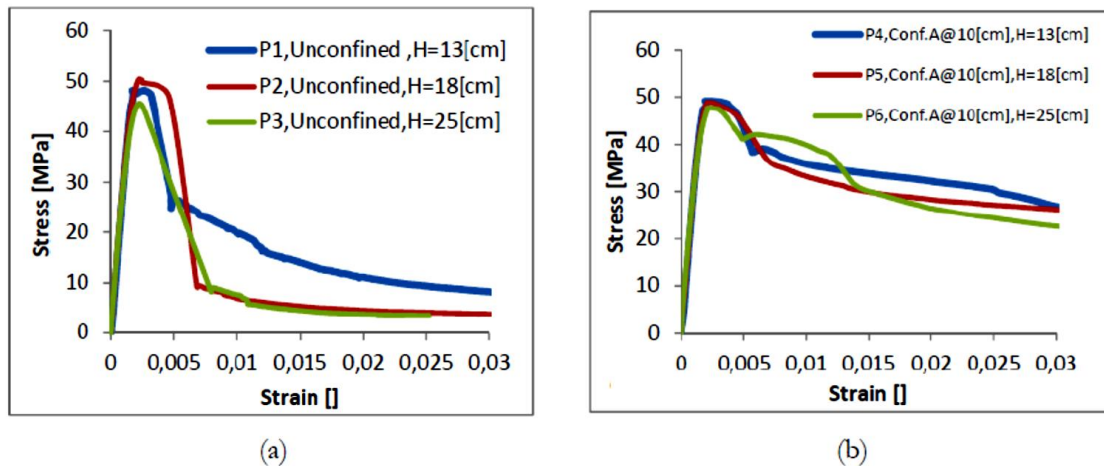
Figure 2.19 - Compressive Performance of Various Thicknesses for (a) Unconfined, and (b) Confined Specimens (Massone *et al.*, 2014)

As shown, specimens of varying thickness exhibited little difference in both strength and deformation capacity for both the unconfined and confined cases. The study did not investigate specimens with varying thickness but the same transverse reinforcement ratio; however, the strength was not substantially affected by the presence of confined steel as compared with the unconfined specimens. The study found a significant correlation between tensile pre-strain and the compressive performance of both unconfined and confined specimens. Figure 2.20 shows the compressive response of unconfined and confined specimens tested with and without a tensile pre-strain (of 2%). The comparison indicates that the confined specimen (P10) outperformed the unconfined specimen (P8) in both strength and deformation capacity following a tensile pre-strain of 2.0%.
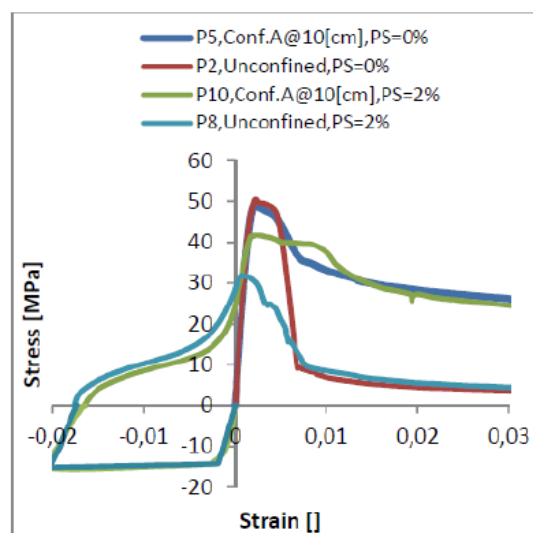
Figure 2.20 - Effect of Tensile Pre-Strain on Unconfined and Confined Specimens (Massone *et al.*, 2014)

2.4 Previous experimental studies on structural RC walls

There are numerous references on the analysis, design and behavior of isolated slender walls and a few of the experimental studies conducted on slender walls focusing on the influence of various design parameters on lateral load behavior are summarized below.

2.4.1. Portland Cement Association (PCA)

The most extensive study on reinforced concrete walls was conducted at the Construction Technology Laboratories in Skokie, Illinois in the 1970s. The study consisted of three phases, and in the first two phases (Oesterle *et al.*, 1976; Oesterle *et al.*, 1979) sixteen 1/3-scale structural walls were constructed. These walls had rectangular, barbell, and flanged cross sections, and were designed in accordance to the 1971 ACI Building code (Oesterle *et al.* 1979). Each of these rectangular walls was approximately 4.6m tall, 1.9m long and 10cm thick. The flanged walls had 90cm by 10cm flanges on each end, while the barbell walls had 30cm square boundary elements, see Figure 2.1. The concrete strength varied with each wall specimen from 21.8 to 53.6MPa, and the yield strength of the reinforcement varied from 410 to 510MPa. The axial load applied to the walls ranged from zero to approximately 9% of $A_g f'_c$. The walls were loaded in the plane of the web under increasing reversed cyclical displacements.

Oesterle *et al.* (1979) found that the different cross section shapes led to different patterns of wall behavior. The rectangular wall had limited out-of-plane stiffness due to the small width of the wall, making it more susceptible to instability in the compression zone under large load reversals resulting in out-of-plane buckling of the boundary element (Oesterle *et al.* 1979). This was observed in the failure of one rectangular test specimen subjected to in-plane lateral displacements. Oesterle *et al.* (1979) noted that rectangular walls exhibited lower flexural capacity compared to the barbell or flanged sections, of equal length and web thickness. Barbell shape prevented horizontal shear sliding failure by providing large dowel action in the boundary elements. The large boundary elements also provided high out-of-plane stiffness that minimized the wall instability. Large area of steel in the boundary element allows high flexural capacities to develop. Crushing of the web concrete was the primary failure mechanism observed in the tests because of the high strains that develop in the plastic region. Oesterle *et al.* recommended that barbell walls be designed for high shear stresses on the section. The flanged sections had a performance similar to the barbell shaped sections, with high flexural capacities developing and the requirement that high shear stresses must be designed for in the wall.
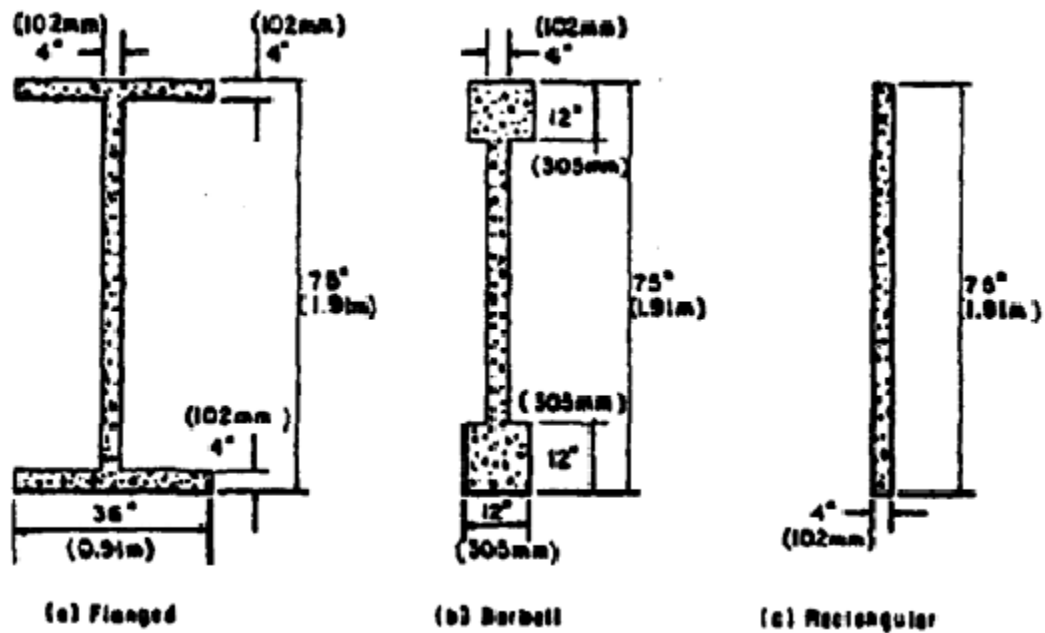
Figure 2.21 - Wall sections tested by Oesterle et al. (1979)

Two failure mechanisms were generally observed in the walls tested corresponding to the level of shear stress on the wall. In walls with low maximum shear stress (i.e., $V < 3f'_c$), the wall's displacement capacity was limited by buckling of the longitudinal reinforcement in the boundary elements and failure of the confined concrete. For walls with high maximum shear stress (i.e., $V > 7f'_c$) the displacement capacity was limited by crushing of the web concrete. The ductility of a wall, determined from measured rotations, decreased with increased shear stress ranging from approximately 8 to 3. Oesterle *et al.* also noted that for walls subjected to high shear stress where crushing of the web concrete limited the performance, uniform axial load of $0.1f'_c$ increased the ductility of the section.

2.4.2. Thomsen and Wallace (1995)

Thomsen and Wallace (1995) conducted an investigation on the behavior of structural walls with rectangular and T-shaped cross-sections. The walls were selected based on a prototype building multi-story office building located in a high seismic region for the floor plan of the prototype building. The building was six stories tall, and incorporated both rectangular and T-shaped walls as well as moment resisting concrete frames to resist lateral and gravity loads. All walls were approximately 3.6m tall and 1.2m long with a 10cm thick web. The T-shape walls included a 1.2m long and 10cm thick flange. Four 1/4-scale test specimens were constructed and identified as RW1, RW2, TW1, and TW2. The dimensions and reinforcement details of rectangular specimens RW1 and RW2 are shown in Figure 2.22Figure 2.23. RW2 differed from RW1 by using a closer spacing for the transverse reinforcing steel in the boundary elements to suppress buckling of the longitudinal reinforcement and allow the confined concrete to control the lateral load behavior of the wall. However, the diameter of the transverse reinforcement was not

changed, increasing the volumetric ratio by 50% thereby greatly increasing the confinement effects to the concrete.

Thomsen and Wallace used a displacement-based design procedure to determine estimates of the lateral roof displacement and story drifts of the prototype structure. In this procedure, individual walls were designed based on the required global deformations.
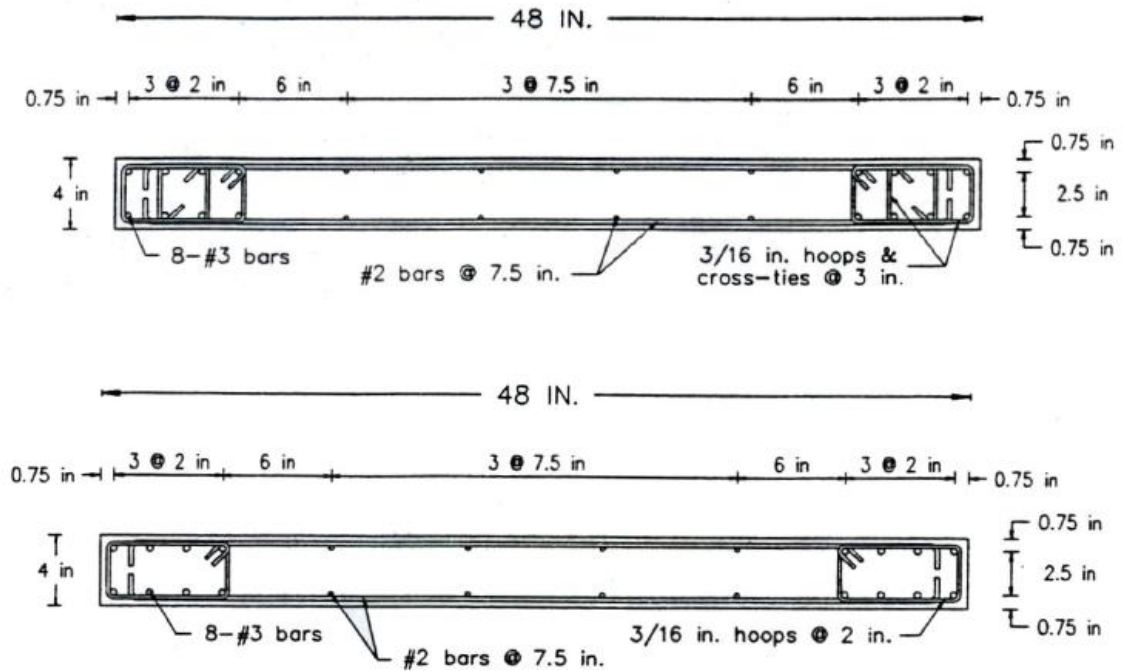
Figure 2.22 - Section of Rectangular Walls RW1 and RW2 Tested by Thomsen and Wallace (1995) (1in = 2.54cm)

Prior to applying lateral load, all walls were subjected to axial loads in the range of $0.07A_gf'_c$ to $0.1A_gf'_c$, where Ag is the gross cross-sectional area and f'_c is the measured concrete strength that were 31.6MPa and 43.6MPa for RW1 and RW2, respectively. The rectangular walls were loaded in the plane of the wall and cycled at least twice at each level of target story drift. The drift targets were 0.25%, 0.50%, 0.75%, 1.0%, 1.5%, 2.0%, and 2.5% drift. With good detailing, specimens RW1 and RW2 were expected to provide adequate ductility with no strength degradation. Figure 2.23 shows the response of rectangular walls, which experienced a symmetric response in terms of strength and ductility when loaded alternatively in the positive and negative directions. RW1 failed by buckling of all eight longitudinal bars in the boundary element between the transverse reinforcement at 1.5% drift. RW2 also failed due to buckling of the longitudinal reinforcement between the transverse reinforcement; however, the reduced spacing of the transverse reinforcement delayed buckling until 2.5% lateral drift.
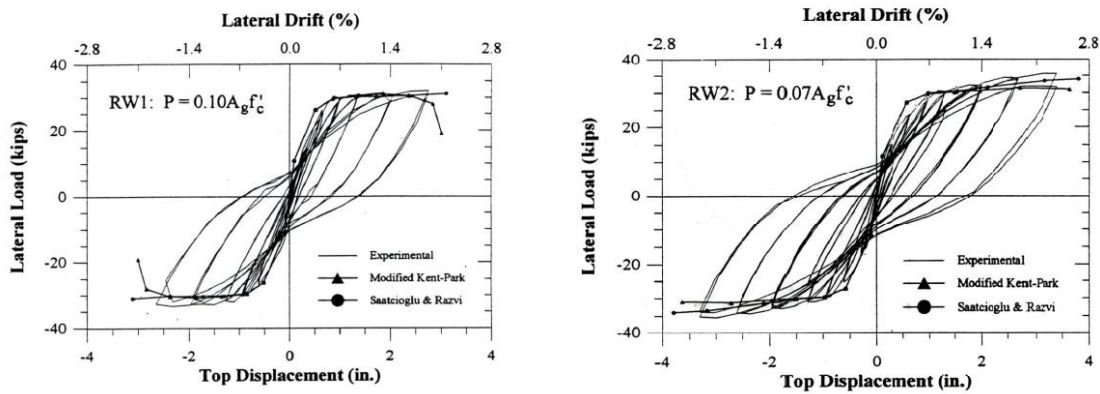
Figure 2.23 - Measured and Analytical Response of RW1 and RW2 (Thomsen & Wallace, 1995)

2.4.3. Dazio *et al.* (2009)

Dazio *et al.* (2009) tested six large-scale reinforced concrete cantilever walls under quasi-static cyclic loading to investigate the effects of different vertical reinforcement contents and different reinforcement ductility properties typical for the Central Europe on the deformation behavior of slender reinforced concrete walls. Various design variables such as, the longitudinal reinforcement layout and content, the ductility properties of the reinforcement, the confining reinforcement, and the applied axial load were varied among the specimens. The geometry and reinforcement details of the test specimens are shown in Figure 2.24.

The test specimens were half-scale models of the lower part of a reinforced concrete wall in a six-story reference building. The six specimens were labeled WSH1 to WSH6 respectively. They were 200cm long and 15cm. thick. The length of the shear span-to-wall length of the specimens was approximately 4.56m for WSH1 to WSH5 and 4.52m for WSH6, corresponding shear span ratios or the aspect ratios of 2.28 and 2.26, respectively.
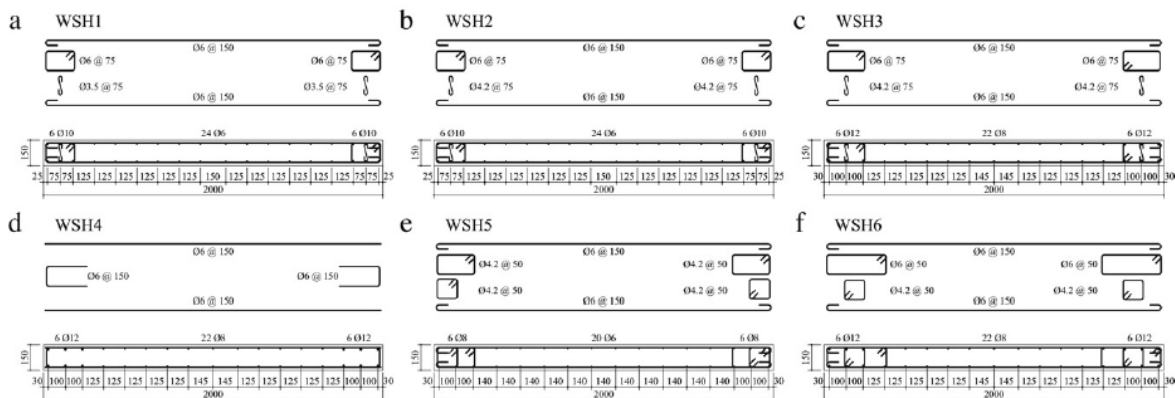
Figure 2.24 - Reinforcement layout in the plastic zone of the test units (All dimensions in mm) (Dazio *et al.* (2009))

All the specimens were subjected to reverse cyclic loading with load applied at the top of the wall. The loading history corresponded to the standard protocol recommended by Park (1998). The first step of the testing protocol was the application of the axial load, which was kept constant throughout each test. Subsequently, the horizontal cyclic displacement history was applied to the top of wall by an actuator with two load cycles at each ductility level. The first two cycles of the loading protocol were force controlled while the rest of the test was performed under displacement-control.

All the wall specimens performed satisfactorily under cyclic loads with stable response, good ductility and energy dissipation capabilities. The observed hysteresis responses of the test specimens are shown in Figure 2.25. The experiments showed that the crack patterns of the six test units were not equally developed at yield capacity of the walls. For walls for which the axial load contributed significantly to the moment resistance (e.g., WSH5) the crack pattern was less developed than for walls with large flexural reinforcement ratios (e.g., WSH3) and therefore the estimates of the yield displacement of the walls differed considerably. All six specimens failed in a flexural mode and for all the specimens the flexural deformations were considerably larger than the shear deformations. At larger drifts, in WSH1, WSH2, and WSH5 flexural deformations were concentrated towards the base of the wall, while in WSH3, WSH4, and WSH6 the flexural deformations are distributed over a larger portion of the wall.

The longitudinal web reinforcement in specimens WSH1, WSH2, and WSH5 fractured prematurely compared to the boundary element reinforcement. This was caused due to reduced spread of plasticity, smaller number of wider cracks in the web region due to the variation of the location and quantity of the vertical reinforcement, strain concentration at a crack due to the improved bond of the small diameter of the longitudinal web reinforcement when compared to the boundary region longitudinal reinforcement.

Based on the experimentally observed behavior of the six specimens, the authors concluded that walls with low longitudinal reinforcement ratios tend to have reduced flexure shear cracking. In addition, the smaller hardening ratio of the longitudinal reinforcement affected the spread of the plasticity causing the strain concentrations at the base of the wall and the reduced deformation capacity. It was also noted that the ductility properties of the longitudinal web reinforcement is as important as that of the boundary region reinforcement to achieve a good ductile response. In summary, the experiments showed the reduced deformation capacity of reinforced concrete structural walls with low longitudinal reinforcement content and this effect was further increased if reinforcing bars with low ductility properties were used.
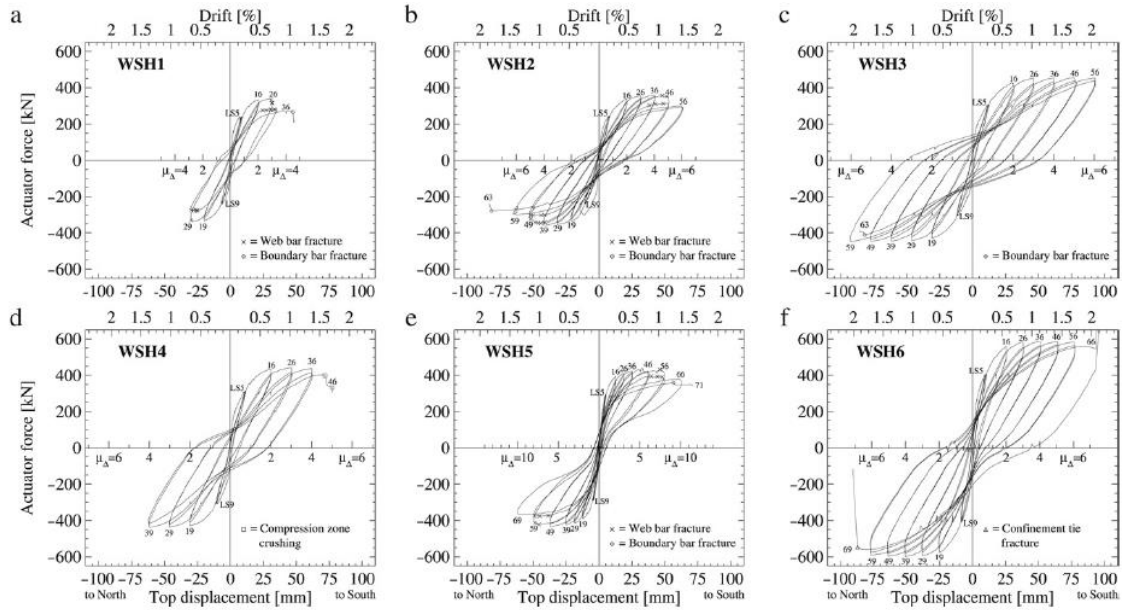
Figure 2.25 - Measured force-displacement hysteresis response of the six wall units tested by Dazio *et al.* (2009)

2.4.4. Tran and Wallace, (2015)

Five large-scale moderate aspect-ratio RC structural wall specimens, subjected to constant axial load combined with reversed cyclic lateral loading, were tested by Tran and Wallace (2015). Specimen identifiers and attributes are given in Table 2.1. Primary test variables included aspect ratio (1.5 and 2.0), which was also shear-span ratio in this case, axial load level ($0.025A_gf'_c$ and $0.10A_gf'_c$), and wall shear stress level. The walls were designed to yield in flexure prior to strength loss, with the level of shear stress at flexural yield as a primary variable

The five wall specimens were 15cm thick and 122cm long, with lateral load applied at either 183cm or 244cm above the wall-foundation interface. Axial load levels of $0.10A_gf'_c$ and $0.025A_gf'_c$ were applied to the first four specimens and the fifth specimen, respectively. The ratio of the area of vertical boundary reinforcement to the area of the boundary element varied between 3.23% and 7.11%. Transverse reinforcement at wall boundaries satisfies ACI 318-11 requirements for special structural walls.

Table 2.1 - Wall Specimen Attributes (Tran and Wallace, 2015)

Test No.	Specimen code	h_w/l_w	$\rho_t = \rho_l$ (%)	ρ_b (%)	$V@M_n^{des}/V_n^{des}$	P/A_gf_c	$V@M_n/V_n$	$\dfrac{V@M_n/A_{cv}}{\sqrt{f'_c}}$
1	RW-A20-P10-S38	2.0	0.27	3.23	0.80	0.073	0.81	3.6
2	RW-A20-P10-S63		0.61	7.11	0.88	0.073	0.91	6.1
3	RW-A15-P10-S51	1.5	0.32	3.23	0.80	0.077	0.83	4.9
4	RW-A15-P10-S78		0.73	6.06	0.84	0.064	0.85	7.0
5	RW-A15-P2.5-S64		0.61	6.06	0.79	0.016	0.79	5.8

Test results for moderate-aspect ratio cantilever walls indicate significant lateral strength loss at approximately 3.0% for all tests; however, significant lateral strength loss was observed for a variety of reasons, i.e., diagonal tension, web crushing, sliding shear, and buckling of vertical reinforcement. The results indicate that failure is impacted by aspect ratio, average shear stress level, axial load level, and vertical and horizontal reinforcement ratios. The contribution of nonlinear shear deformations to wall top lateral displacement varied between approximately 15% and 50%, with lower values for the aspect ratio 2.0 walls.

Wall specimen	"a"	"b"	"c"	"d"
RW-A20-P10-S38	4#4	4#4	6D6a @140 (@5.5in.)	D6b @140 (@5.5in.)
RW-A20-P10-S63	4#6	4#6	5#3 @152 (@6in.)	#3 @152 (@6in.)
RW-A15-P10-S51	4#4	4#4	7D6a @114 (@4.5in.)	D6b @114 (@4.5in.)
RW-A15-P10-S78	4#6	4#5	6#3 @127 (@5in.)	#3 @127 (@5in.)
RW-A15-P2.5-S64	4#6	4#5	5#3 @152 (@6in.)	#3 @152 (@6in.)
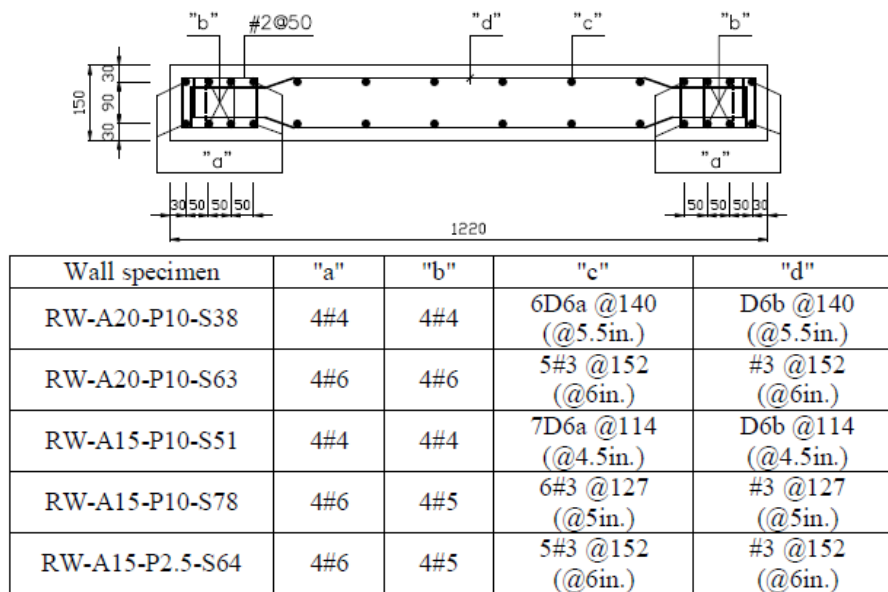
Figure 2.26 - Wall Reinforcement Details (Tran and Wallace, 2015)
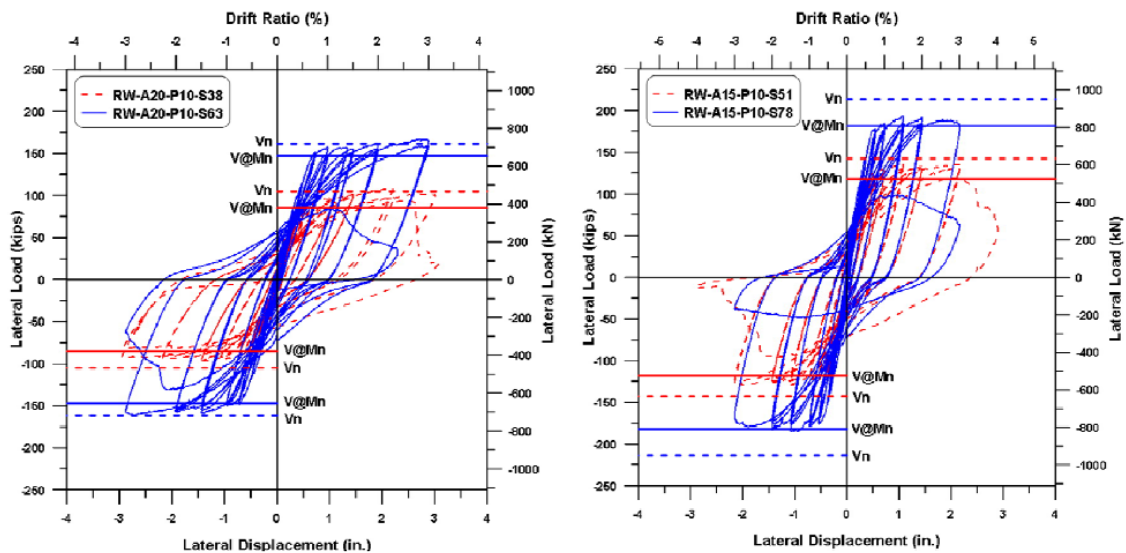
Figure 2.27 - Lateral load versus top displacement for wall specimens (Tran and Wallace, 2015)

2.5   Design of Reinforced Concrete Structural Wall

2.5.1.   Boundary Elements

Prior to the development of displacement-based design provisions by Wallace and Moehle (1992), which were incorporated into the 1994 UBC and subsequently incorporated, with modification, into ACI 318-99 (Wallace and Orakcal 2002), the requirement for including special boundary elements was determined by the expected compressive stress at the extreme fiber. According to these specifications, special boundary elements are required when the maximum extreme fiber compressive stress due to factored forces including earthquake effect is larger than $0.2f'_c$. The confinement must be extended over the height until the extreme fiber stress is less than $0.15f'_c$.

Wallace and Moehle (1992) found that these stress-based requirements were overly conservative and led to a need for special boundary elements in nearly all walls. They proposed an alternate, displacement-based approach to determine the need for special boundary elements and the associated dimensions where required. With this approach, the need for boundary elements is determined in accordance with the building configuration. Specifically, they found that the need for boundary elements is related to four issues:

1. The ratio of wall cross-sectional area to total floor-plan area, where boundary elements are generally not needed when this ratio exceeds approximately 1 percent;
2. The wall aspect ratio and configuration;
3. The wall axial load;
4. The wall reinforcement ratio (Thomsen and Wallace 1995).

 The implementation of Wallace and Moehle's recommendations requires confined boundary elements when:

$$c \geq \frac{l_w}{600(\delta_u / h_w)} \tag{2.1}$$

where c is the neutral axis depth, l_w is the wall length, δ_u is the roof displacement expected under the design earthquake, and h_w is the total wall height. Drift ratio δ_u/h_w may be taken as code compliance or, when a more precise estimate of the drift ratio is desired in early stages of design, rather than assuming the upper bound value, Thomsen and Wallace (1995) derived an estimate of the drift demand for a particular building and wall configuration as:

$$\frac{\delta_u}{h_w} = 0.00023 \frac{h_w}{l_w} \sqrt{\frac{1}{p}} \tag{2.2}$$

where p is the ratio of wall area to floor-plan area. Where confined boundary elements are required, confined boundary elements are extend vertically from the critical section a distance not less than the larger of l_w or $M_u/(4V_u)$, where M_u and V_u are the design moment and shear, respectively.

2.5.2. Distribution of Longitudinal Reinforcement

Concentrating longitudinal reinforcement in the boundary elements of a RC wall (i.e., a rectangular wall or a web or flange in a non-rectangular wall), rather than uniformly distributing it across section, leads to a small increase in the moment capacity of the section and a more substantial increase in the ductility of the section because it allows for a shallower neutral axis depth due to an increased area of steel in compression. However, this shallower neutral axis depth can lead to an increased susceptibility to sliding shear failures (Paulay and Priestley 1992). Additionally, tests have shown that using more closely spaced, smaller bars in the web of a wall improves its hysteretic response and energy dissipation capacity by minimizing the width of shear cracks (Paulay and Priestley 1992).

2.5.3. Bar Anchorage and Strain Penetration Effects

The development of stresses in reinforcing bars causes some relative movement between the bars and the foundation in which they are anchored. This slip occurs even when bars are sufficiently anchored, and it is distinct from much larger slip observed when bars are insufficiently anchored. Because of this slip, a rigid body rotation is observed in addition to the deformations from flexure and shear of the wall (Figure 2.28).

Historically, rotations due to strain penetration have generally not been separated from those due to flexural plastic hinging. While neglecting the effects of strain penetration in analysis often leads to satisfactory predictions of the overall force versus displacement response of a structure, it often overestimates the curvature demands on the plastic hinge region (Zhao and Sritharan 2007). Because correct prediction of local damage levels is critical to performance-based engineering, strain penetration effects cannot be ignored in the modeling of walls.
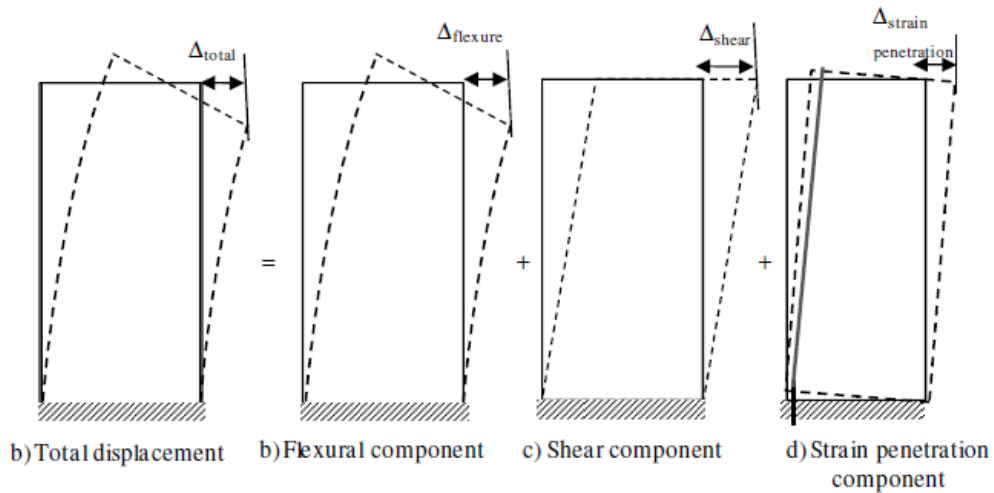
Figure 2.28 – Deformation components in RC walls under lateral force

2.6 Performance-Based Design: prediction of damage states

Performance-based engineering for seismic regions is being developed to provide engineers and owner-users with the tools required to make rational design decisions incorporating the costs of potential repairs and downtime into the costs of distinct design options that meet or exceed current life-safety provisions. In order to accomplish this objective, performance-based engineering requires the linking of defined performance levels, damage states, and likely repair requirements to engineering demand parameters (EDPs) that can be determined from structural analysis.

Previous works (FEMA 356, 2000, Berry *et al*., 2008, ASCE/SEI 41-13, 2014) considered the use of both macro level, deformation- or drift-based EDPs, such as drift or displacement ductility, and local EDPs, such as strain. While both approaches have been found to be reliable, the use of local EDPs is commonly understood to provide a better understanding of the expected damage level (Berry *et al*. 2008).

The selection of appropriate EDPs and damage measures for various performance levels is ongoing. FEMA 356 (200) represents an early effort in defining limits for the performance levels. ASCE/SEI 41-13 (2014) define limits for the performance levels as immediate occupancy (IO), life safety (LS), and collapse prevention (CP). The simplified modeling procedure recommend in ASCE/SEI 41-13 considers only flexural deformations and the axial load and shear demands on the member. Figure 2.29 and Table 2.2 summarize the modeling procedure and definition of performance levels in FEMA 356. In Figure 2.29, Q/Q_y is the ratio of the resistance of the member at a particular rotation (θ) or displacement (Δ) to the value at yielding. This resistance may be a shear force or a bending moment, depending on the particular analysis.

Table 2.2 - Modeling parameters and performance levels for walls with boundary elements controlled by flexure (ASCE/SEI 41-13, 2014)

Conditions		Plastic Hinge Rotation (rad)		Residual Strength Ratio	Acceptable Plastic Hinge Rotation (rad)		
$\dfrac{A_s f_y - A'_s f_y + P}{t_w l_w f'_c}$	$\dfrac{V}{t_w l_w \sqrt{f'_c}}$	a	b	c	Performance Level		
					IO	LS	CP
≤ 0.1	≤ 4	0.010	0.020	0.75	0.005	0.015	0.020
≤ 0.1	≥ 6	0.009	0.015	0.40	0.004	0.010	0.015
≥ 0.25	≤ 4	0.005	0.012	0.60	0.003	0.009	0.012
≥ 0.25	≥ 6	0.008	0.010	0.30	0.0015	0.005	0.010

A_s is the area of longitudinal reinforcement in tension, A'_s is the area of longitudinal reinforcement in compression, t_w is the thickness of the web, l_w is the length of the web, f_y is the yield strength of the reinforcement, f'_c is the compressive strength of the concrete, P is the applied axial compression load, a and b are plastic hinge rotations indicated, and c is the residual fraction of the strength after the collapse prevention limit is reached.
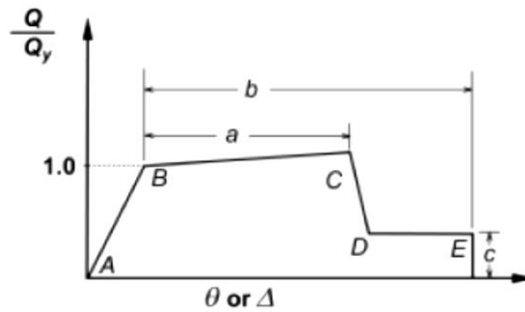
Figure 2.29 - Generalized force-deformation relations for concrete elements (ASCE/SEI 41-13, 2014)

Recent efforts have refined the definitions of performance levels and have correlated more specific damage measures with the general performance levels, and many of these efforts have expanded the number of performance and damage levels defined. For instance, Pagni and Lowes (2006) recommend 12 discrete damage levels for reinforced concrete beam-column joints. These damage levels range from initial hairline cracking requiring the replacement of finishes to crushing of the concrete core and reinforcement failure due to buckling, pullout, or fracture requiring replacement of the entire section. Berry *et al*. (2008) determined that these damage levels are appropriate for describing damaged condition of reinforced concrete structural elements in general and selected four of these damage levels as the most important for predicting repair costs and downtime for performance-based engineering of reinforced concrete columns. Some of these limits may be found to apply to all reinforced concrete structural elements, while other limits may depend on the type of element under consideration (e.g., walls, columns, and beam-column joints).

2.7 Analysis and Modeling of Reinforced Concrete Structural Wall

Structural walls have been modeled and analyzed using different approaches by researchers. A summary of various modeling approaches used for wall studies are presented with commentary on the advantages and disadvantages of the different approaches.

2.7.1. Finite Element Method

2.7.1.1. 3D elements modeling

The behavior of structural walls has been simulated using solid or brick elements. Solid elements have been used by a number of researchers (e.g. Deshmukh *et al.* 2006; Moaveni *et al.* 2006) to simulate the structural wall behavior under lateral loads. This modeling approach has the advantage of allowing strain and corresponding stress to vary across the section without the user having to specify a particular distribution such as that based on the plane section remains plane assumption. Additionally the shear stiffness of the wall is determined for the individual elements. In this approach, the longitudinal and transverse reinforcement can be smeared across the solid element or modeled discretely using truss elements. The 3D nature of the model allows bi-directional lateral loads to be applied to the wall. However, solid elements have some significant disadvantages. These include incorporating an accurate 3D concrete material model that can accurately model the initiation, propagation, and orientation of cracks as they form in concrete elements as well as the loading and unloading paths. A large number of solid elements may be required to model the concrete and reinforcement of a wall accurately, which may require significant computational time to run the analysis. Including the effects of strain penetration is challenging and typically ignored in the analysis.

2.7.1.2. 2D elements modeling

2D elements (plain stress, shell, …) have also been used to simulate the response of structural walls in 2D. A reliable 2D concrete model is required for the analysis that should include the effects of cracking and appropriate unloading/reloading rules. In addition to the concrete model, complexity and number of elements, these models are being limited to unidirectional loading only. Similar to solid elements, including the effects of strain penetration is difficult and commonly ignored (e.g., Sittipunt and Wood, 1993). Some researchers have addressed this later shortcoming by modeling the strain penetration effects using pairs of nonlinear gap-truss elements to model the reinforcement at the base of each wall (Kelly, 2006).

2.7.2. Macro Models

Macro Models use a type of element with global response parameters specified directly. Typically, macro models lump various behaviors into one element to simplify the analysis

and increase the computational efficiency of the analysis. Macro model elements are used to capture regions of nonlinear behavior, while linear elements are used in elastic regions. One example of a macro model element is the multiple-vertical-line-element-models (MVLEM) that have been shown to capture the response of structural walls (Fischinger and Isakovic, 2006; Orakcal *et al.*, 2004). This modeling approach simulates the behavior of rectangular walls using a series of vertical and shear springs connected by rigid beams at the top and bottom of the element. The force-displacement characteristics of the springs can be defined to incorporate the various response components of the structural walls.

The primary advantage of macro model elements is that they are very computationally efficient and provide good simulation of the global wall behavior. However, macro model elements require experience and knowledge to determine the force-displacement relationships for the springs, rather than stress-strain relationships of the material that are more familiar to most engineers. Additionally, strain penetration and other behaviors are lumped together in the spring behavior, potentially leading to inaccurate simulation at the local level.

2.7.3. Fiber-Based Models

Fiber-based models have been used to simulate response of structural walls (e.g., Martinelli and Filippou, 2006; Grange *et al.*, 2006; Dazio, 2006). The fiber-based approach represents the section with a group of uniaxial fibers with only uniaxial material properties defined, and it is significantly less computationally expensive than traditional finite element analysis using three-dimensional elements with nonlinear material properties; although, the primary intended application of these models is still for research, rather than design.

These models allow the user to specify uniaxial stress-strain behavior of longitudinal reinforcement as well as that of confined and unconfined concrete including the effects in the transverse direction. A large variety of models are available that can be used to characterize the behavior of different materials in order to capture the section and member responses accurately. Since the model is based on the uniaxial stress-strain behavior of groups of fibers, the models are easier to build and understand.

The fiber-based concept has previously been applied to beam-column elements with success, but three limitations have prevented its application to wall sections:

- The assumption in the fiber-based model formulation is that plane sections remain plane. This might be not always true in wall critical sections, and consequently, strains and curvatures may not be calculated correctly.
- Fiber-based analyses typically assume perfect bond between the concrete and the reinforcement, neglecting the contributions of strain penetration to the total deformation of the wall.

- Fiber-based models neglect shear deformations. previous testing, such as that by Thomsen and Wallace (1995) indicated that even for slender structural walls with aspect ratios greater than 2.5, shear deformations can contribute more than 10% of the total deformation of the wall. For intermediate aspect ratio walls with shear span-to-wall length ratio ranging approximately between about 1.5 and 2.5 and designed for flexural failure, nonlinear shear behavior may be not negligible, and may lead to lower strength and stiffness with larger concrete compressive strains demand at the wall end regions (Massone *et al.* 2006, Orakcal and Wallace 2006). Several analytical models have been proposed to incorporate shear flexure interaction based on fiber-type models (Massone *et al.* 2009, Jiang and Kurama 2010), empirical models (Elwood 2002), or semi-empirical models (Beyer *et al.* 2011), but relatively little model validation for structural walls has been reported.

2.8 Conclusions

Due to a number of factors, including advances in structural modeling capabilities and modern architecture demand in using slender walls, modern walls are likely to be constructed with thinner compression regions and designed for larger lateral drift and axial load demands. Based on a substantial amount of research on the seismic performance of reinforced concrete structural walls, modern design provisions for mid-rise and high-rise shear wall buildings have been developed with the goal of achieving significant ductility in the event of strong earthquake ground shaking. Observations following recent earthquakes in Chile (2010) and New Zealand (2011) have demonstrated the potential for shear wall buildings designed according to modern seismic design codes to experience brittle failures.

Research on construction practice trends in Chile identified an important trend for mid-rise and high-rise RC wall buildings: while average building heights have increased over the past few decades, the ratio of wall area to floor plan area has remained relatively constant, cross-sections have become thinner, and axial stress ratios have increased. Based on the extent of damage observed in Chile and New Zealand, it is likely that performance for slender walls have been reached by current design and construction practice. It is important to understand the behavior limitations of walls designed for large ductility demands.

Research has demonstrated that slender walls can achieve large lateral drift ratios when compression zones in yielding regions are adequately detailed to remain stable. Many of the presented experimental programs on confined boundary element evaluated the effects of tensile pre-strain on compressive performance. The general trends indicate that significant tensile strain prior to compression damage results in a significant reduction in strength and deformation capacity. However, these tests were all loaded monotonically in compression to failure following the peak tensile strain, which may not be indicative of

actual loading conditions. Therefore, a review into the effects of cyclic loading are included in the experimental program on confined boundary element in Chapter 3. In addition, most tests focused on global buckling of wall boundary rather that buckling of longitudinal reinforcement.

References

1. Acevedo, C., (2010), "Seismic Vulnerability of Non-Special Boundary Elements of Shear Wall under Axial Force Reversals," Florida International University.

2. ACI, (2008), "Building code requirements for structural concrete (ACI 318-08) and commentary (ACI318R-11)", American Concrete Institute, MI, USA.

3. ACI, (2011), "Building code requirements for structural concrete (ACI 318-11) and commentary (ACI318R-11)", American Concrete Institute, MI, USA.

4. ACI, (2014), "Building code requirements for structural concrete (ACI 318-14) and commentary (ACI318R-14)", American Concrete Institute, MI, USA.

5. Berry, M., Lehman, D., Lowes, L., (2008), "Lumped-plasticity models for performance simulation of bridge columns", ACI Structural Journal, 105(3): 270-279.

6. Beyer, K., Dazio, A., Priestley, M. J. N., (2011), "Shear Deformations of Slender Reinforced Concrete Walls under Seismic Loading", ACI Structural Journal, 108(2): 167-177.

7. Chai, Y. H., Elayer, D. T., (1999), "Lateral stability of reinforced concrete columns under axial reversed cyclic tension and compression", ACI Structural Journal, 96(5): 780–790.

8. Chrysanidis, T. A., Tegos, I. A., (2012), "The Influence of Tension Strain of Wall Ends to their Resistance against Lateral Instability for Low-Reinforced Concrete Walls", 15th World Conference on Earthquake Engineering, Lisbon. Portugal.

9. Creagh, A., Acevedo, C., Moehle, J., Hassan, W., Tanyeri, A. C., (2010), "Seismic Performance of Concrete Special Boundary Element" The University of Texas at Austin.

10. Dazio, A., (2006)., "Some Aspects of RC Walls Modeling using Fiber Elements", Proceedings of the NEES/UCSD Workshop on Analytical Modeling of Reinforced Concrete Walls, San Diego.

11. Dazio, A., Beyer, K., Bachmann, H., (2009), "Quasi-static cyclic tests and plastic hinge analysis of RC structural walls", Engineering Structures, 31(7): 1556-1571.

12. Deshmukh, K., Thiagarajan, G., Heausler, T., (2006), "Numerical Modeling of Seven Story Reinforced Model Using SAP", NEES/UCSD Workshop on Analytical Modeling of Reinforced Concrete Walls, San Diego.

13. Earthquake Engineering Research Institute (EERI), (2010), "The Mw 8.8 Chile Earthquake of February 27, 2010", EERI Earthquake Spectra Special Earthquake Report.

14. Elwood, K.J., (2002), Shake Table Tests and Analytical Studies on the Gravity Load Collapse of Reinforced Concrete Frames, PhD Dissertation, Department of Civil and Environmental Engineering, University of California, Berkeley.

15. Federal Emergency Management Agency, (2000), "Prestandard and Commentary for the Seismic Rehabilitation of Buildings (FEMA-356)" ASCE, 518 pp.

16. Fishinger, M., Isakovic, T., (2006), "NEES Blind Prediction Testing on RC Wall

Building Slice, Multiple-Vertical-Line-Element Model", Proceedings of the NEES/UCSD Workshop on Analytical Modeling of Reinforced Concrete Walls, San Diego.

17. Grange, S., Mazars, J., and Koronis, P., (2006), "Seven-Story Building Slice Earthquake Blind Prediction Contest: A Simplified Model Using Multi Fiber Timoshenko Beams", Proceedings of the NEES/UCSD Workshop on Analytical Modeling of Reinforced Concrete Walls, San Diego.

18. Jiang, H., Kurama, Y., (2010), "Analytical modeling of medium-rise reinforced concrete shear walls", ACI Structural Journal, 107(4.): 400-410.

19. Kelly, T., (2006). "A Blind Prediction Test of Nonlinear Analysis Procedures for Reinforced Concrete Shear Walls", Bulletin of New Zealand Society for Earthquake Engineering, 40(4): 142-158.

20. Martinelli, P., Filippou, F., (2006), "Numerical Simulation of the Shake Table Test of a Full Scale, Seven Story Shear Wall Specimen", Proceedings of NEES/UCSD Workshop on Analytical Modeling of Reinforced Concrete Walls, San Diego.

21. Massone, L. M., Orakcal, K., Wallace, J. W., (2006), "Modeling flexural/shear interaction in rc walls", American Concrete Institute, ACI-SP-236: 127–150.

22. Massone, L. M., Polanco, P., Herrera, P., (2014), "Experimental and Analytical Response of RC Wall Boundary Elements", Proceedings of the 10th U.S. National Conference on Earthquake Engineering, Anchorage.

23. Massone, L. M. , Bonelli, P., Lagos, R., Lüders, C., Moehle, J., Wallace, J. W., (2012), "Seismic Design and Construction Practices for RC Structural Wall Buildings", Earthquake Spectra, 28(S1): S245-S256.

24. Moaveni, B., He, X., Conte, J., Restrepo, J., (2006), "System Identification of a Seven-Story Reinforced Concrete Shear Wall Building Slice Tested on the UCSD-NEES Shake Table", NEES/UCSD Workshop on Analytical Modeling of Reinforced Concrete Walls, San Diego, CA December 2006.

25. Network for Earthquake Engineering Simulation, "NEEShub - The Chile Earthquake Database Group", https://nees.org/groups/chileearthquakedatabase. (Accessed Jun. 2017)

26. Oesterle, R. G., Aristizabal-Ochoa, J. D., Fiorato, A. E., Russell, H. G. and Corley, W. G., (1979), "Earthquake Resistant Structural Walls – Tests of Isolated Walls – Phase II," Portland Cement Association, Skokie, Illinois.

27. Oesterle, R.G., Fiorato, A. E., Johal, L. S., Carpenter, J. E., Russell, H. G. and Corley, W. G., (1976), "Earthquake Resistant Structural Walls – Tests of Isolated Walls," Portland Cement Association, Skokie, Illinois.

28. Orakcal, K., Wallace, J. W., (2006), "Flexural Modeling of Reinforced Concrete Walls: Experimental Verification", ACI Structural Journal, 103(2): 196-205.

29. Orakcal, K., Wallace, J.W., Conte, J.P., (2004), "Nonlinear Modeling and Analysis of Slender Reinforced Concrete Walls", ACI Structural Journal, 101(5): 688 - 699.

30. Pagni, C.A., Lowes, L.N., (2006), "Fragility functions for older reinforced concrete beam column joints". Earthquake Spectra, 22(1): 215-238.

31. Paulay, T., Priestley, M. J. N., (1992), "Seismic Design of Reinforced Concrete and Masonry Buildings", John Wiley and Sons, New York, 744 p.

32. Pilakoutas, K., Elnashai, A., (1995), "Cyclic behavior of reinforced concrete cantilever walls. I: Experimental results", ACI Structural Journal 92 (3): 271-281

33. Sittipunt, C., Wood, S. L., (1993), "Finite Element Analysis of Reinforced Concrete Shear Walls", Report to the National Science Foundation, Department of Civil Engineering, University of Illinois at Urbana-Champaign.

34. Sritharan, S., Beyer, K., Henry, R.S., Chai, Y. H., Kowalsky, M., Bull, D., (2014), "Understanding Poor Seismic Performance of Concrete Walls and Design Implications", Earthquake Spectra, 30(1): 307-334.

35. Standards Council, Concrete Structures Standard, Wellington: Standards New Zealand, NZS 3101-1, 2006.

36. Thomsen, J. H., Wallace, J. W., (1995), "Displacement-based design of reinforced concrete structural walls: Experimental studies of walls with rectangular and T-shaped cross sections", Report No. CU/CEE-95/06, Department of Civil and Environmental Engineering, Clarkson University, Potsdam.

37. Tran T. A. and Wallace J. W., (2015), "Cyclic Testing of Moderate-Aspect-Ratio Reinforced Concrete Structural Walls", ACI Structural Journal, 112(6): 653-666.

38. Wallace J. W., (2011), "February 27, 2010 Chile Earthquake: Preliminary Observations on Structural Performance and Implications for U.S. Building Codes and Standards," in Structures Congress 2011, Las Vegas.

39. Wallace J. W., Massone L. M., Bonelli P., Dragovich J., Lagos R., Lüders C. and Moehle J., (2012), "Damage and implications for seismic design of RC structural wall buildings", Earthquake Spectra, 28(S1), pp. S281–S299.

40. Wallace, J. W. and Moehle, J. P., (1992), "Ductility and detailing requirements of bearing wall buildings", ASCE Journal of Structural Engineering, 116(6): 1625–1644.

41. Wallace, J. W., Orakcal, K., (2002), "ACI 318-99 provisions for seismic design of structural walls", ACI Structural Journal 99 (4): 499-508.

42. Zhao, J., Sritharan, S., (2007), "Modeling of Strain Penetration Effects in Fiber-Based Analysis of Reinforced Concrete Structures," ACI Structural Journal, 104(2): 133-141.

43. Zhang, Y., Wang, Z., (2000), "Seismic Behavior of Reinforced Concrete Shear Walls Subjected to High Axial Loading", ACI Structural Journal. 97(5): 739-750.

CHAPTER 3 EXPERIMENTAL STUDY ISOLATED CONFINED BOUNDARY ELEMENTS

3.1. Introduction

A RC structural wall, as a building component, consists of two unique sub-components: the confined boundary elements and the web. Boundary elements are located on either end of the wall, and provide the majority of the flexural capacity. The web of a structural wall between the boundary elements, and provides the majority of the shear capacity. An experimental program was conducted in order to bring insight on the seismic performance of confined boundary elements of RC rectangular walls. The objective was to investigate the influence of longitudinal and transverse reinforcement detailing, cross-section slenderness and loading type (Monotonic and cyclic) on their compressive capacity, damage process and failure modes. It is also important to contribute to make an experimental database related to failures by buckling of reinforcement and global buckling.

3.2. Experimental Concept

The behavior of boundary regions in a ductile RC wall subjected to lateral loading was studied by isolating the boundary regions of the wall as axially loaded RC column. Although this approach lacks strain gradient effects expected across the wall section and ignore the contribution of the shear component, the idealization is useful to provide an understanding of the behavior and to identify critical parameters involved during lateral loading of RC walls, where confined boundaries are subjected to large amplitude of tension and compression cycles. This scheme provides excellent time and cost benefits as compared to testing large-scale wall specimens. Figure 3.1 is a schematic showing the demands on a structural wall, and how the test specimens were representative of a boundary element.
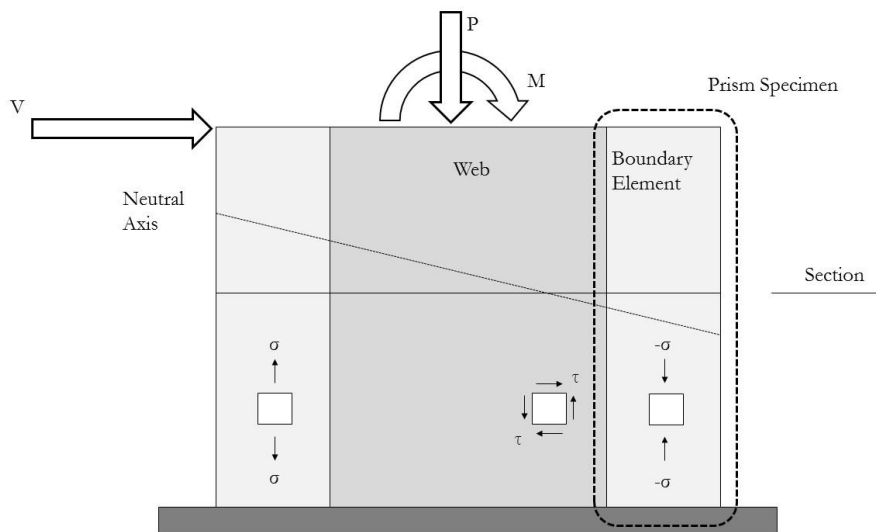
Figure 3.1 - Experimental Concept

The test specimens also varied slightly from a boundary element in that a boundary element is laterally restrained by the web portion of the wall on one side. This lateral restraint exists in both the in- and out-of-plane directions, and has a more significant effect in the out-of-plane direction due to the lower stiffness in that direction. However, that restraint is limited in slender planar walls due to the lower flexural stiffness. Figure 3.2 shows the conceptual progression from the compression boundary element within the prototypical structural wall shown in Figure 3.1 to the test specimens, as implemented within this experimental program.
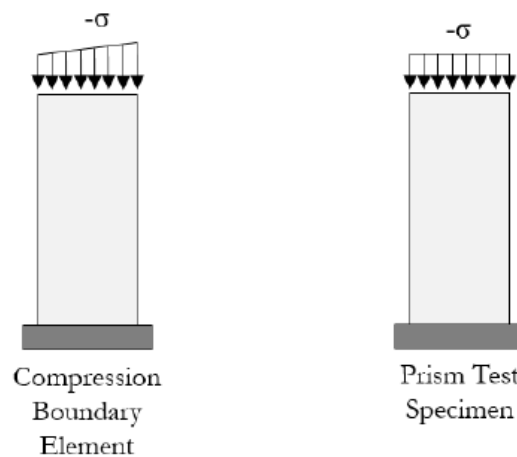
Figure 3.2 - Conceptual Progression between Compression Boundary Element and Test Specimen

3.3. Description of the Test Elements

A total of sixteen (16) rectangular elements with two different sectional dimensions (B-type and C-type) having approximately similar cross-sectional area were constructed and tested. Table 3.1 shows the cross-sectional configurations, the layouts and amounts of reinforcement. The elements were built without cover concrete so that to avoid a sudden drop in the response curves following spalling of cover concrete, since the objective was to assess ultimate behavior and final failure modes. The cross section dimensions ($b \times l$) for B-type and for C-type specimens represent two levels of slenderness (h/b). The dimensions are measured from the outside of the transverse reinforcement. The shorter side length of the section corresponds to boundary wall thickness. For B-type specimens, specimens from 1B to 4B were constructed with four levels of transverse reinforcement ratio ranging from 0.22% to 1.27%, respectively. Specimens 5B and 6B were constructed with similar transverse reinforcement ratios as for 1B and 4B specimens, respectively, but with larger longitudinal reinforcement ratio. For C-type specimens (1C and 3C), two levels of transverse reinforcement were set and were also similar to transverse reinforcement ratios of 1B and 4B, respectively. For each of these eight configurations, two identical specimens were built to produce sixteen specimens so that each configuration was tested under monotonic compressive load and under cyclic tension and compression reversal load. The last characters in the specimens label stand for loading type, M for monotonic and C for cyclic. D4 (SD295A) deformed reinforcing bars were used for transverse reinforcement for lightly confined specimens and D6 (SD295A) for densely confined specimens. All transverse reinforcement had 135-degree hooks. D10 (SD295A) deformed reinforcing bars were used for longitudinal reinforcement for B1-type ($\rho_l = 2.63\%$) and C-type ($\rho_l = 3.24\%$) specimens, while D16 (SD295A) deformed reinforcing bars were used for B2-type ($\rho_l = 7.33\%$).

Figure 3.3 shows vertical reinforcement layout of 6B and 1C configurations. Longitudinal reinforcing bars were bent 180-degrees at their ends and hanged to a D25 (SD345) deformed reinforcing bars in the upper and lower stub to ensure good anchorage. D25 bars were also used as longitudinal reinforcement for lower and upper stubs with D10 transverse reinforcement. The tested elements had 600mm height (h) with fixed at both ends to the lower and upper stubs. This height represents the lower portion of the confined boundary in a wall where likely compressive failure may occur. Observations from previous experimental studies indicate that the compressive failure region is limited within a height of about 2.5 times the wall thickness (Markeset and Hillerborg 1995, Takahashi *et al.* 2013).

Table 3.1 – Element specimens cross-sections and reinforcement details

Specimen		Section $b{\times}l$ (mm)	Layout (Unit: mm)	Long. Reinf	Transv. Reinf.	s/d_b	Loading type
B1-type	1B-M	238×108		10-D10 ($\rho_l = 2.63\%$)	3-D4@80 ($\rho_t = 0.22\%$)	8	Monotonic
	1B-C						Cyclic
	2B-M				6-D4@80 ($\rho_t = 0.42\%$)	8	Monotonic
	2B-C						Cyclic
	3B-M	242×112			6-D6@80 ($\rho_t = 0.95\%$)	8	Monotonic
	3B-C						Cyclic
	4B-M				6-D6@60 ($\rho_t = 1.27\%$)	6	Monotonic
	4B-C						Cyclic
B2-type	5B-M	238×108		10-D16 ($\rho_l = 7.33\%$)	3-D4@80 ($\rho_t = 0.22\%$)	5	Monotonic
	5B-C						Cyclic
	6B-M	242×112			6-D6@60 ($\rho_t = 1.27\%$)	3.75	Monotonic
	6B-C						Cyclic
C-type	1C-M	363×68		12-D10 ($\rho_l = 3.24\%$)	4-D4@70 ($\rho_t = 0.22\%$)	7	Monotonic
	1C-C						Cyclic
	3C-M	367×72			6-D6@40 ($\rho_t = 1.29\%$)	4	Monotonic
	3C-C						Cyclic

Note: ρ_l: is the longitudinal reinforcement ratio $\rho_l = A_l /(b{\times}l)$, ρ_t is the transverse reinforcement ratio $\rho_t = A_t /(l{\times}s)$, A_l and A_t are the longitudinal and transverse reinforcement area, respectively.
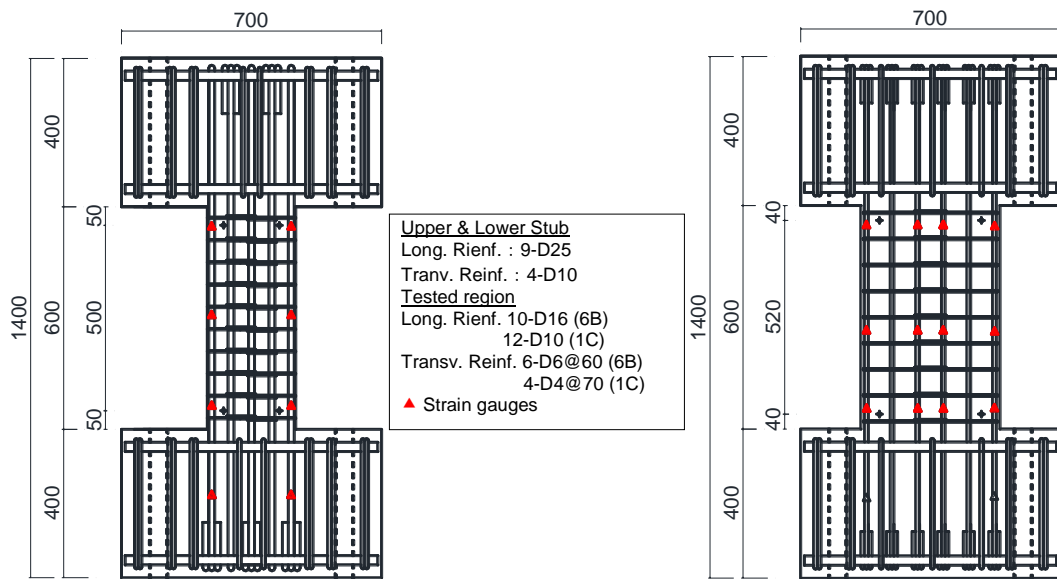
Figure 3.3 - Vertical reinforcement layout of 6B-M/6B-C (left) and 1C-M/1C-C (right)

3.4. Material Properties

Table 3.2 and Table 3.3 show measured material properties for concrete and reinforcing bars, respectively. A concrete mix with 13mm of maximum aggregate size and 12cm for slump test was used.

Table 3.2 – Concrete mechanical properties

Compressive strength (MPa)	Strain at peak (%)	Young's modulus (GPa)	Splitting tensile strength (MPa)
24.5	0.18	26.3	2.3

Table 3.3 – Reinforcing bars mechanical properties

Reinforcing Bar	Young's modulus (GPa)	Yield strength (MPa)	Ultimate strength (MPa)
D4	/	363	532
D6	192	365	516
D10	190	347	484
D16	188	325	462
D25	192	381	567

3.5. Specimen Construction

Specimen were cast vertically, representative of common construction practice for walls and columns. Longitudinal reinforcement was anchored in the upper and lower stubs with sufficient anchorage length. Steel cages of the lower stub were first constructed and mounted into the wooden forms; test elements were then prepared and inserted into the lower stub. The elements were cast vertically in two stages, the lower stub was cast first (Figure 3.4(a)) and then the element with the upper stub as one part (Figure 3.4(b)) with intentionally roughened surface created at lower stub–element interface to insure adherence.

| (a) | (b) |

Figure 3.4 –Specimens construction

3.6. Loading Method and Measurement

Figure 3.5 shows test setup and loading protocol. A Universal Testing Machine with a capacity of 1500kN was used to apply vertical load on the upper stub under the condition of uniaxial tension and compression. Only vertical displacement is possible and the head of the testing machine have no freedom for rotation or lateral displacement. For monotonic tests, the compression load was applied gradually until failure. For cyclic tests axial loading history was determined based on the average strain at the lower part of previously tested RC structural walls and previous tests on isolated RC boundary elements (Chai and Elayer, 1999). A ratio of tensile-to-compressive strain of 5 was used as the loading protocol. Thus, the loading cycle consisted of an initial half cycle of axial tensile strain followed by a compression half cycle with a nominal target compressive strain 1/5 of the axial tensile strain. The test was terminated when the resistance of the specimen decreased significantly and the specimen exhibited instability. Thus, two cycles of loading were applied that correspond to yielding tensile strain followed by tensile strains of 0.5%, 1%, 1.5% 2%, 3% and 4% (Figure 3.6). A load cycle is considered stable if the target compressive strain was reached in two successive cycles without excessive decrease in compressive capacity. The specimens were tested at low rate of monotonic

loading which was in the order of 1mm/min for compression and 4mm/min for tension to insure that no strain rate effects were introduced to damage process.
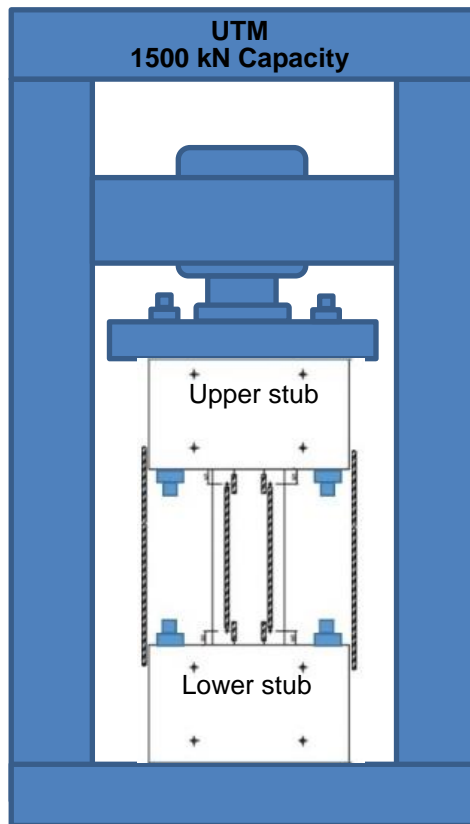
Figure 3.5 –Loading machine and test setup
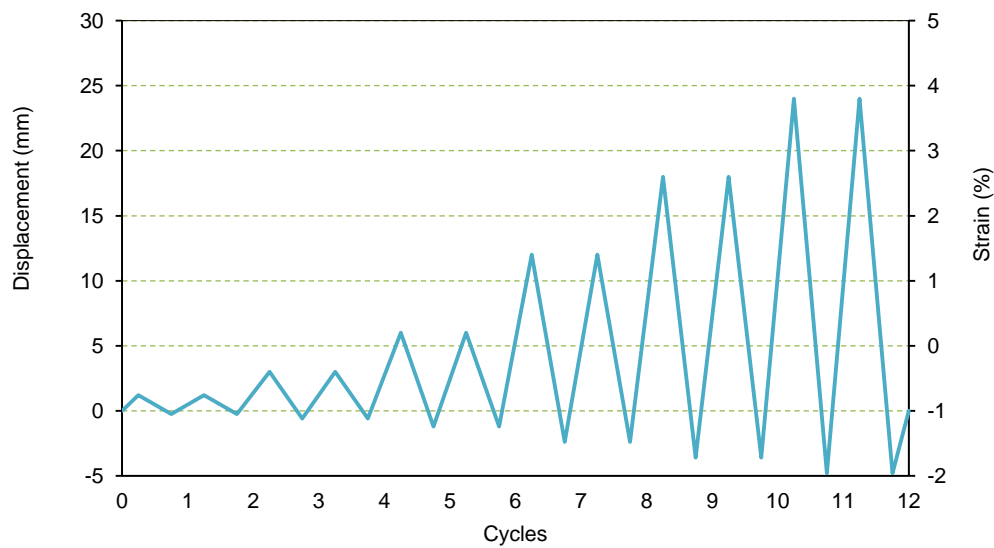
Figure 3.6 – Cyclic loading protocol

Figure 3.7 shows displacement transducers positions for B-type and C-type configurations. Displacement transducers were mounted to both ends of the longer side length of the prism section which was divided into three measuring zones Z1 (Gauges ① and ②), Z2 (Gauges ③ and ④) and Z3 (Gauges ⑤ and ⑥). These zones were set at intervals of 0~50mm for Z1 at the bottom part of the element, 50~550mm for Z2 at the middle, and 550~600mm for Z3 at the top part for B-type elements, and at intervals of 0~40mm (Z1), 40~560mm (Z2) and 560~600mm (Z3) for C-type elements. This difference in insert positions between B-type and C-type was due to transverse reinforcement position. Two displacement transducers (Gauges ⑦ and ⑧) were also installed between upper and lower stub at both sides to check any possible inclination during test. Although variation of configurations and confinement may affects the degree of localization and measured strain, measured strains are compared in an average manner. The nominal axial strain, ε_{nom}, was defined experimentally as the strain corresponding to average displacement at both ends of the specimen over its total height h (600mm).

$$\varepsilon_{nom} = \frac{1}{2}\left[\frac{(N_1 + N_3 + N_5)}{h} + \frac{(S_2 + S_4 + S_6)}{h} \right]$$

(3.1)

where, N_1, N_2 and N_3 are displacements corresponding to north side transducers 1, 3 and 5, respectively. S_1, S_2 and S_3 are displacements corresponding to south side transducers 2, 4 and 6, respectively, and h is the specimen height (600mm).
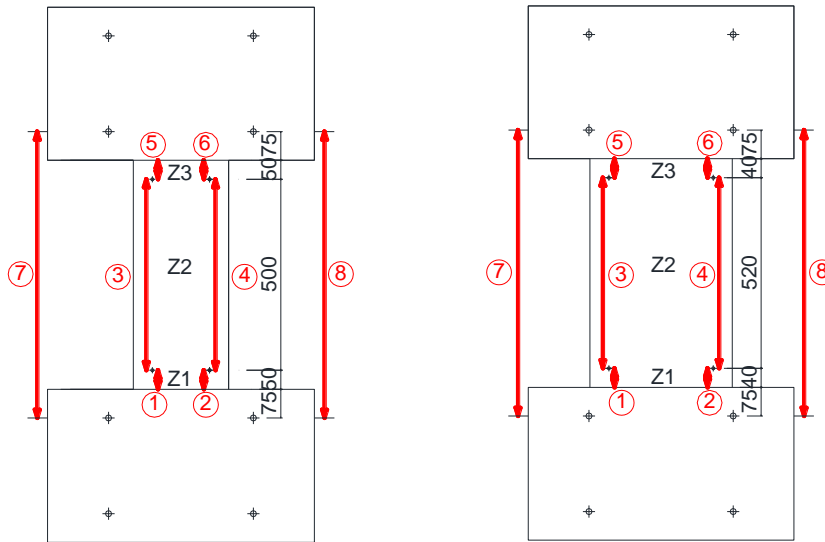
(a) B-type   (b) C-type

Figure 3.7 – Displacement gauges positions

3.7. Experimental Results and Discussion

3.7.1. Axial load-Axial Nominal Strain Relationships

Figure 3.8 shows axial load versus nominal axial strain relationships for all specimens. Each plot in the figure represents response relations for both monotonic and cyclic loading. The upper and lower dashed lines indicate, respectively, the calculated loads corresponding to the yielding of longitudinal reinforcements.

$$N_t = A_s f_y \qquad\qquad (3.2)$$

and the compressive strength as sum of the concrete uniaxial compressive strength and compressive yield stress of longitudinal reinforcement.

$$N_c = A_c f'_c + A_s f_y \qquad\qquad (3.3)$$

where A_c and A_s are the cross-sectional area of concrete gross section and longitudinal reinforcement, respectively, and f'_c and f_y are the concrete compressive cylinder strength and the yield strength of longitudinal reinforcement.

In C-type elements, vibration of concrete during concrete casting was conducted manually using steel rods since the use of vibrator was not possible due to the lack of space. Some small honeycombs were observed after removing the formwork. Hence, the unconfined compressive strength was not fully reached. It should be also noted that excessively large compressive strain for 6B-M and 6B-C elements was due to an inclination of the elements prior to extensive crushing. For all specimens, a stable response was observed under low levels of axial tensile strains for element tested under cyclic loading. However, increasing the tensile strain level led to different response. These differences and the comparison monotonic and cyclic loading response are summarized in the following.

It was noted that specimens with thin boundaries (C-type) were not able to fully develop the compressive strength. These configurations could not provide sufficient confinement although the transverse reinforcement ratio was high for 3C configuration. The low confinement ratio and large difference between longitudinal-to-transverse bar diameters led also to a lower compressive capacity. Comparison of load carrying capacity between monotonic and cyclic loadings showed no significant difference for all tested elements.

49
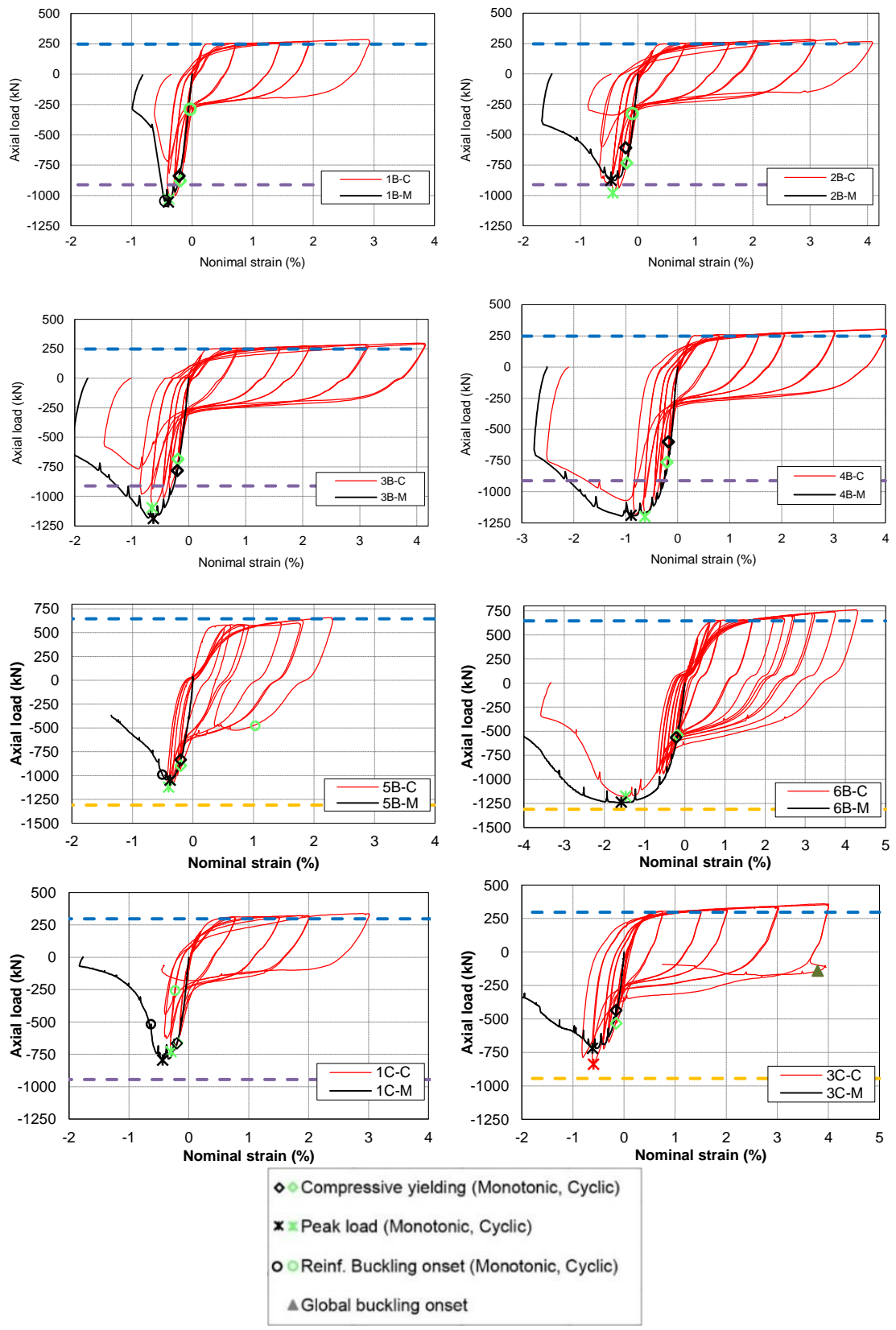
Figure 3.8 –Axial load-Nominal axial strain relationships

Failure of 1B, 5B and 1C configurations as well as 2B-C element was due to longitudinal reinforcing bar buckling. 3B, 4B and 6B configurations as well as 2B-M and 3C-M elements failed due to crushing of concrete, while global buckling failure was observed for 3C-C element. Failure mode due to buckling of reinforcement is indicated when apparent longitudinal bar buckling is observed with slight damage in only concrete surrounding longitudinal bars. Failure mode due to concrete crushing is indicated when extensive damage is observed in compressive concrete without any apparent longitudinal bars buckling.

Comparison between monotonic and cyclic response for elements with failure mode governed by buckling of longitudinal reinforcement (1B, 5B, and 1C configurations) showed that prior tensile strain affects considerably the load level at onset of bar buckling. Onset of bar buckling for elements tested under monotonic compression (1B-M, 5B-M and 1C-M) was noted around the peak point, followed by a rapid drop of the load carrying capacity and revealing that their failure was related to longitudinal bar buckling. Following bar buckling, the core concrete could not sustain the total axial load and extensive concrete crushing happened at bar buckling region. Response curves of elements that failed by buckling of longitudinal bars showed a quick decrease of axial load after the peak compressive load was reached. Figure 3.9 compares load-strain curve for B-type elements tested under monotonic load. A sudden drop of the capacity was observed and manifested by the rapid concrete crushing at the region of reinforcement buckling.
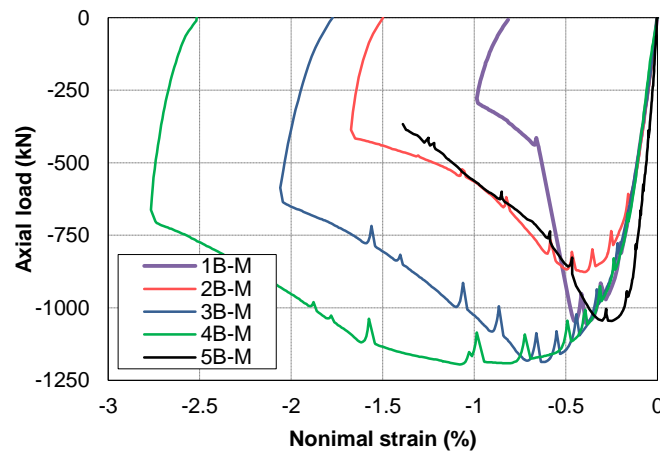
Figure 3.9 –Comparison of load- strain curves for B-type elements under monotonic load

On the other hand, elements tested under cyclic loading (1B-C, 5B-C and 1C-C) showed onset of bar buckling at lower compressive load before cracks completely closed following unloading from peak tensile strain. Onset of bar buckling for 1B-C element was

51

observed at approximately -220kN that correspond to about 80% less than the load level of bar buckling under monotonic compression. Onset of bar buckling happened after unloading from the first cycle of 2% tensile strain, similarly to 5B-C element. Onset of bar buckling for 1C-C element started when unloading from the second cycle of 1.5% tensile strain and loading to the corresponding compressive strain that is compressive strain corresponding to compressive peak load. The following cycle was marked by buckling of several longitudinal bars and capacity drop. This demonstrate vulnerability of slender elements to bar buckling. Response curves of elements that failed due to concrete crushing showed a smoother decrease of load carrying capacity compared to elements with failure mode by longitudinal bar buckling. This smooth decrease was more pronounced as the ratio of transverse reinforcement was higher.

Comparing densely and lightly confined specimens, it was shown that well confined specimens revealed capability to sustain larger tensile strain in a stable manner. However, dense transverse reinforcement detailing added little to the compressive capacity, especially for thin elements. Comparison of compressive capacity of 4B (ρ_t =1.27%) to 1B (ρ_t =0.22%) configurations showed an increased capacity of about 16%, while comparison between 3C (ρ_t =1.29%) and 1C (ρ_t = 0.22%) configurations display similar capacity even though the transverse reinforcement ratio in 3C was set more than 5 times of that in 1C. These observations suggest that it may not be even possible to provide enough confinement in thin sections by close transverse reinforcement spacing because the core concrete width is small and the pattern of concrete crushing indicates that compression strain concentrates over a short height.

Comparing the two levels of slenderness (B-type and C-type), it was shown that although they had similar confined area, the compressive load capacity of C-type elements was in the range of 25% to 40% less than the capacity of B-type elements. This was due to the thin core concrete in C-type elements where a similar confining effect to section with small aspect ratio cannot be obtained and spread of concrete crushing by confined core concrete could not be ensured. Imposing a minimum wall thickness would be an alternative means to suppress failures due to global buckling (Chai and Kunnath 2005) and maintain a stable compression zone.

3.7.2. Damage process and failure modes

Damage process is presented for each configuration under monotonic and cyclic loading conditions. All elements tested under monotonic compression exhibited a stable behavior without apparent damages until the peak load. Following the peak point, different damage evolutions and failures were observed. For cyclically tested elements, horizontal cracks appeared at top and bottom element-stub interface. They also appeared uniformly at transverse reinforcement planes when loading in tension, indicating that these cracks were initiated by the transverse reinforcement. Further tension loading led to widely opened horizontal cracks. Table 3.4 and

Table 3.5 give the numerical values for the observed damage states. Damage evolution and failure modes are described in the following.

3.7.2.1. B1-type specimens

Figure 3.10 shows the final damage situation for B1-type specimens. For 1B-M element subjected to monotonic compression, first cracks appeared near corner vertical reinforcing bars at the top region followed by the spalling of surrounding concrete and buckling of multiple longitudinal bars at this region with a buckling length corresponding to one transverse reinforcement spacing. On the other hand, 1B-C element started damage under compression by spalling of surface concrete at mid-height and the start of buckling of two corner bars with one transverse reinforcement spacing for buckling length. Extensive spalling of concrete was shown in the following compressive cycle with large buckling of longitudinal bars. Buckling length of corner and intermediate supported bars corresponded to one transverse reinforcement spacing while this buckling length for unsupported intermediate bars corresponded to more than two spacing. Crushing of concrete was not so severe at the buckling region following longitudinal reinforcement buckling.

For 2B-M element, damage started with the appearance of multiple vertical cracks at mid-height that quickly led to large spalling of surface concrete followed by crushing of concrete and buckling of several corner and intermediate longitudinal bars over one transverse reinforcement spacing. 2B-C started to damage under compression by the spalling of concrete around some corner bars at the middle and then at the top regions followed by buckling of longitudinal bars at those locations. At further compressive strains, extensive spalling of surface concrete between longitudinal reinforcing bars at mid-height region of the element occurred followed by buckling of many longitudinal bars over one transverse reinforcement spacing. A sudden concrete crushing at that region happened at final stage. A fracture of one longitudinal bar was observed when loading from 3% to 4% tensile strain. Failure modes of 2B configuration was different depending on loading type. 2B-M failed due to crushing of concrete, while failure of 2B-C was attributed to buckling of reinforcement that led to a sudden concrete crushing. Further large strains in tension and compression resulted in an increased number of regions were corner longitudinal bars buckled. This damage situation indicate that the pre-cracks at transverse reinforcement planes due to previous tension strains prior to compressive strain facilitates their buckling compared to element tested under monotonic compression.

3B-M started damage with the appearance of multiple vertical cracks at different locations around corner bars. Further compressive strains led to spalling of surface concrete and crushing of core concrete. For 3B-C, spalling of concrete around a pair of corner bars occurred with core concrete crushing at final stage at top region of the element. Damage

evolution for 4B-M and 4B-C elements was similar to 3B-M and 3B-C elements, respectively.

(a) 1B-M	(b) 1B-C	(c) 2B-M	(d) 2B-C
(e) 3B-M	(f) 3B-C	(g) 4B-M	(h) 4B-C
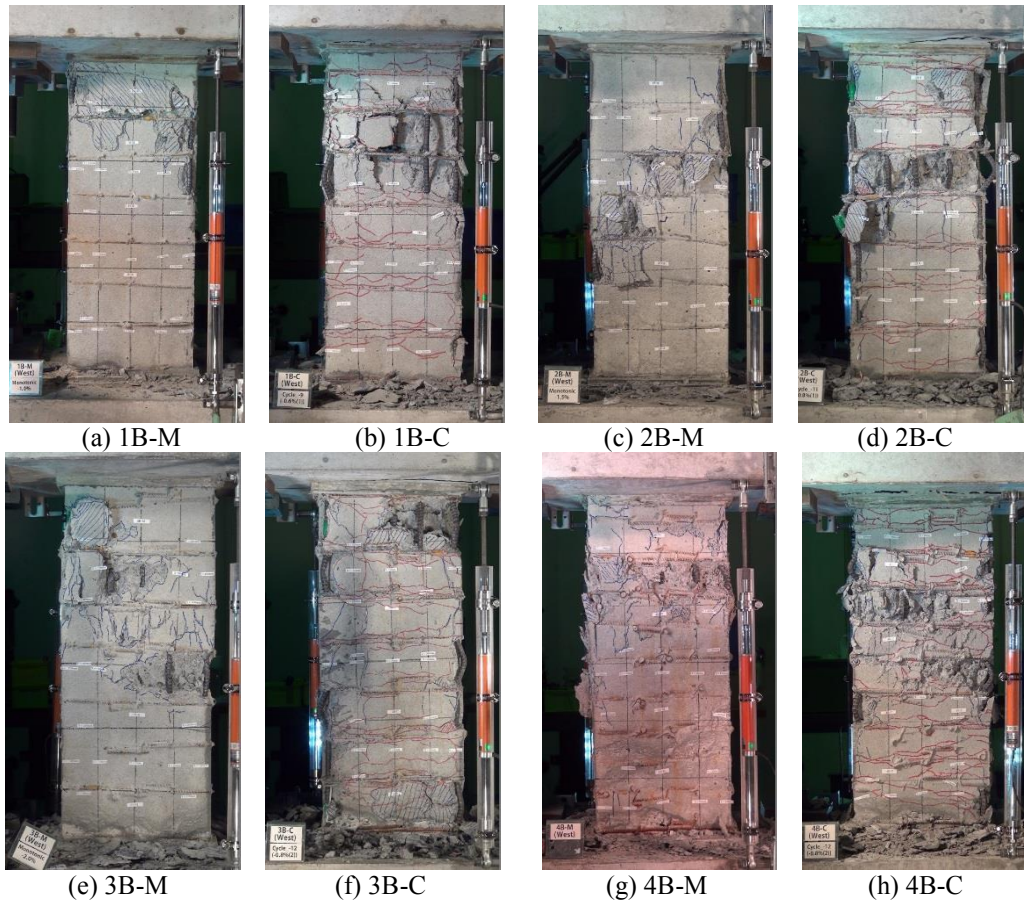
Figure 3.10 –Final damage situation for B1-type specimens

3.7.2.2. B2-type specimens

Figure 3.12 shows the final damage situation for B2-type and C-type specimens. For 5B-C, horizontal cracks opened widely and new horizontal cracks formed at mid-spacing between transverse reinforcement at further tensile strains. At final stage, buckling of multiple longitudinal reinforcing bars happened simultaneously at mid-height region over three and four spacing of transverse reinforcement after the spalling of surface concrete between longitudinal reinforcing bars. The transverse reinforcement (D4@80) was not able to contribute effectively in retaining larger longitudinal bars diameter (D16) and preventing them from buckling over large buckling length even though ratios of hoop spacing to longitudinal bar diameter, $s/d_b = 5$, is within the limit of ACI 318-14. This suggests that anti-buckling detailing provisions should also be related to the ratio of longitudinal-to-transverse bar diameters. Buckling of unsupported intermediate bars was more pronounced compared to other bars. 5B-M reached maximum capacity without visible damage, followed by spalling of concrete and buckling of longitudinal reinforcement over two and three transverse reinforcement spacing similarly to 5B-C element.

For 6B-C element, horizontal cracks appeared only at transverse reinforcement planes under tension loading and opened widely as tensile strain increased. At final loading stage, both 6B-C and 6B-M failed by crushing of compressive concrete followed by localized buckling of the damaged region, but no buckling of longitudinal reinforcement was observed. The damaged region was located at the lower portion for 6B-M and at the top for 6B-C.

<div align="center">

(a) 5B-M   (b) 5B-C   (c) 6B-M   (d) 6B-C
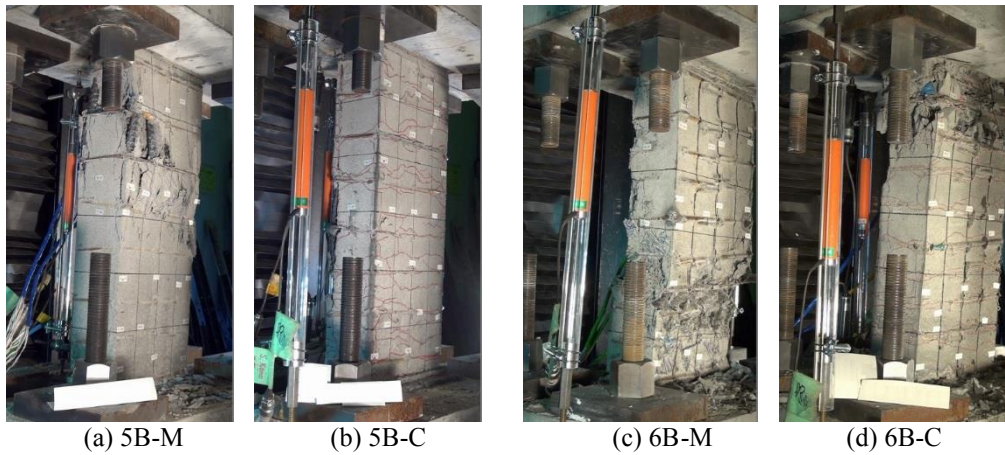
Figure 3.11 –Final damage situation for B2-type specimens
</div>

3.7.2.3. C-type specimens

Both 1C-C and 1C-M specimens failed by buckling of longitudinal reinforcement under compression. Buckling length was observed over two and three transverse reinforcement spacing for 1C-M, while it extended in 1C-C over more than four spacing of transverse reinforcement due to pre-cracks induced by tensile strain. Pre-cracking condition facilitates the buckling of longitudinal reinforcement in addition to the very thin concrete core. Similar to 5B configuration, buckling of unsupported intermediate bars was more pronounced than other bars, suggesting that restraining unsupported intermediate bars in the confined boundary region should be considered, especially for slender walls.

The final failure for 3C-M element was caused due to extensive crushing of compressive concrete at the bottom of element over a very limited height corresponding to approximately two transverse reinforcement spacing. Crushing of concrete for 3C-C was also concentrated at the bottom within limited height, similarly to 3C-M. However, crushing of concrete in 3C-C was followed by global buckling of the element when unloading from the second cycle of 4% tensile strain indicating that global buckling was driven by prior induced large tensile strain. This phenomenon demonstrates the vulnerability of confined boundaries of slender walls to tensile strain excursions prior to compressive strain. Concrete crushing was very limited in height compared to B-type specimens.

In specimens failing due to concrete crushing, concrete crushed over a height ranging approximately between 2 to 3 times element widths. Fracture under tension of

longitudinal reinforcing bars was not observed excluding one longitudinal bars for 2B-C at tensile strain larger than 3%. Globally, no difference of the failure modes were shown when comparing failures under monotonic and cyclic loading condition. Exception was noted for 2B and 3C configurations. 2B-M failed due to crushing of concrete, but failure of 2B-C was due to buckling of reinforcement that led to a sudden concrete crushing. In addition, 3C-M failed due to extensive crushing of concrete, while 3C-C element showed a limited concrete crushing region at the base followed by out-of-plane buckling. Prior crushing assisted the global buckling over almost the total height of the element and resulted in a large out-of-plane displacement.

| (e) 1C-M | (f) 1C-C | (g) 3C-M | (h) 3C-C |
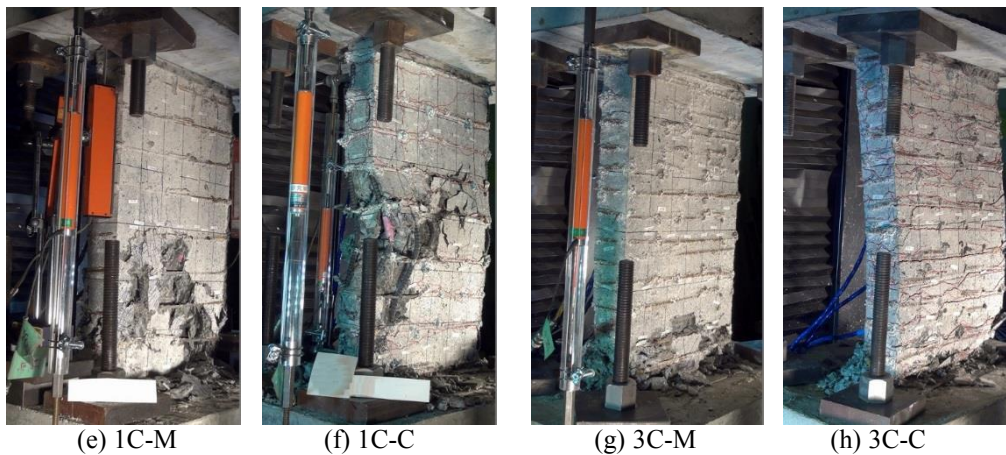
Figure 3.12 –Final damage situation for C-type specimens

Table 3.4 – Numerical values for observed damage states for B1-type elements

Specimen		Reinf. Comp. Yield.	Peak	Reinf. Buckl.	Global Buckl.	Failure Mode
1B-M	Load (kN)	-839.3	-1053.2	-1045.3	-	Reinf. Buckling
	Strain (%)	-0.2135	-0.391	-0.4425	-	
1B-C	Load (kN)	-879.4	-1027.6	-290.2	-	Reinf. Buckling
	Strain (%)	-0.192	-0.378	-0.033	-	
2B-M	Load (kN)	-607.2	-876	-	-	Concrete Crushing
	Strain (%)	-0.2115	-0.4655	-	-	
2B-C	Load (kN)	-733.5	-978.8	-327.3	-	Reinf. Buckling
	Strain (%)	-0.1945	-0.4355	-0.0985	-	
3B-M	Load (kN)	-781.2	-1186.8	-	-	Concrete Crushing
	Strain (%)	-0.199	-0.6185	-	-	
3B-C	Load (kN)	-685.9	-1095.4	-	-	Concrete Crushing
	Strain (%)	-0.188	-0.6415	-	-	
4B-M	Load (kN)	-601	-1189.7	-	-	Concrete Crushing
	Strain (%)	-0.18	-0.897	-	-	
4B-C	Laod (kN)	-763.7	-1201.5	-	-	Concrete Crushing
	Strain (%)	-0.205	-0.6295	-	-	

Table 3.5 – Numerical values for observed damage states for B2- and C-types

Specimen		Reinf. Comp. Yield.	Peak	Reinf. Buckl.	Global Buckl.	Failure Mode
5B-M	Load (kN)	-834.2	-1045.3	-989.3	-	Reinf. Buckling
	Strain (%)	-0.2005	-0.377	-0.5055	-	
5B-C	Load (kN)	-894	-1120.8	-477.3	-	Reinf. Buckling
	Strain (%)	-0.201	-0.4045	1.032	-	
6B-M	Load (kN)	-565.2	-1237.2	-	-	Concrete Crushing
	Strain (%)	-0.2105	-1.5775	-	-	
6B-C	Load (kN)	-540.8	-1175	-	-	Concrete Crushing
	Strain (%)	-0.176	-1.468	-	-	
1C-M	Load (kN)	-664.9	-795	-517.7	-	Reinf. Buckling
	Strain (%)	-0.1995	-0.436	-0.628	-	
1C-C	Load (kN)	-662.1	-730	-256.8	-	Reinf. Buckling
	Strain (%)	-0.1885	-0.2985	-0.226	-	
3C-M	Load (kN)	-435.7	-719.4	-	-	Concrete Crushing
	Strain (%)	-0.151	-0.618	-	-	
3C-C	Load (kN)	-532.1	-838.6	-	-140.5	Concrete Crushing
	Strain (%)	-0.1495	-0.5975	-	3.794	

3.8. Conclusions

An experimental study was conducted on sixteen RC rectangular columns that idealize confined boundaries of RC rectangular walls to examine the effects of slenderness, reinforcement detailing and loading type on their performance under monotonic and cyclic reversed axial loading. The following conclusions were drawn.

- Three different failure modes were observed depending on confinement and slenderness levels: crushing of compressive concrete, buckling of longitudinal reinforcement, and global buckling of element. Although load carrying capacity between monotonic and cyclic loadings showed no significant difference, loading type may lead to different final failure mode.
- Dense transverse reinforcement detailing in thin confined boundaries did not improve the performance of walls. Imposing a minimum wall thickness would be an alternative means to suppress failures due to global buckling of thin walls and efficiently use the confinement. It was also shown that failure due to global buckling was affected by both large tensile strain prior to compressive strain and prior crushing of compressive concrete.
- Large transverse reinforcement spacing may result in buckling of longitudinal reinforcement following even limited tensile strain excursions. Intermediate unsupported bars are more susceptible to buckling. Supporting all intermediate bars

at the wall confined boundary should be considered. Comparison between monotonic and cyclic response for elements with failure mode governed by buckling of longitudinal reinforcement showed that prior tensile strain reduced considerably the load level at the onset of bars buckling.

References

1. Chai, Y. H., Elayer, D. T., (1999), "Lateral stability of reinforced concrete columns under axial reversed cyclic tension and compression", ACI Structural Journal, 96(5): 780–790.

2. Markeset, G. Hillerborg, A., (1995), "Softening of concrete in compression localization and size effects", Cement and Concrete Research, 25(4), 702–708.

3. Takahashi S., Yoshida K., Ichinose T., Sanada Y., Matsumoto K., Fukuyama H. and Suwada H., (2013), "Flexural drift capacity of reinforced concrete wall with limited confinement", ACI Structural Journal, 110(1), 95−104.

CHAPTER 4 ANALYTICAL AND NUMERICAL STUDIES ON CONFINED BOUNDARY ELEMENTS

4.1. Introduction

When properly designed and detailed, RC walls are expected to behave in a ductile flexural manner to resist high seismic demands. This expected behavior is based on the practice of detailing reinforced concrete structural walls to be tension-controlled by maintaining a stable compression zone. To achieve this goal, instabilities due to global buckling of wall boundaries or buckling of longitudinal reinforcement in confined boundaries should be prevented.

This chapter presents evaluation of design and detailing rules to prevent global buckling and reinforcement bar buckling in confined boundaries. A longitudinal-to-transverse reinforcement index is proposed as anti-buckling measure of reinforcement.

In order to simulate the hysteretic behavior of cyclically tested elements, an accurate and reliable prediction of experimentally observed response is proposed. The model addresses important issues of the hysteretic behavior in both cyclic compression and tension. The analytical model includes bar buckling.

4.2. Prediction of failure modes and damage situations

4.2.1. Potential of out-of-plane buckling

Figure 4.1 shows the final buckled shape of 3C-C. A vertical line was drawn to highlight the transverse displacement of the buckled element in the figure. Wide cracks, which developed at transverse reinforcement planes resulted from large yield excursion, did not close prior to full development of maximum compressive strength due to residual tensile strain in the previously yielded longitudinal reinforcement. This damage situation caused

a critical condition affecting the lateral stability (Paulay and Priestley 1993, Chai and Elayer 1999). However, crushing of concrete at the base of 3C-C prior to global buckling contributed in a large out-of-plane displacement when unloading from the second cycle of 4% tensile strain since the base acted as a pin joint. This reveals that both large tensile strain prior to compressive strain and prior crushing affect the global buckling failure mode for slender walls. Imposing a minimum wall thickness would be an alternative means to eliminate global buckling.

Figure 4.1 –Final buckling shape of 3C-C

Buckling may not be easily perceptible at the design level because their mechanism is difficult to quantify even with the current analysis capabilities. Tendency to buckle in RC walls depend primarily on the wall slenderness ratio and loading history or specifically the maximum tensile strain in the boundary longitudinal reinforcement. Parra and Moehle (2014) suggested that buckling instability might be related to two damage situations. One is that tensile yielding softens the boundary in one direction for subsequent loading in the opposite direction under compression, leading to global lateral instability of an intact wall. The second is that the wall crushes first, leaving an even smaller and irregular cross-section, leading to instability of the reduced cross section as a secondary buckling failure. However, failure of 3C-C showed a third damage situation, where prior crushing at the bottom led to a global buckling rather than a local buckling of the crushed region.

Based on buckling theory for prismatic sections under cyclic loading, a relation between the critical slenderness ratio for the wall boundary element and the maximum tensile strain prior to compressive load, ε_{sm}, was proposed as Eq. (4.1) (Paulay and Priestley 1993, Chai and Elayed 1999, Parra and Moehle 2014).

$$\frac{b_{cr}}{kh_0} = \frac{1}{\pi}\sqrt{\frac{\varepsilon_{sm}-0.005}{\beta\xi}} \tag{4.1}$$

where b_{cr} is the critical wall boundary thickness, h_0 is the clear height, β is the effective depth parameter for longitudinal reinforcement assumed to be 0.8 for two layers of longitudinal bars and 0.5 when a single central layer of bars is used, and ξ is a parameter related to mechanical reinforcement ratio that should satisfy:

$$\xi \le 0.5\left(1+\frac{2m}{0.85}-\sqrt{\left(\frac{2m}{0.85}\right)^2+\frac{4m}{0.85}}\right) \tag{4.2}$$

with $m=\rho_l f_y/f'_c$ is the mechanical reinforcing ratio. For practical design, Parra and Moehle (2014) suggested that $\xi=0.25$. Eq.(4.1) becomes then:

$$\frac{kh_0}{b_{cr}} = \frac{1}{0.7\sqrt{\varepsilon_{sm}-0.005}} \tag{4.3}$$

Assuming fixity at top and bottom, the effective length is $kh_0=0.5h_0$, Figure 4.2 compares theoretical relation for wall instability given by Eq. (4.3) and element test results. A value of β equal to 1.0 was used in Eq. (4.1) to consider the total thickness since the specimens were built without cover concrete. The equation may be used to judge the potential of global buckling.
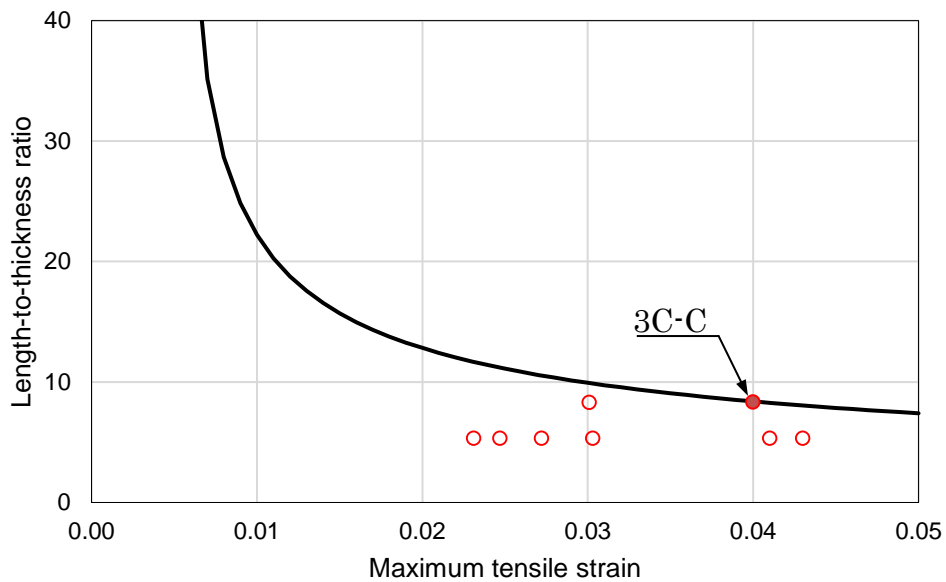
Figure 4.2 – Comparison with theoretical relation for global buckling instability

4.2.2. Potential of longitudinal bars buckling

Buckling of longitudinal reinforcing bars are usually addressed by limiting the ratio of transverse reinforcement spacing to longitudinal bar diameter, s/d_b. Large s/d_b ratios result in limited confinement of concrete, and leave longitudinal reinforcement more vulnerable to buckling instability. ACI 318-14 limits the ratio of s/d_b to 6. Rodriguez *et al.* (1999) introduced a criterion to assess the onset of bar buckling based on monotonic and cyclic tests on isolated reinforcing bars with various s/d_b ratios. Tests indicated that bars subjected to cyclic loading were more susceptible to buckling failures than bars subjected to monotonic loading. A strain parameter was introduced as an indicator of the onset of bar buckling. However, this approach is limited to s/d_b ratio equal to 8 and does not take into account buckling susceptibility over multiple transverse reinforcement spacing.

4.2.2.1. Kato's transverse reinforcement index

Based on quasi-static tests on RC columns subjected to lateral loads and constant or varying axial load, Kato *et al.* (1995) proposed a model to estimate the buckling length and the onset of inelastic buckling of corner reinforcing bars. The buckling length is given as a function of the number of transverse reinforcement spacing over where the buckling of longitudinal reinforcement is likely to happen. Transverse reinforcement index, α, was also proposed as a design rule to prevent buckling of longitudinal bars given as:

$$\alpha = \frac{(A_w/A_l)(f_{wy}/f_y)}{s/d_b} \geq 0.039 \tag{4.4}$$

where A_w and A_l are the areas of transverse and longitudinal reinforcement, respectively, f_{wy} and f_y are yield stress of transverse and longitudinal reinforcement, respectively, and s/d_b is the ratio of transverse reinforcement spacing to longitudinal bar diameter. Figure 4.3 shows relation between transverse reinforcement index and observed failure mode for cyclically tested element.
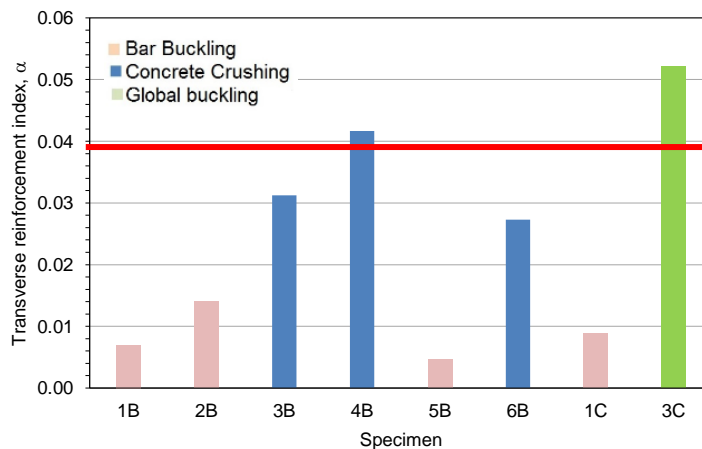
Figure 4.3 – Transverse reinforcement index for tested elements based on Kato *et al.* (1995)

Although the lower limit of 0.039 for the index of transverse reinforcement seems to be conservative, the index was able to predict the vulnerable specimens to buckling of longitudinal reinforcement as those with the lower transverse reinforcement ratios. Configuration 5B with the lowest index, showed the most drastic failure due to buckling of longitudinal bars, while buckling of longitudinal reinforcement for configuration 2B was only observed for 2B-C tested under cyclic loading. Among the tested configurations, 2B was considered as a limit between failure due to longitudinal bars buckling and failure by concrete crushing.

4.2.2.2. Proposed longitudinal-to-transverse reinforcement index

In 5B configuration, transverse reinforcement did not effectively retain longitudinal bars and prevent them from buckling over large buckling length even though ratios of hoop spacing to longitudinal bar diameter, $s/d_b = 5$, is within the limit of the ACI 318-14. This suggests that anti-buckling detailing provisions should also be related to the ratio of longitudinal-to-transverse bar diameters. Figure 4.4 shows relation between longitudinal-to-transverse reinforcement bar diameters times transverse reinforcement ratio as an index to measure the effectiveness of transverse reinforcement to prevent bar buckling. The index was also able to predict vulnerable specimens to bar buckling. A limit of 1.2 is suggested and this index is considered as complementary to previous rules for preventing bar buckling.

$$\rho_t \frac{d_b}{d_t} \geq 1.2 \tag{4.5}$$

with ρ_t is the transverse reinforcement ratio in confined boundary (%), d_b is the longitudinal reinforcing bar diameter, and d_t is the transverse reinforcing bar diameter.
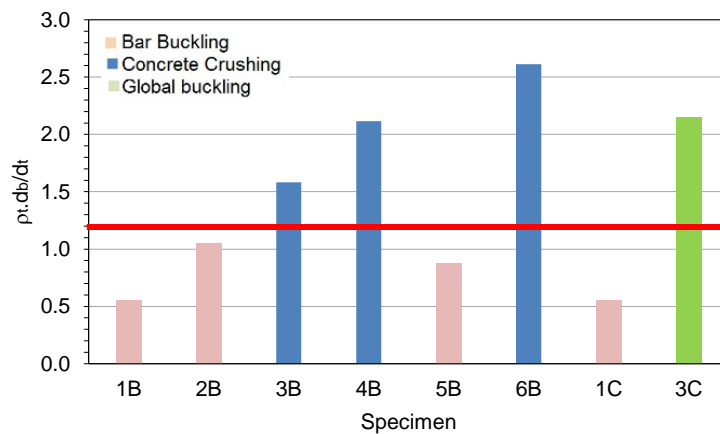
Figure 4.4 – Proposed longitudinal-to-transverse reinforcement index

The proposed longitudinal-to-transverse reinforcement index needs to be validated with more experimental data. However, literature review on existing prism tests focused on

global buckling of wall boundary rather that buckling of longitudinal reinforcement, and most specimens failed due to buckling of longitudinal reinforcement were tested without transverse reinforcement which do not represent the actual construction practice.

4.3. Analytical prediction of load - Strain relations

In order to simulate the hysteretic behavior of cyclically tested elements, an accurate and reliable prediction of experimentally observed response is proposed. The model addresses important issues such as the hysteretic behavior in both cyclic compression and tension; the progressive degradation of stiffness of the unloading and reloading curves for increasing values of strain; and the effects of confinement, tension stiffening, and gradual crack closure. The model takes into account concrete damage and hysteresis, while retaining computational efficiency.

4.3.1. Materials models

The monotonic envelope curve of the hysteretic model for concrete in compression follows the monotonic stress-strain relation of modified Kent and Park model (Scott *et al.* 1982) offering a good balance between simplicity and accuracy (Figure 4.5(a)) . The hysteretic behavior of concrete in both compression and tension were modeled using hysteretic unloading and reloading rules proposed by Yassin (1994) as a set of linear stress-strain relations. The model is able to simulate stiffness degradation for both unloading and reloading. The model provides the flexibility to represent the hysteretic behavior of confined and unconfined concrete in both cyclic compression and tension (Figure 4.5(b)).
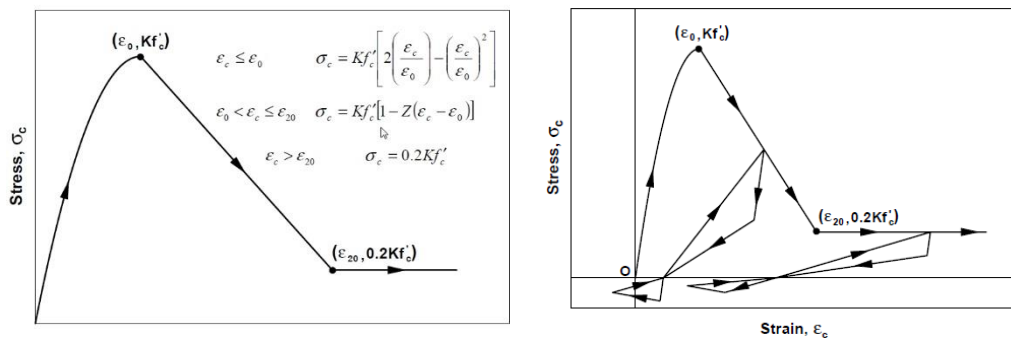
(a) Envelope curve (Scott *et al.*, 1982)   (b) Hysteretic rules (Yassin, 1994)
Figure 4.5 –Stress-strain relations for concrete

The numerical model used for reinforcing steel was based on Menegotto-Pinto model (Menegotto and Pinto 1973). It was extended by Filippou *et al.* (1983) to include isotropic strain hardening effects as shown in Figure 4.6. To include the effect of buckling of reinforcement, Dhakal and Maekawa (Dhakal and Maekawa, 2002) model was implemented. Based on a calibration with experimental data, Dhakal and Maekawa model

explicitly provides the compressive stress - strain response of the rebar that is linear for pre-yielding branch and follow Eq.(4.6) and Eq.(4.7) for post-yield behavior (Figure 4.7).

$$\frac{\sigma_{sc}}{\sigma_t} = 1 - \left(1 - \frac{f_i}{f_{it}}\right)\left(\frac{\varepsilon_{sc} - \varepsilon_y}{\varepsilon_i - \varepsilon_y}\right) \qquad \text{for} \quad \varepsilon_y < \varepsilon_{sc} \leq \varepsilon_i \tag{4.6}$$

$$\sigma_{sc} = f_i - 0.02E_s(\varepsilon_{sc} - \varepsilon_i) \geq 0.2 f_y \qquad \text{for} \qquad \varepsilon_{sc} > \varepsilon_i \tag{4.7}$$

where σ_t and f_{it} are the stresses in the tension envelope corresponding to ε_{sc} (current strain) and ε_i (strain at the intermediate point), respectively. f_y and ε_y are yielding stress and strain, respectively. The coordinates of intermediate point correlated to $\sqrt{f_y}\, L/d_b$ are given by:

$$\frac{\varepsilon_i}{\varepsilon_y} = 55 - 2.3\sqrt{\frac{f_y}{100}}\frac{L}{d_b} \geq 7 \tag{4.8}$$

$$\frac{f_i}{f_{it}} = \alpha\left(1.1 - 0.016\sqrt{\frac{f_y}{100}}\frac{L}{d_b}\right); \frac{f_i}{f_y} \geq 0.2 \tag{4.9}$$

where α is a coefficient that takes into account strain hardening which is equal to 0.75 for elastic-perfectly plastic bars, and 1.0 for bars with continues linear hardening. L/d_b is the ratio of the buckling length to the longitudinal bar diameter. Buckling length of reinforcement was evaluated based on Kato *et al.* (1995). Buckling length were evaluated as three transverse reinforcement spacing for specimens failing due to buckling of reinforcement, and one transverse reinforcement spacing for specimens failing due to concrete crushing of global buckling.
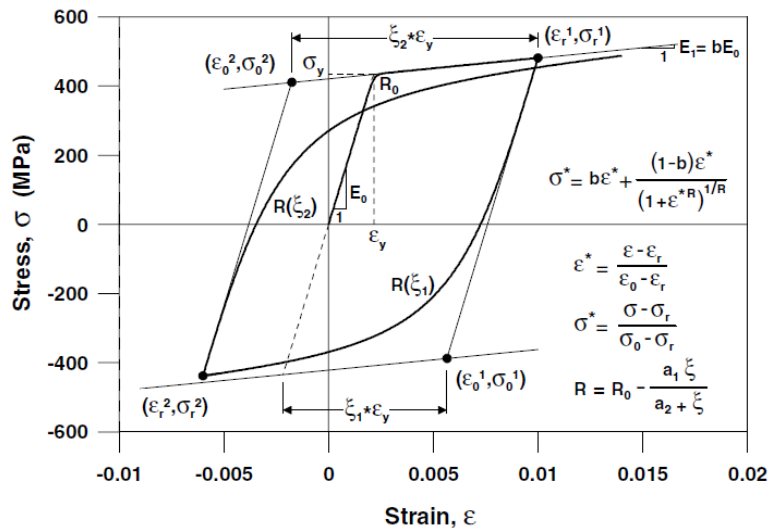
Figure 4.6 –Stress-strain relations for reinforcing bars based on Menegotto-Pinto model
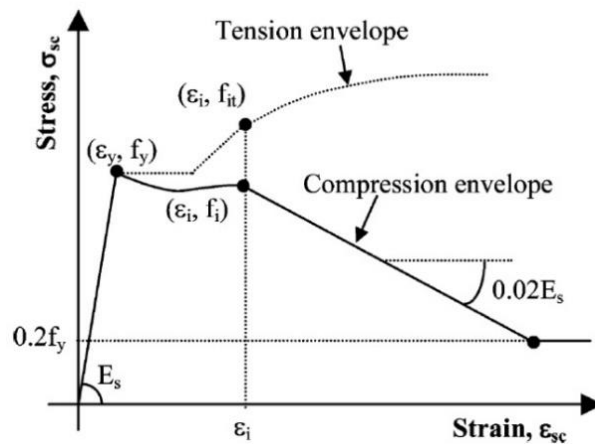
Figure 4.7 –Reinforcement monotonic compressive buckling model (Dhakal and Maekawa, 2002)

Procedure for design and evaluation of confined boundary elements

Figure 4.8 shows the procedure followed to determine the compressive strength. Global buckling vulnerability is judge using Eq.(4.3), and reinforcement buckling is assessed based on the longitudinal-to-transverse reinforcement index and the ratio of transverse reinforcement spacing to longitudinal bar diameter, buckling model is considered to determine the compressive strength. $_sN_{max}$ and $_{sb}N_{max}$ are simulated peak load without and with buckling effect, respectively. Figure 4.9 shows an example for 1C-C element with and without considering reinforcement buckling effect. The figure shows clearly the importance of considering reinforcement buckling effect in predicting compressive strength of element. The ratio of experimental to simulated compressive strength is equal to 0.96 and 0.97 for, respectively, 1C-C and 5B-C specimens when considering reinforcement buckling effect, while this ratio is equal to 0.76 and 0.85 when buckling effect is not considered.
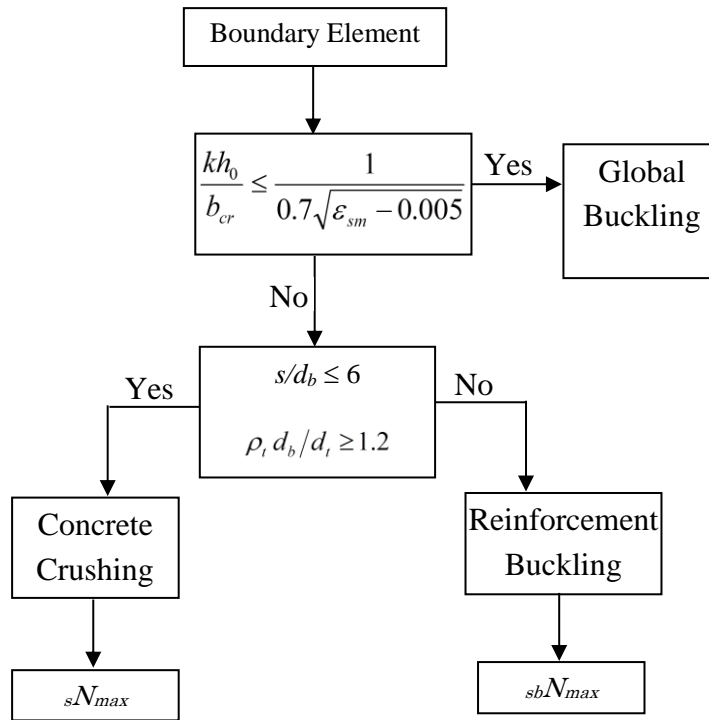
Figure 4.8 –Procedure to determine compressive strength

(a)   (b)
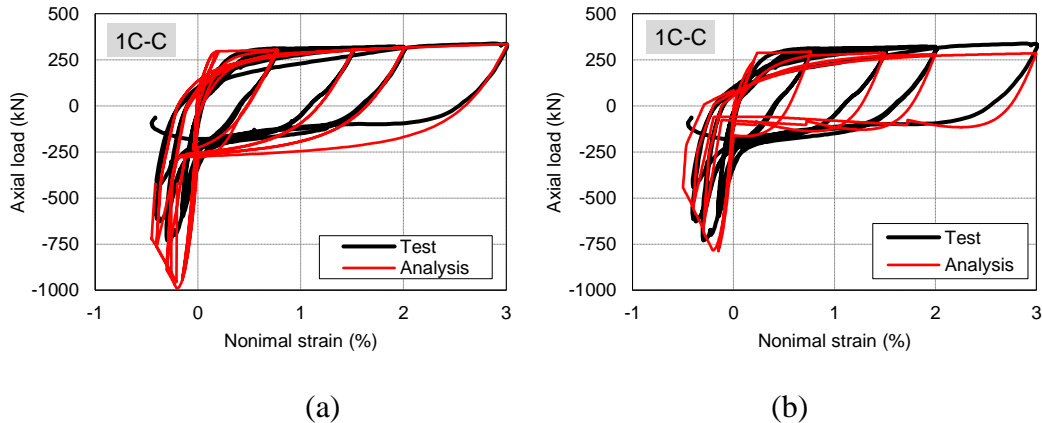
Figure 4.9 –Measured and predicted cyclic axial load – axial strain relations for 1C-C element (a) without considering buckling and (b) with buckling

4.3.2. Simulation results and discussion

Figure 4.10 and Figure 4.11 show comparison between experimental and analytical axial load – axial strain for specimens tested under cyclic and monotonic loading, respectively. Table 4.1 compares compressive strength point and corresponding strain. The analytical model for cyclically tested specimens captures reasonably well the measured response with hysteretic shape of the response and stiffness degradation. The cyclic properties of the implemented analytical stress-strain relations for steel and concrete produced good correlation for global response, and was able to predict the compressive strength reduction for specimens failing due to reinforcing bar buckling. For specimens tested under monotonic loading, although compressive strength was overestimated especially for specimens failing due to concrete crushing and global buckling, the model well simulated the post peak branch for specimens failing due to reinforcement buckling.

Table 4.1 – Comparison between experimental and simulated peak load and strain

Specimen	Experiment			Numerical Simulation				Comparison	
	$_eN_{max}$ (kN)	$_e\varepsilon_{@max}$ (%)	Failure mode	$_cN_{max}$ (kN)	$_sN_{max}$ (kN)	$_{sb}N_{max}$ (kN)	$_s\varepsilon_{@max}$ (%)	$_eN_{max}$ $/_{sb}N_{max}$	$_e\varepsilon_{@max}$ $/_s\varepsilon_{@max}$
1B-M	-1053	-0.391	RB		-957	-957	-0.206	1.10	1.90
1B-C	-1029	-0.378	RB		-946	-815	-0.203	1.26	1.86
2B-M	-876	-0.466	CC		-977	-977	-0.208	0.90	2.24
2B-C	-979	-0.435	RB	-912	-968	-878	-0.208	1.12	2.09
3B-M	-1187	-0.619	CC		-1030	-1030	-0.225	1.15	2.75
3B-C	-1095	-0.642	CC		-1101	-1101	-0.218	0.99	2.94
4B-M	-1195	-0.630	CC		-1062	-1062	-0.236	1.13	2.67
4B-C	-1202	-0.897	CC		-1051	-1051	-0.240	1.14	3.74
5B-M	-1045	-0.249	RB		-1350	-1350	-0.202	0.77	1.23
5B-C	-1121	-0.278	RB	-1310	-1309	-1158	-0.201	0.97	1.38
6B-M	-1237	-1.578	CC		-1398	-1398	-0.228	0.88	/
6B-C	-1175	-1.468	CC		-1392	-1392	-0.281	0.84	/
1C-M	-795	-0.436	RB	-944	-990	-987	-0.206	0.81	2.12
1C-C	-755	-0.299	RB		-990	-789	-0.206	0.96	1.45

Note: $_eN_{max}$ and $_e\varepsilon_{@max}$ are experimental peak load and corresponding strain, respectively. N_c compressive load capacity based on uniaxial concrete strength and longitudinal reinforcement yielding. $_sN_{max}$ and $_{sb}N_{max}$ are simulated peak load without and with reinforcement buckling effect, respectively, and $_s\varepsilon_{@max}$ is the corresponding peak strain. CC: Concrete Crushing, RB: Reinforcement Buckling, GB: Global Buckling.
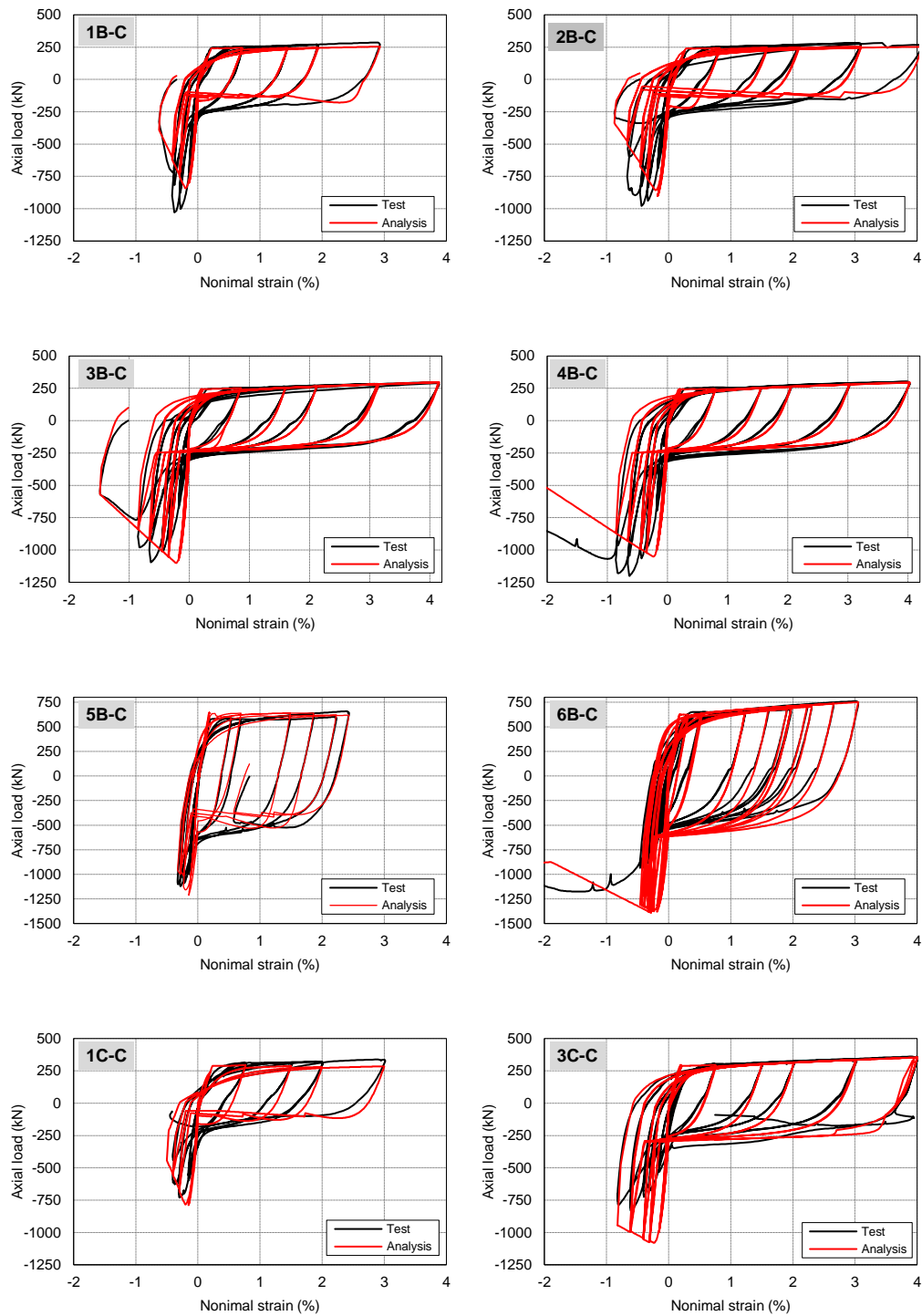
Figure 4.10 –Measured and predicted cyclic axial load – axial strain relations

70
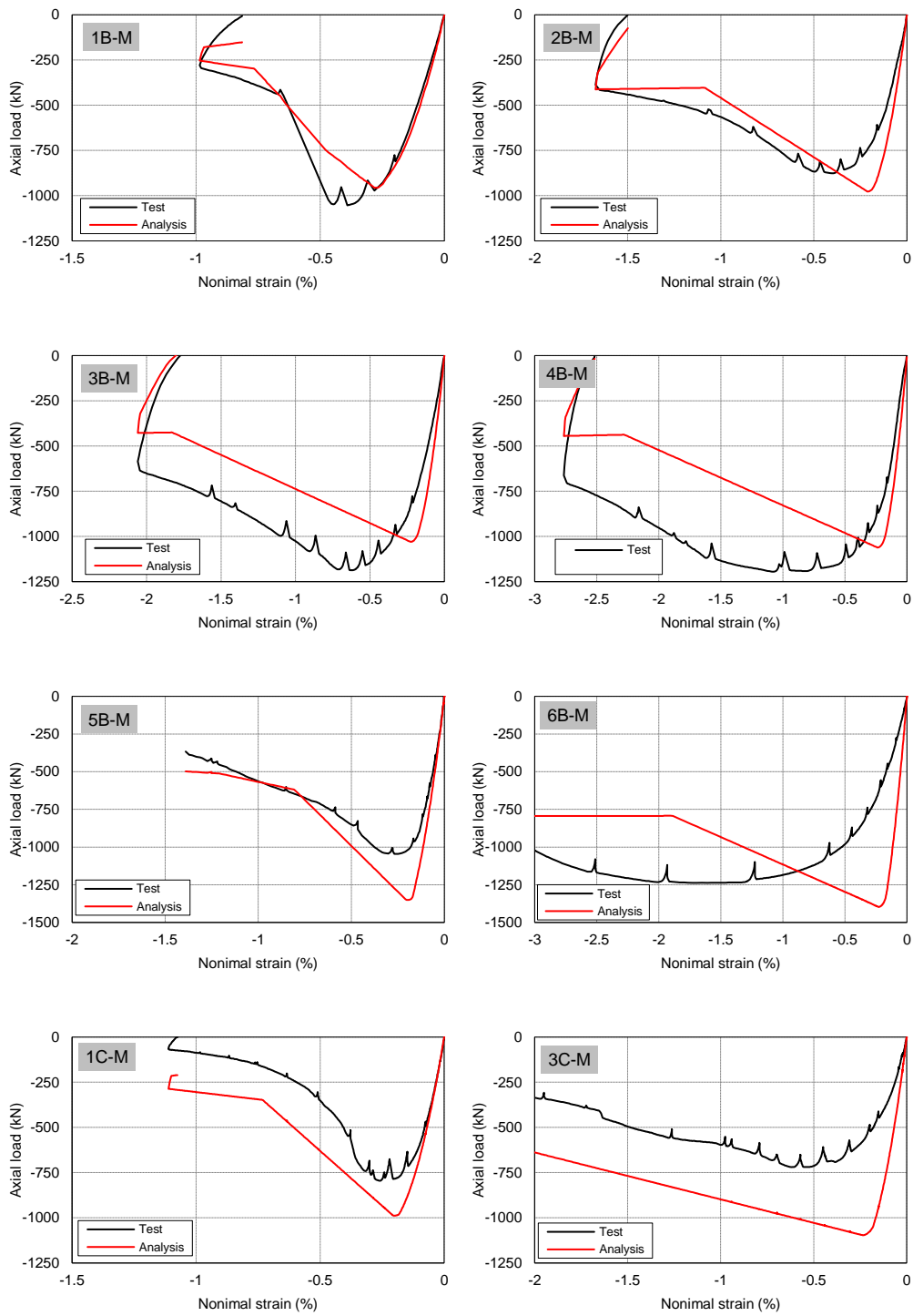
Figure 4.11 –Measured and predicted monotonic axial load – axial strain relations

4.4. Conclusions

Design and detailing rules for RC walls confined boundary were evaluated. Analytical model was developed to simulate hysteretic behavior of isolated confined boundary elements. From this study, the following conclusions were drawn.

- Considering the maximum usable tensile strain is approximately 0.05, the practical range for critical slenderness ratio is limited by approximately 13.5. For practical design, the limiting slenderness ratio of $h_u/b = 16$, as specified in the 1997 Uniform Building Code. (UBC, 97) is recommended.
- The proposed longitudinal-to-transverse reinforcement index along with the ratio of transverse reinforcement spacing to longitudinal bar diameter present a simple but effective anti-buckling measures of reinforcement.
- The proposed longitudinal-to-transverse reinforcement index needs to be validated with more experimental data. However, literature review on existing prism tests focused on global buckling of wall boundary rather that buckling of longitudinal reinforcement, and most specimens failed due to buckling of longitudinal reinforcement were tested without transverse reinforcement which do not represent the actual construction practice.
- An analytical model that include bar buckling was proposed to predict cyclic response of tested specimens. The analytical model captures reasonably well the measured response and was also able to predict the compressive strength reduction for specimens failing due to reinforcing bar buckling.
- A procedure was proposed for the design and evaluation of RC walls confined boundaries to prevent or evaluate global buckling and reinforcement buckling vulnerabilities.

References

1. ACI, (2014), "Building code requirements for structural concrete (ACI 318-14) and commentary (ACI318R-14)", American Concrete Institute, MI, USA.

2. Chai, Y. H., Elayer, D. T., (1999), "Lateral stability of reinforced concrete columns under axial reversed cyclic tension and compression", ACI Structural Journal, 96(5): 780–790.

3. Dhakal R. P., Maekawa K., (2002), "Path-dependent cyclic stress–strain relationship of reinforcing bar including buckling", Engineering Structures, 24(11): 1383–1396.

4. Filippou, F. C., Popov, E. G., Bertero, V. V., (1983), "Effects of bond deterioration on hysteretic behavior of reinforced concrete joints", EERC Report No. UCB/EERC-83/19, Earthquake Engineering Research Center, University of California, Berkeley.

5. Kato, D., Kanaya, J., Wakatsuki, K., Honda, Y., (1995), "Design method to prevent buckling of main bars in RC members", Pacific Conference on Earthquake Engineering, Melbourne 20-22 November.

6. Menegotto, M., Pinto, E., (1973), "Method of analysis for cyclically loaded reinforced concrete plane frames including changes in geometry and non-elastic behavior of elements under combined normal force and bending", Proceedings of IABSE Symposium on Resistance and Ultimate Deformability of Structures Acted on by Well-Defined Repeated Loads, Lisbon, 1973, pp. 15–20.

7. Parra, P. F., Moehle, J. P., (2014), "Lateral buckling in reinforced concrete walls", Proceedings of the 10th U.S. National Conference on Earthquake Engineering, Anchorage 21–25 July 2014.

8. Paulay, T., Priestley, M. J. N., (1993), "Stability of Ductile Structural Walls", ACI Structural Journal, 90(4): 385-392.

9. Rodriguez, M. E, Botero, J. C., Villa, J., (1999), "Cyclic stress-strain behavior of reinforcing steel including effect of buckling", ASCE Journal of Structural Engineering, 125(6), 605–612.

10. Scott, B. D., Park R., Priestley, M. J. N., (1982), "Stress-strain behavior of concrete confined by overlapping hoops at low and high strain rates", Journal of the American Concrete Institute, 79(1), 13–27.

11. Yassin, M. H. M., (1994). "Nonlinear analysis of prestressed concrete structures under monotonic and cyclic loads", PhD Thesis, University of California, Berkeley.

CHAPTER 5 EXPERIMENTAL AND ANALYTICAL STUDY ON RC STRUCTURAL WALLS WITH CONFINED BOUNDARIES

5.1. Introduction

When RC structural walls are required to withstand the effects of large earthquakes, the wall ductility under lateral loading is considered as a measure of the structural performance and is a key parameter in the current seismic design codes. While modern architectural demand has been requiring design engineers to produce slender walls with higher load and drift capacities, observed damages of RC wall buildings in recent earthquakes in Chile and New Zealand raised concerns about the seismic performance of rectangular RC walls. To address issues related to these observations, an experimental study was conducted to study the effects of end region confinement on the seismic performance of cantilever structural walls. Seven 40%-scale cantilever type structural walls having different cross sectional configurations and transverse reinforcement at the end regions of the walls were constructed and tested under lateral cyclic reversed loading. The test specimens included two specimens with boundary columns and five specimens with rectangular section. Primary test variables included cross sectional shape (rectangular and barbell shape), transverse reinforcement ratio in confined end regions, shear span-to-wall length ratio, and axial load ratio.

This chapter aims also to develop a fiber-based sectional analysis model to simulate observed hysteretic responses. The model is based on the plastic hinge length and moment-curvature analysis, and takes into account flexural, shear and strain penetration drift components.

5.2. Experimental Program

5.2.1. Description of Test Specimens

Seven 40% scale RC structural walls with different section configurations and detailing in confined end regions, as shown in Figure 5.1 and Figure 5.2, were constructed and tested under combined constant axial load and reversed cyclic lateral load. Primary test variables included sectional shape (two barbell-shape walls and five rectangular walls), transverse reinforcement ratio in confined end regions, shear span-to-wall length ratio (1.71 and 1.37), axial load level (0.1 and 0.2), and wall shear safety ratio. Wall specimens BC40 and BC80 had boundary columns while other wall specimens had rectangular sections with confined end regions. As can be seen from Table 5.1, all specimens had same wall length (1750mm). Wall thicknesses of rectangular walls were 120 mm and 128mm for 1.71 (NC40 and NC80) and 1.37 (MC, SC and HN) shear span-to-wall length ratio walls, respectively. Barbell-shaped wall specimens (BC40 and BC80) had a wall panel with a thickness of 80mm and the boundary columns at both ends with a cross-section of 250mm×250mm. BC's and NC's wall specimens were designed to have approximately same total area (2,250cm^2 for BC's and 2,240cm^2 for NC's), same confined end regions area (625cm^2 for BC's and 666cm^2 for NC's considering cover concrete) and with comparable flexural capacity. The rectangular walls with 1.37 shear span-to-wall length ratio were tested to study the effect of confined area and axial load on the ultimate deformation. For rectangular walls with 1.37 shear span-to-wall length ratio, SC specimen had the smallest confined area (180cm^2) with the smallest confining hoop spacing (40mm) and MC specimen had the medium confined area (300cm^2) with 80mm hoop spacing. HN specimen had the largest confined area (540cm^2) with 40mm hoop spacing. An axial load of approximately 0.10$A_g f'_c$ was applied to all specimens, except HN specimen which sustained an axial load level of 0.20$A_g f'_c$, where, A_g is the gross section area of wall, and f'_c is the concrete compressive strength. The axial load was applied to the wall specimens at the beginning of each test and maintained constant throughout the test to represent the action of vertical loads.
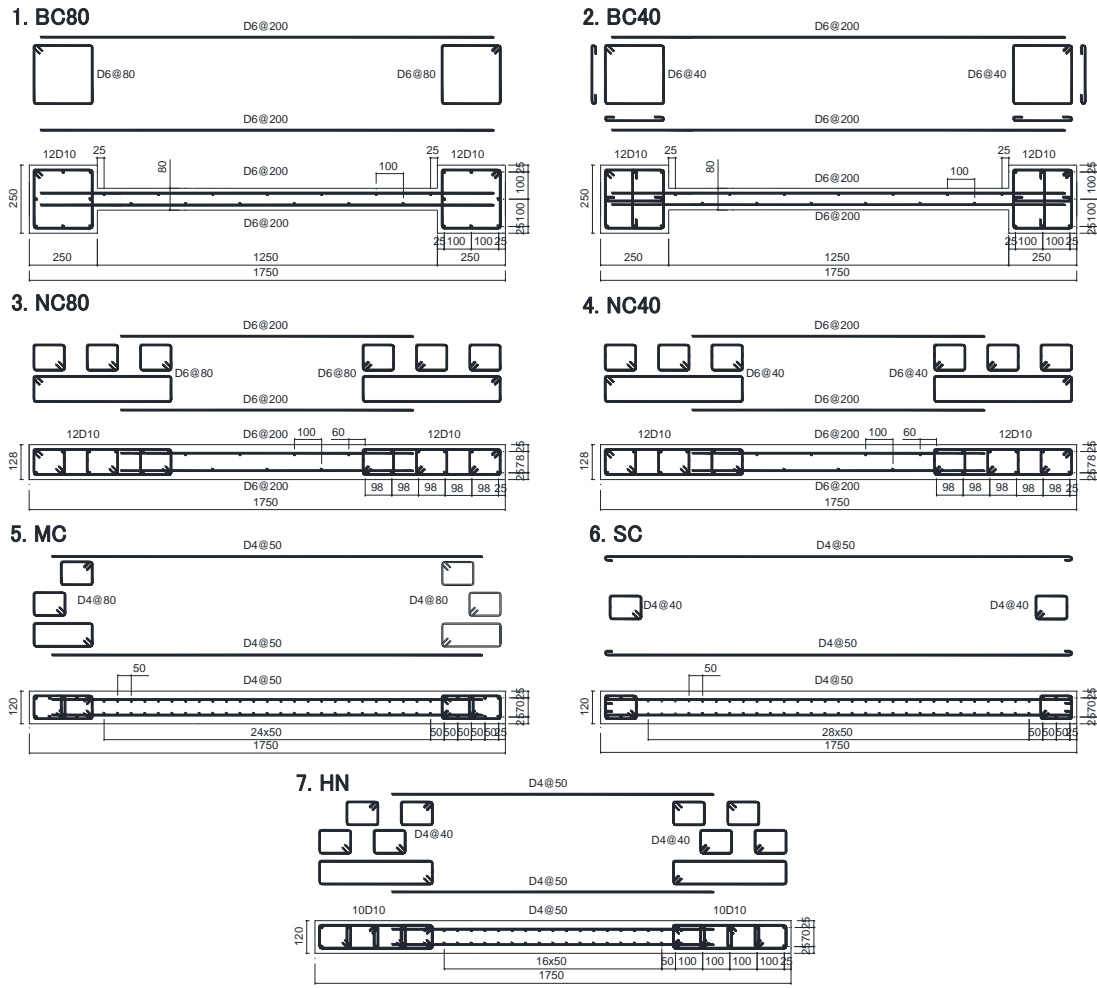
Figure 5.1 –Cross-Sections and details.

Wall specimens were classified as intermediate aspect ratio walls and designed to fail in flexure, and the shear safety factor, z, defined as the ratio of shear capacity to flexural capacity vary from 1.1 to 1.5. The flexural capacity, $_cQ_{mu}$, were calculated based on a simplified wall design equation (Eq. 5.1) given by the standard for seismic evaluation of existing reinforced concrete buildings (JBDPA 2001), and the shear capacity, $_cQ_{su}$, were calculated based on an empirical equation (Eq. 5.2) given by the Commentary of Structural Technique Standard for Buildings (NILIM 2015).

$$_cQ_{mu} = \left(a_t f_y l_w + 0.5 a_{wv} f_{wv} l_w + 0.5 N l_w\right)/a \tag{5.1}$$

With, $N \leq 0.67 f'_c A_c$ for confined boundary column

$$_cQ_{su} = \left\{\frac{0.068 p_{te}^{0.23}\left(f'_c+18\right)}{\sqrt{M/(QD)+0.12}} + 0.85\sqrt{f_{wh} p_{wh}} + 0.1\sigma_0\right\} t_e j \tag{5.2}$$

where, a_t, f_y: area and yield strength of longitudinal reinforcement in the wall boundary region, a_{wv}, f_{wv}: area and yield strength of longitudinal web reinforcement, l_w: length between the centers of boundary columns ($0.9D$ for rectangular cross-section), N: axial load, a: shear span length, p_{te}: equivalent tensile reinforcement ratio (%) ($=100a_t/t_ed$), d: effective length of wall ($=0.95D$), f'_c: concrete compressive strength, $M/(QD)$: moment-to-shear ratio ($1 \leq M/(QD) \leq 3$), f_{wh}: yield strength of horizontal web reinforcement, p_{wh}: horizontal web reinforcement ratio, σ_0: average axial stress for gross cross-sectional area, t_e: equivalent wall thickness, j: lever arm length ($=7/8d$), D: wall length.

The flexural and shear capacities as well as the shear-to-flexural capacity ratio are shown in Table 5.1.The detailing of hoops in end regions of rectangular walls satisfied the ACI 318-11 requirements.

Table 5.1 – Properties of wall specimens.

Wall	h_w/l_w (mm)	a_s (Shear span)	Confined end region			Wall panel		$N/A_gf'_c$	$_cQ_{mu}$ (kN)	$_cQ_{su}$ (kN)	SFR
			A_{ch} (mm^2)	p_{wc},%	p_l,%	t_w (mm)	$p_{wh} = p_{wv}$, %				
BC80	1.6 (2800/1750)	1.71 (3000 mm)	250×250 (216×216)	0.95	0.91	80	0.40	0.13	532	761	1.43
BC40				0.32							
NC80			128×520 (94×506)	1.24	1.29	128	0.25	0.11	586	867	1.48
NC40				2.47							
MC	0.97 (1700/1750)	1.37 (2400 mm)	120×250 (84×214)	1.36	2.56	120	0.47	0.10	499	620	1.24
SC			120×150 (84×114)	1.46	2.70			0.10	441	596	1.35
HN			120×450 (84×414)	2.61	1.38			0.20	599	671	1.12

Notes:$h_w/l_w$is the aspect ratio, a_s is the shear span-to-wall length ratio, A_{ch} is the area of confined end region (values in brackets correspond to confined region dimensions measured between stirrups centerlines), p_{wc} is the boundary longitudinal reinforcement area ratio, t_w is the wall panel thickness, p_{wh} and p_{wv} are the horizontal and vertical web reinforcement ratio, respectively, $N/(A_gf'_c)$ is the axial load ratio, A_g is the concrete gross section area, f'_c is the concrete compressive strength, and SFR is the shear to flexural capacity ratio.

5.2.2. Material properties

Table 5.2 shows compressive strength, Young's modulus and tensile strength of concrete cylinders. Young's modulus was determined by connecting the origin to the point of one third of compressive strength on the stress-strain curve. Table 5.3 shows the mechanical properties of reinforcement. Reinforcement consisted of deformed D10 bars as longitudinal bars in confined end-regions with either D6 or D4 deformed bars as transverse reinforcement. Either D6 or D4 deformed bars were used as horizontal and vertical reinforcement in the wall panels.

Table 5.2 – Measured mechanical properties of concrete.

Specimen	Compressive strength (MPa)	Young's modulus (GPa)	Splitting tensile strength (MPa)
BC80/BC40	59.5	30.9	5.10
NC80/NC40	52.5	30.1	3.66
SC	27.5	29.5	2.24
MC	29.6	33.0	2.60
HN	27.8	31.0	2.52

Table 5.3 – Measured mechanical properties of reinforcement.

Specimen	Reinforcing bar	Yield strength (MPa)	Young's modulus (GPa)	Ultimate strength (MPa)
BC's & NC's	D6	387	189	496
	D10	377	194	533
MC, SC & HN	D4	395	190	524
	D10	385	196	524

(a) BC40 (left) and BC80 (right)   (b) NC40 (left) and NC80 (right)

(c) MC   (d) MC   (e) MC
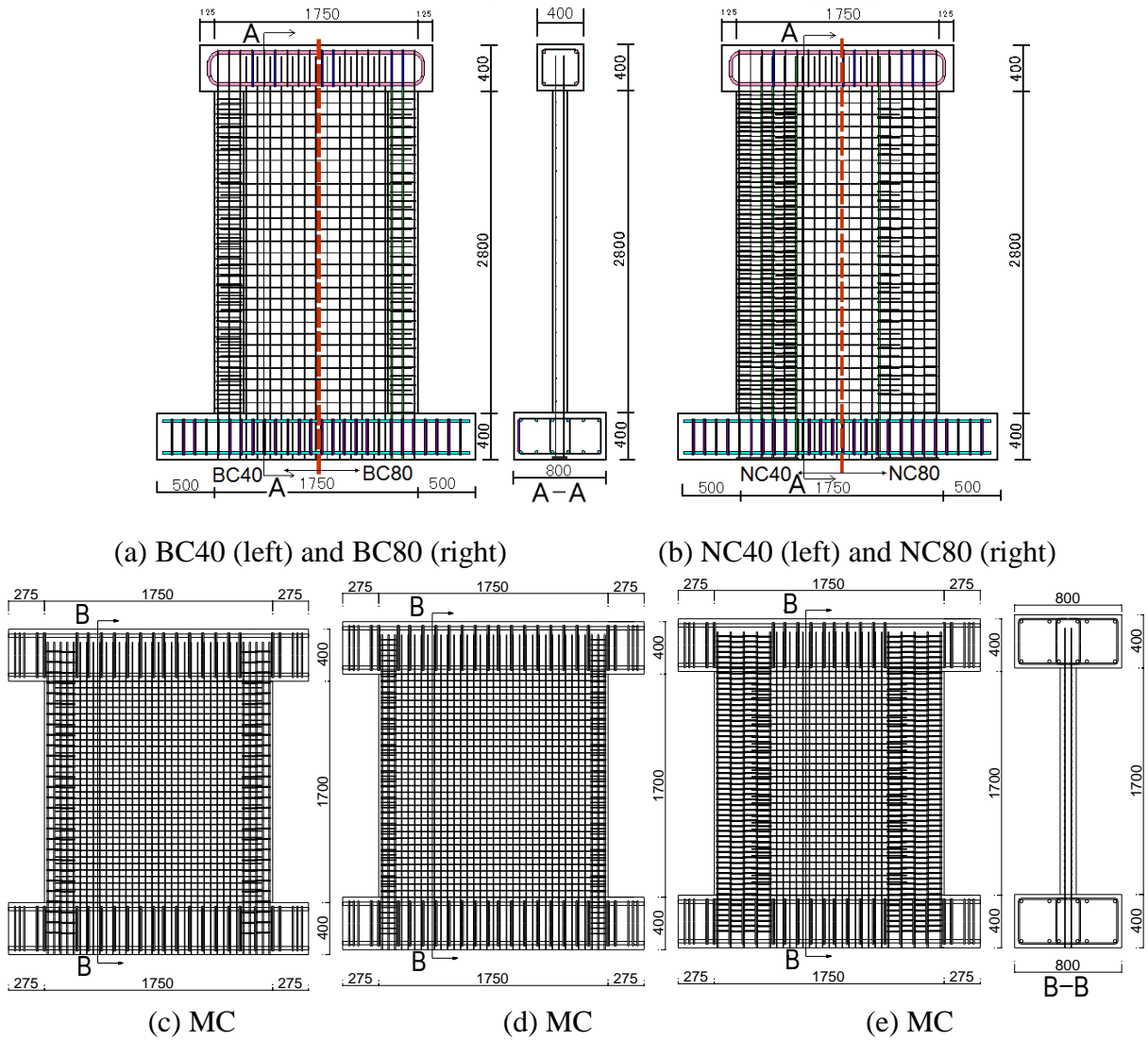
Figure 5.2 –Vertical reinforcement layout of tested specimens.

5.2.3. Specimens construction and test procedure

The specimens were cast vertically in two phases, consisting of the foundation block followed by the wall section and the loading beam with intentionally roughened surface created at the foundation–wall interface to insure good adherence. Before each test, the foundation block was anchored to the strong floor using eight prestressed steel rods. The foundation block and its anchors were designed to provide nearly a fixed-based condition for the wall tests.

As Figure 5.3 shows, the wall specimens were tested in an upright position as a vertical cantilever with a quasi-static lateral load applied at a height of 3000mm above the wall-foundation interface for specimens with shear-span ratio of 1.71, and at a height of 2400mm for specimens with shear-span ratio of 1.37. Axial load was applied using hydraulic jacks connected to the loading frame to simulate vertical loading. The contra-flexure point was kept at the center of the steel loading beam that is attached to the top RC loading beam by prestressed steel rods. The top RC loading beam insured a uniform distribution of the applied loads to the wall. Reversed cyclic lateral load was applied to the wall using a static displacement-controlled reversed cyclic load protocol. Each load increment was repeated two times at drift ratios (top horizontal displacement at the centerline of the loading beam divided by the clear height of wall specimen) of 0.05%, 0.1%, 0.25%, 0.5%, 0.75%, 1.0%, 1.5%, 2% and 4%.
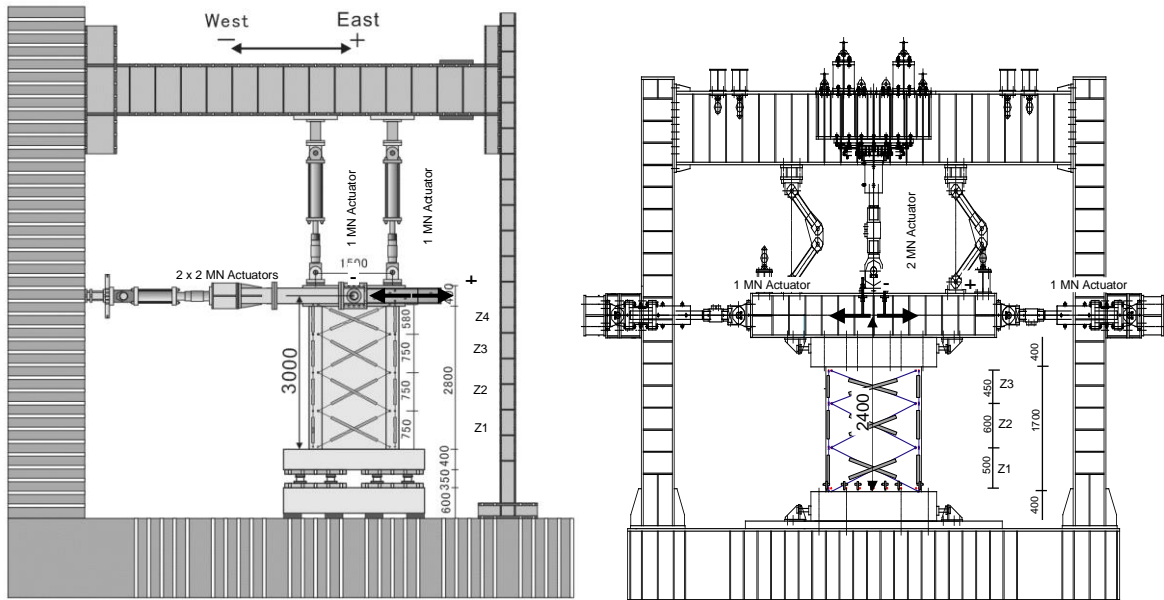
(a) BC's and NC's walls   (b) MC, SC and HN walls

Figure 5.3 –Test setup (Dimensions in mm,)

5.2.4. Test instrumentation

Load cells were used to measure the applied lateral and axial loads. Linear variable differential transformers (LVDTs) were used to measure displacements between specified locations as shown in Figure 5.4. Reinforcement strains were measured at different locations using strain gauges placed on boundary vertical reinforcement, web vertical and horizontal reinforcement, and boundary transverse reinforcement over the height of approximately half wall length from the wall-foundation interface. This LVDT configuration allowed determination of wall foundation sliding and uplift, lateral wall displacements at various height levels, including flexural, shear, and sliding shear components, and wall average concrete strains over specified gauge lengths. Walls with shear span-to-wall length ratio of 1.71 were subdivided into four zones (Z1, Z2, Z3 and Z4) in the vertical direction for a separate measurement of the contributions of shear and flexure deformations to the total deformation, and walls with shear span-to-wall length ratio of 1.37 were divided into three zones (Z1, Z2 and Z3).
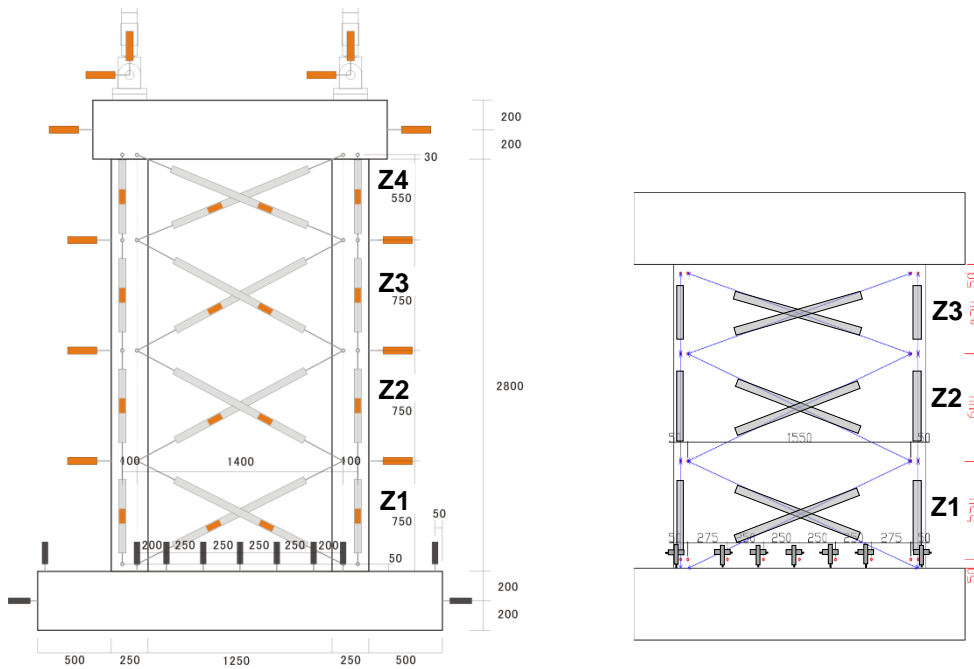
(a) BC's and NC's walls   (b) MC, SC and HN walls

Figure 5.4 – LVDTs layouts.

5.3. Test Results and Discussions

5.3.1. Damages and failure modes

Figure 5.6 shows the damage situation at 2% drift ratio of BCs and NCs walls and at 1.5% drift ratio of MC, SC and HN walls. At 0.05% drift ratio, flexural cracks started to appear in the lower part of the tensile region. The number of flexural cracks increased along the confined regions height and progressed into flexural-shear cracks at drift ratio of 0.5% with the yielding of tensile longitudinal reinforcement.

(a) 1.71 shear span-to-wall length ratio

(b) 1.37 shear span-to-wall length ratio

Figure 5.5 – Crack patterns
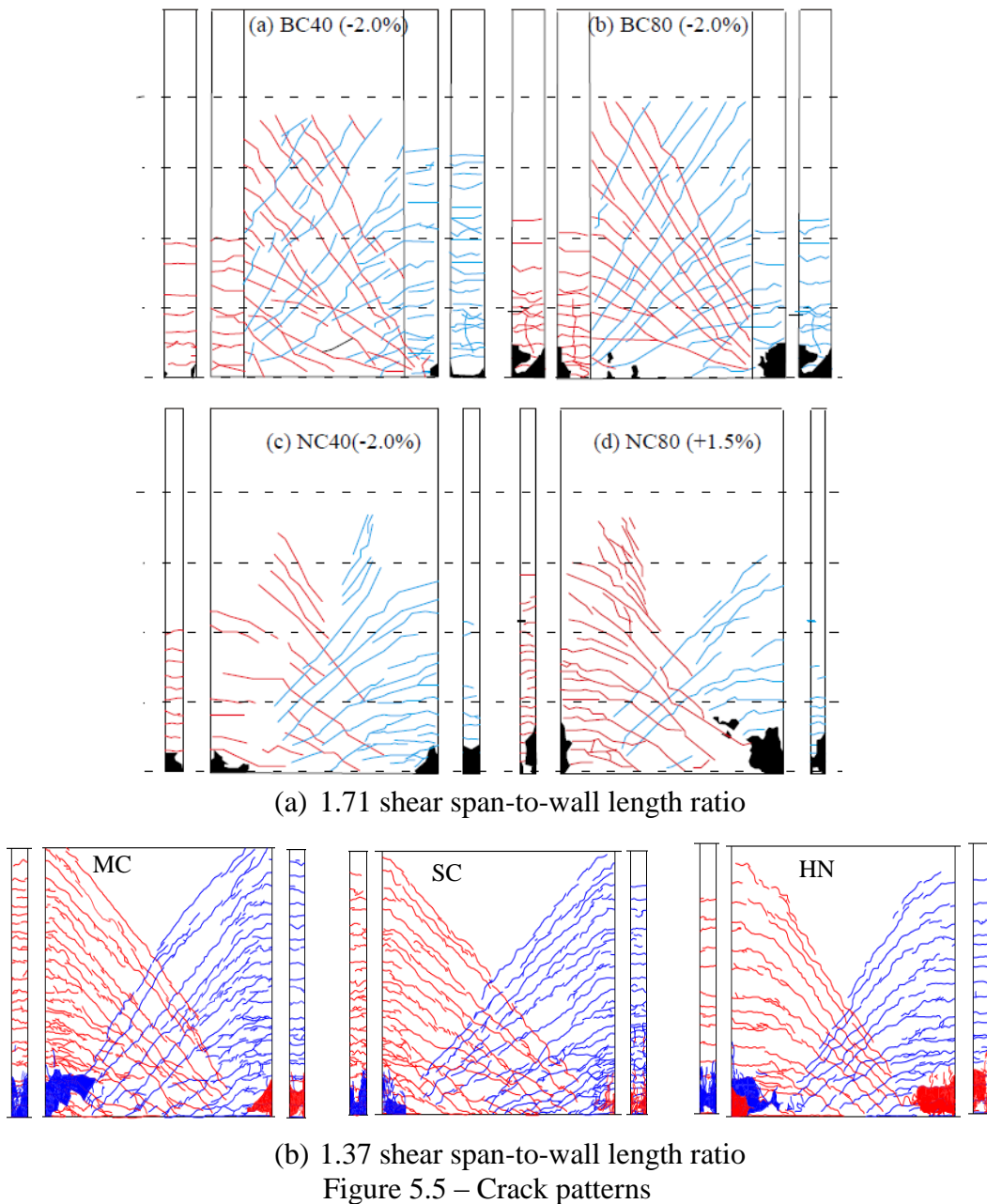
For specimens with boundary columns, flexural cracks and shear cracks were not necessarily continuous at the column-wall panel interface. As drift ratio increased, these cracks increased and propagated to the upper part and to the center of the walls. Spacing between flexural cracks was larger for HN specimen under high axial load level compared to other specimens. Although the wall specimens behaved generally in a flexural manner by yielding of the longitudinal reinforcement and suppressing of a premature shear failure, these specimens failed finally by concrete crushing of the compression zone with buckling of longitudinal reinforcement in confined end regions after the drift ratio of 1.5%. Global buckling of damaged regions under compression was more pronounced for HN specimen at final loading stage. The failure was brittle at final stage since the core concrete crushed in a brittle manner. Crushing was more brittle and happened mainly around the boundary column for BC40 and BC80, while extended to the wall center for rectangular section walls.

(c) 1.71 shear span-to-wall length ratio walls around peak point
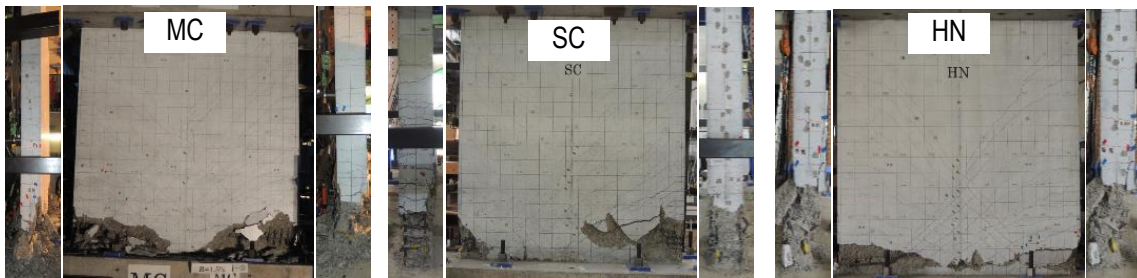
(d) 1.37 shear span-to-wall length ratio walls at 1.5% drift ratio

Figure 5.6 – Damage patterns.

As expected, the performance of wall with boundary columns was better than that of rectangular walls with similar shear span-to-wall length ratio and transverse reinforcement spacing in terms of drift capacity and damage level. Boundary columns showed the ability to reduce damage level in wall panel since they carry a large amount of axial force, which reduces axial stress level in wall panels. Comparison between BC80 and NC40 walls have comparable degree of damage and almost similar ultimate drift showing that for similar confined area, rectangular walls need to be tightly confined to reach similar performance of walls with boundary columns.

In this manner, boundary columns can also contribute effectively in preventing failure mode due to global wall buckling when subjected to high axial load level. Damage observation for specimens with larger hoop spacing revealed that the two outer

82

longitudinal reinforcing bars buckled first followed by simultaneous buckling of the other longitudinal reinforcement at final stage.

The damaged regions in confined region under compression for all specimens seem to have concentrated within approximately 30cm height above the wall base, whereas extended horizontally toward wall center. MC and SC walls have comparable volumetric transverse reinforcement content in confined end regions (1.36% for SC and 1.46% for MC). However, SC wall with shallow confined core and closer hoop spacing might have similar to better performance than larger confined core with larger hoop spacing since core concrete crushing under compression spread less in SC specimen compared MC specimen for a comparable ultimate drift. Spacing of transverse reinforcement might be a key parameter when assessing detailing requirements to reach a large drift capacity since failure might be accelerated by longitudinal reinforcement buckling.

5.3.2. Lateral load - drift angle hysteretic behavior

Figure 5.7 shows lateral load-drift ratio relations. All specimens yielded in flexure, reached the peak point, and deformed until the failure without too much degradation of lateral load carrying capacity and showed ductile inelastic behavior after flexural yielding. The ultimate point was defined by either 20%-drop of the peak load or the maximum drift reached during the loading process. Table 5.4 summarizes test results for lateral load and corresponding drift ratio at concrete cracking, yielding of longitudinal reinforcement in confined regions, peak point as well as ultimate deformation point for both positive and negative loading directions. Hysteresis curves of the shear-span ratio 1.71 walls showed pinching loops due to high axial load, high concrete strength and low longitudinal reinforcement content in confined end regions.

Table 5.4 – Experimental characteristic damage points.

Specimen		Flexural Cracking		Yielding		Peak		Ultimate
		Q_{cr}	R_{cr}	Q_y	R_y	Q_{max}	R_{Qmax}	R_u
		(kN)	(%)	(kN)	(%)	(kN)	(%)	(%)
BC40	Positive	443	0.12	562	0.29	634	1.41	4.00
	Negative	-441	-0.10	-521	-0.25	-608	-1.47	-2.75
BC80	Positive	418	0.08	487	0.26	633	1.17	2.00
	Negative	-338	-0.07	-507	-0.33	-592	-1.45	-2.00
NC40	Positive	328	0.07	478	0.19	606	1.91	2.38
	Negative	-379	-0.09	-449	-0.20	-604	-1.46	-2.00
NC80	Positive	334	0.09	467	0.30	598	1.16	1.50
	Negative	-331	-0.08	-332	-0.12	-578	-0.87	-1.50
MC	Positive	284	0.11	444	0.30	490	0.73	1.53
	Negative	-247	-0.07	-445	-0.37	-467	-0.72	-1.48
SC	Positive	126	0.05	420	0.46	461	1.40	1.81
	Negative	-178	-0.05	-288	-0.19	-434	-1.38	-1.50
HN	Positive	407	0.10	586	0.36	611	0.69	1.50
	Negative	-398	-0.10	-477	-0.23	-579	0.64	-1.51
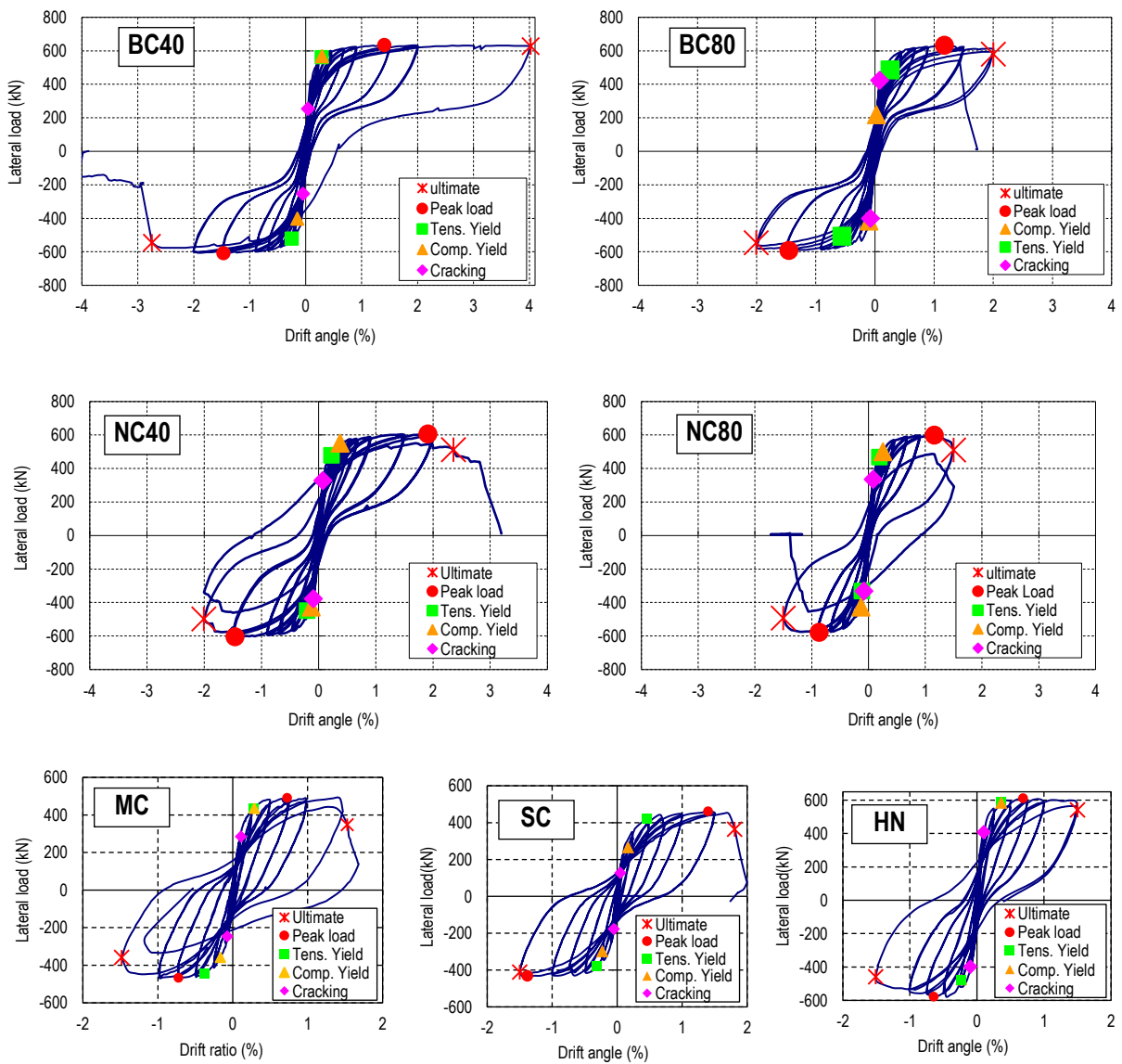
Figure 5.7 – Lateral load-drift ratio hysteresis curves.

5.3.3. Variation of displacement components

Although the shear force in a cantilever wall subjected to a horizontal top load is constant over the height of the wall, the shear deformation is not uniform after concrete cracking and reinforcement yielding. Wall specimens were divided into either four (Z1, Z2, Z3 and Z4) or three (Z1, Z2 and Z3) along the wall height for a separate measurement of the contributions of shear and flexure deformation components to the total deformation. The vertical displacement transducers were used to measure flexural deformation Δ_f, and can be calculated as:

$$\Delta_f = \theta h = \frac{(V_L - V_R)}{2L} h \tag{5.3}$$

where θ is the rotation over the height h, V_L and V_R are the vertical displacements along the wall edge (measurements of the two vertical displacement transducers), and L is the horizontal distance between gauges, as shown in Figure 5.8. The diagonal displacement transducers were used to measure shear displacement Δ_s, which was estimated from changes in their length as:

$$\Delta_s = \frac{(d_1' - d)d - (d_2' - d)d}{2L} \tag{5.4}$$

where d_1' and d_2' are the deformed length of diagonal, d is the original diagonal length, and L is the horizontal distance between gauges. Mohamed *et al.* (2014) suggested that the shear deformation given by Eq. (5.4) should be corrected because it contains flexural deformation due to the existence of a moment gradient along the height of the shear walls that should be excluded. The shear deformation can be expressed as follows:

$$\Delta_{s\_cor} = \Delta_s - (\alpha - 0.5)\theta h \tag{5.5}$$

Hiraishi (1984) suggested that the factor α is estimated based on the rotation θ, as it is the ratio of the shaded area to the rectangular surrounded by solid lines shown in Figure 5.9(b), giving same results for α when calculated as the ratio of curvature centroid to panel height as shown in Figure 5.8. Massone and Wallace (2004) set α to 0.67, assuming a triangle curvature distribution. Based on this assumption, the drift components of the tested wall specimens at the first cycle of each drift level are illustrated in Figure 5.9.
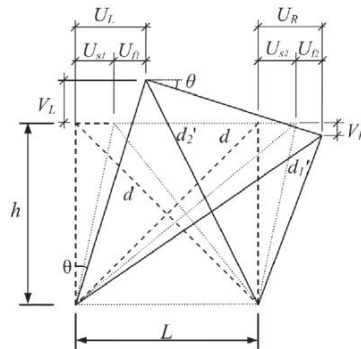
Figure 5.8 – Flexural and shear deformation components
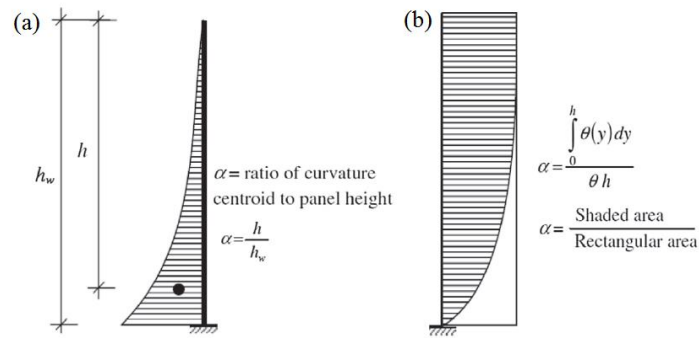
Figure 5.9 – Method for estimating *α* based on (a) curvature profile; (b) rotation profile over the wall height (Mohamed *et al.*, 2014)

(a) BC40

(b) BC80

(c) NC40

(d) NC80

- ■ Shear (Z4)
- □ Shear (Z3)
- ■ Shear (Z2)
- ■ Shear (Z1)
- □ Slide (Z0)
- ■ Flexure (Z4)
- □ Flexure (Z3)
- □ Flexure (Z2)
- ■ Flexure (Z1)
- □ Pull (Z0)

(e) MC

(f) SC

(g) HN
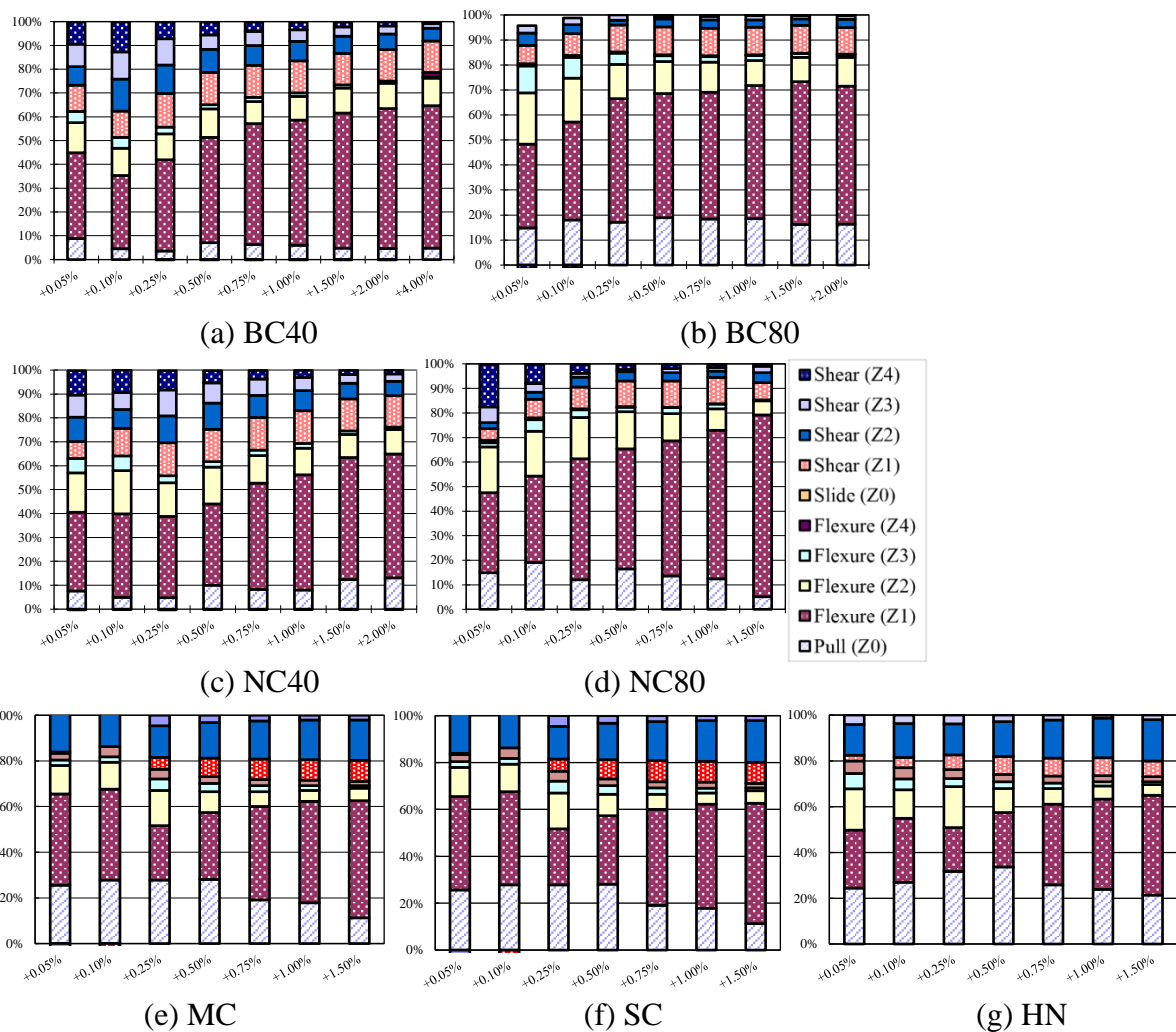
Figure 5.10 –Variation of flexural and shear deformations with top drift ratio.

Figure 5.10 shows the contribution of flexure and shear deformations as percentage of the total lateral drift for four segments of the 1.71 shear-span ratio walls and three segments of the 1.37 shear span-to-wall length ratio walls. Zone Z0 is the lower 50mm region, which has vertical and horizontal displacement gages to measure pullout of vertical

reinforcement and sliding along the joint between the wall base and foundation, respectively.

The flexural contribution was clearly dominant and constantly as high as 70% for the 1.71 shear span-to-wall length ratio rectangular walls, while it slightly decreased from approximately 70% to 60% after yielding for 1.37 shear span-to-wall length ratio rectangular walls. Furthermore, more than 70% of the flexural deformation after yielding is concentrated at lower zone (Z1). Similarly, the shear contribution concentrated in the lower part, where the longitudinal reinforcement yielded remained approximately constant for all peak drift ratio in the inelastic range for the 1.71 shear-span ratio walls, while it gradually increased for the lower shear-span ratio walls.

For boundary column walls, it is noted that contribution of shear deformation was large before yielding since the flexural deformation changed from about 40-50 % before yielding to approximately 70% for larger drift ratios. On the other hand, sliding at the wall-foundation interface was negligible in all specimens, whereas contribution of deformation due to pullout of longitudinal reinforcement was more significant for rectangular walls especially for smaller shear-span ratio walls. The contribution of deformation due to pullout of longitudinal reinforcement was about 18% for larger shear span-to-wall length ratio walls and about 25% for other rectangular walls while it was lower than 10% for walls with boundary columns. It was also observed that contribution of deformation due to pullout of longitudinal reinforcement is larger for rectangular walls compared barbell walls.

5.3.4. Strain distribution in confined regions

Confined regions of MC, SC and HN walls were instrumented by strain gages attached to longitudinal and transverse reinforcement over a height of about half of the clear wall height from the foundation-wall interface. Strain gages on transverse reinforcement were attached at 80mm from the wall base and then at every 160mm above. Only transverse reinforcement at 80mm and at 240mm height tensile yielded in end regions under compression. Figure 5.11 and Figure 5.12 shows strain distribution in transverse reinforcement perpendicular and parallel to the wall thickness at 80mm above the wall base, respectively. X-axis represents distance from the wall centerline. Strain evolution in confined regions showed that yielding initiated earlier for HN wall under high axial load compared to MC and SC walls. The high-compressive region tends to expand more in the horizontal direction than in the vertical direction. The high-compressive region was defined as the region where transverse reinforcement parallel to wall thickness yielded in confined boundary under compression. Due to the influence of the high axial force in HN specimen, the high stress area spread both in the horizontal and in the vertical direction. Figure 5.13 shows strain distribution in the outermost edge longitudinal reinforcement. It is shown that yielding of longitudinal reinforcement at the wall bases was very limited

with a maximum tensile strain less that 0.5%. It is also shown that the damaged region was limited in a height of about 300mm. Based on strains in transverse and longitudinal reinforcement, Figure 5.14 represents schematic damaged regions in SC, MC and HN walls that represent plastic hinge region. This range for plastic hinge length is in good agreement with the proposal of Takahashi *et al.* (2013) suggesting that the plastic hinge zone length would be 2.5 times the wall thickness, and that the height of confinement may be limited to 3 times that of the wall thickness if the expected compressive strain is not exceeding 0.008. These observations demonstrate that the tested walls were compression-controlled.

| (a) MC | (b) SC | (c) HN |
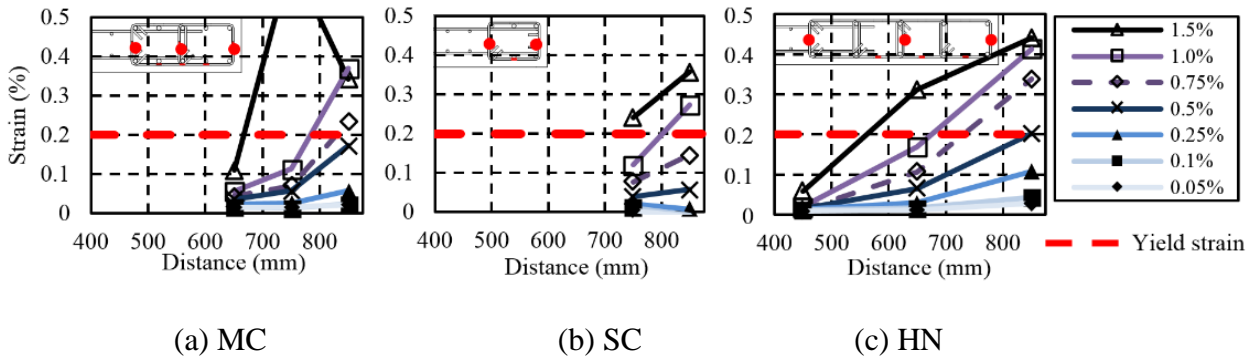
Figure 5.11 –Strain distribution in transverse reinforcement parallel to wall thickness.

| (a) MC | (c) HN |
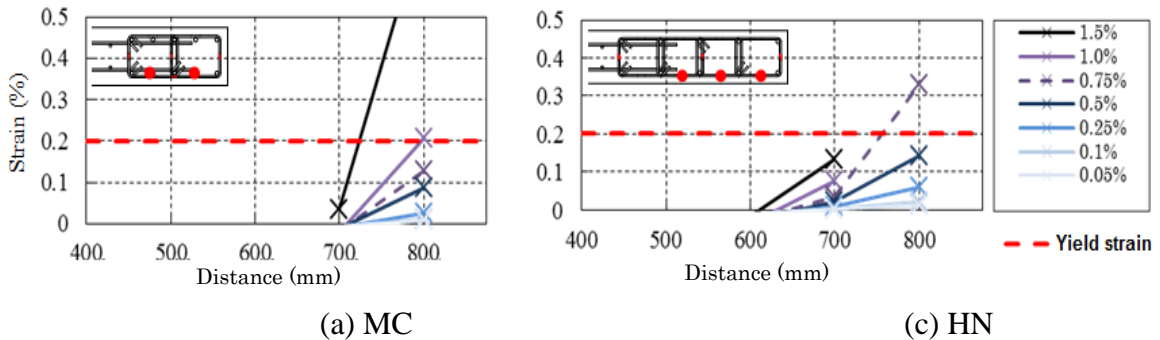
Figure 5.12 – Strain distribution in transverse reinforcement perpendicular to wall thickness.

(a) MC   (b) SC

(c) HN
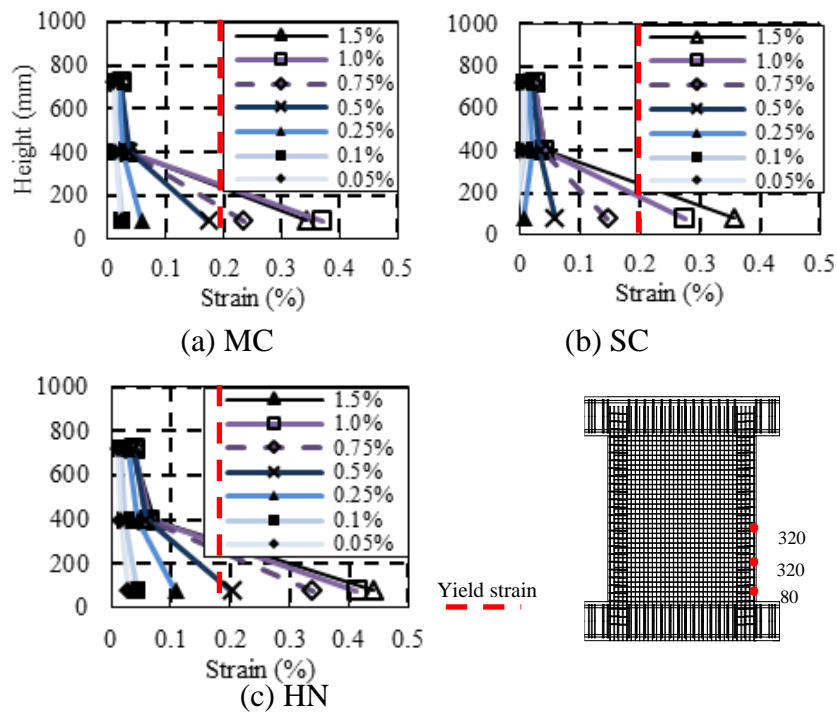
Figure 5.13 – Strain distribution in the outermost edge longitudinal reinforcement.
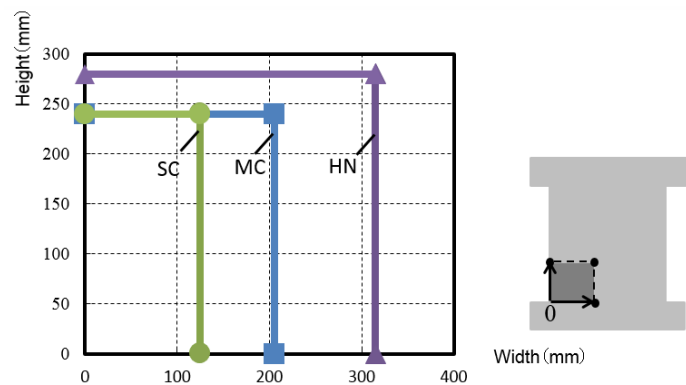
Figure 5.14 – Schematic damaged regions in SC, MC and HN walls

5.3.5. Vertical displacement distribution at wall base

Displacement transducer were mounted at seven locations along the wall base to measure vertical and horizontal displacement at a height of 50mm from the wall-foundation interface. Figure 5.15 shows displacement transducer layout at the wall base and vertical displacement distribution along the wall base for MC, SC and HN walls corresponding to the peak of the first loading cycle. Vertical reference line represents the wall vertical centerline and the two vertical dashed lines represent limit between confined boundary regions and wall panel. It is shown that for up to drift angle of 0.5%, distribution of vertical displacement at the base is linear. For larger drift angles, this distribution is linear between the wall centerlines and compression edge, while it is not linear in the opposite

side of the centerline due to the influence of confined end region. Vertical displacement in HN wall is reduced compared to MC and SC walls due to the influence of high axial load. The distribution of vertical displacement at the wall bases demonstrates that the assumption of plane sections remain plane is not always true especially under large drift angles.
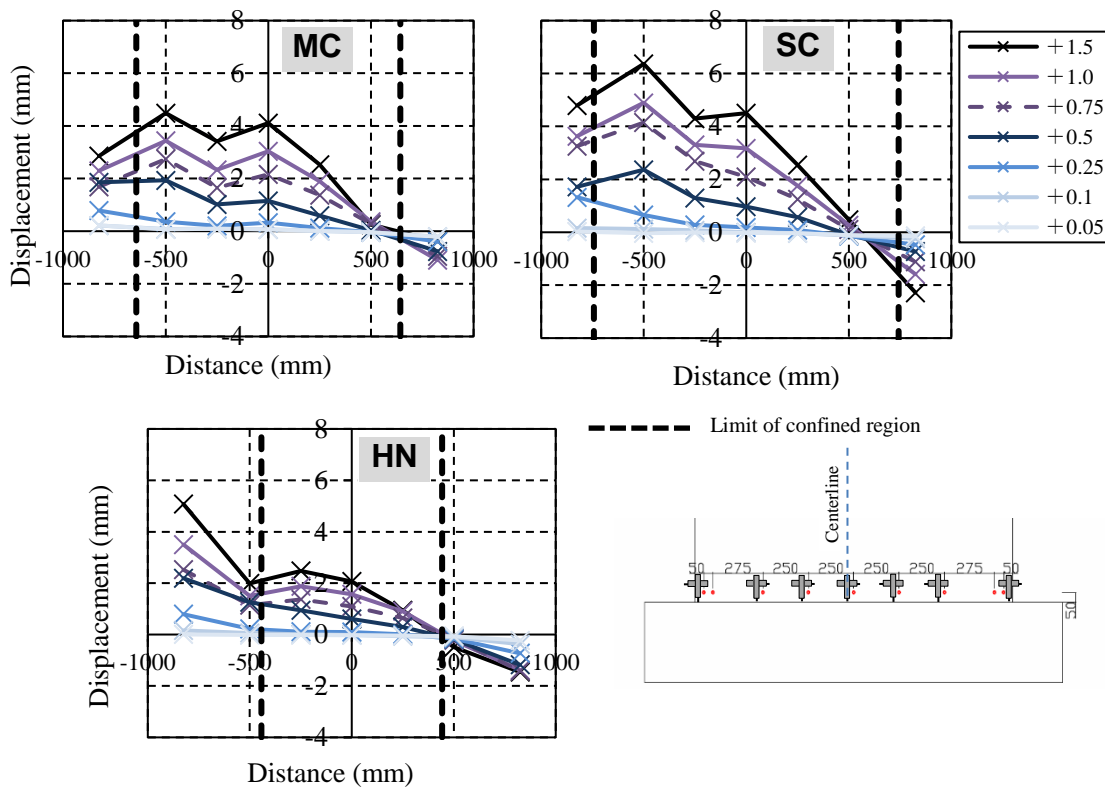
Figure 5.15 – Vertical displacement distribution at the base

5.3.6. Equivalent damping ratios

Estimation of the equivalent viscous damping factor is an important step in the methodology of performance-based design. The use of effective stiffness and equivalent viscous damping leads to simplify the dynamic analysis and making this approach very desirable for design purposes. However, errors in the estimation of equivalent viscous damping leads to consequent errors in the estimation of the ductility demand of the designed elements. Equivalent viscous damping value was evaluated based on the conventional Jacobsen's approach, which estimates equivalent viscous damping based on the ratio of the dissipated energy per cycle to the strain energy stored at maximum displacement at that cycle. Figure 5.16 shows equivalent damping ratios as function of drift angles for the tested wall specimens evaluated for second cycle of each peak drift angle. Equivalent damping is scattered from 0.5% to 3% and tends to increase with the increase of drift angle. It is observed that damping of walls with lower shear span-to-wall

length ratio is higher that walls with higher shear span-to-wall length ratio, and that damping of walls with boundary columns (BC's walls) is slightly lower than corresponding rectangular walls (NC's walls). SC wall with the lowest confined region area had the highest damping ratio, which was around 3%.
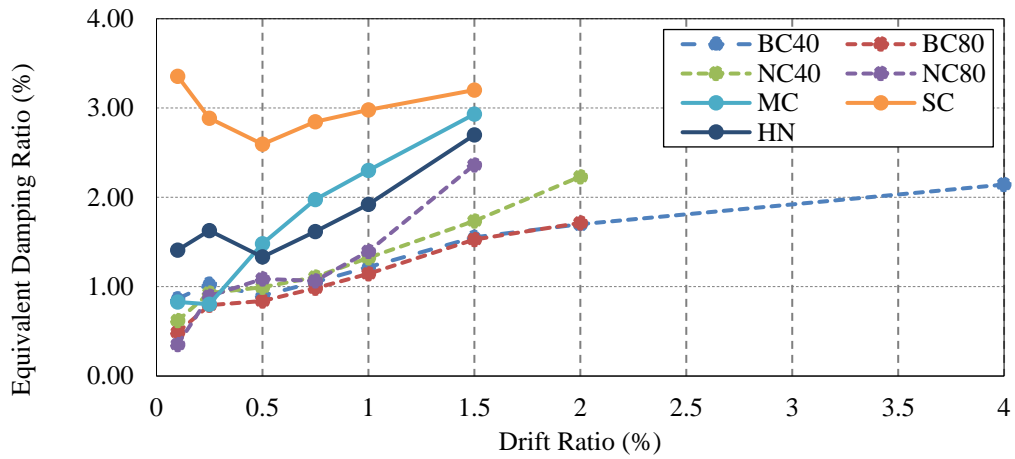
Figure 5.16 – Vertical displacement distribution at the base

5.4. Prediction of Cyclic Load-Strain Relations

5.4.1. Concept of the model

A fiber-based sectional analysis based on the plastic hinge length and moment-curvature analysis is proposed to simulate lateral load-displacement hysteresis for flexure, shear and strain hardening. The total top displacement of a RC wall is obtained by the sum of three displacement components: the flexural displacement Δ_f of the wall panel, the displacement due to strain penetration Δ_{sp} in the form of fixed-end rotation of the wall base, and the shear displacement Δ_s of the wall (Figure 5.17). The sliding displacement along the wall-foundation interface is not modeled in this study.

$$\Delta = \Delta_f + \Delta_s + \Delta_{sp} \tag{5.6}$$

Simulation of the out-of-plane wall boundary buckling is not considered in this study. It is rather recommended that failure due to out-of-plane buckling be prevented by setting minimum wall thickness based on the maximum expected tension strain of longitudinal reinforcement in confined boundaries (Parra and Moehle 2014) or the use of adequate confined boundary columns.

For the displacement-based seismic design and assessment of reinforced concrete elements, Priestley *et al.* (2007) recommended that the flexural displacement capacity be estimated using the plastic hinge concept in which the maximum displacement at the top can be computed as the sum of the elastic and the plastic components.

$$\Delta_f = \Delta_{fe} + \Delta_{fp}$$

The total flexural drift angle, R_f, is computed using the following equations.

$$R_f = R_{fe} + R_{fp} = \frac{\Delta_{fe} + \Delta_{fp}}{H_w} \tag{5.7}$$

with,

$$\Delta_{fe} = \frac{QH_w^3}{3EI} \tag{5.8}$$

$$\Delta_{fp} = L_p \phi_p \left(H_w - 0.5L_p \right) \tag{5.9}$$

$$\Delta_{sp} = \phi \, L_{sp} H_w \tag{5.10}$$

with,

$$L_{sp} = 0.022 f_y d_b \tag{5.11}$$

where H_w is the shear span, ϕ is the curvature of the wall section, ϕ_p is the plastic curvature, L_p is the plastic hinge length, L_{sp} is the strain penetration length, f_y yield strength of longitudinal reinforcement, d_b diameter of longitudinal bar.

The plastic curvature is assumed constant over the equivalent plastic hinge length. Once the plastic hinge length is determined, the flexural drift can be obtained by integrating both elastic and plastic curvature distribution based on moment-curvature relation from a section analysis. The equivalent plastic hinge length has been studied experimentally and analytically (Dazio *et al* 2009, Bohl and Adebar 2011, Kazaz 2013, Takahashi *et al.*, 2013), and equations have been proposed, the procedure is still controversial.

Takahashi *et al.*'s proposal for plastic hinge length that is linked to wall thickness and $L_p = 3t$ was used to simulate the plastic component of flexural drift although it may not be necessarily linked to the physical plastic hinge length.

The shear displacement of walls is estimated using the semi-empirical equation developed by Beyer et *al.* (2011). This equation was developed based on a series of experimental and analytical studies of slender reinforced concrete walls under seismic loading.

$$\Delta_s = 1.5 \Delta_f \left(\frac{\varepsilon_m}{\phi \tan \beta} \right) \frac{1}{H_w} \tag{5.12}$$

where ε_m and ϕ are the axial strain at the center of the wall section and the curvature of the wall section, respectively, and are derived from moment-curvature analysis, β is the crack angle. Beyer *et al.* (2011) suggested that this angle could be assumed 45 degrees for simplification. Alternatively, β can be obtained by Eq. (5.13).

$$\tan \beta = \frac{j_d}{V} \left(f_l t_w + \frac{A_{sw} f_{yw}}{s} \right) \quad (\beta \le 90°) \tag{5.13}$$

where j_d is the lever arm between compression and tensile resultants, V is the shear force, f_l is the tensile strength orthogonal to the crack, t_w is the wall thickness, A_{sw}, f_{yw} and s are the area, yield strength and spacing of shear reinforcement, respectively.
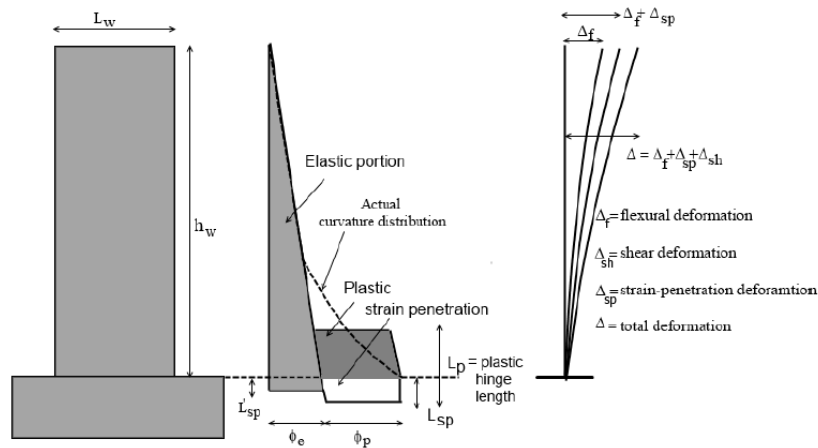
Figure 5.17 – Curvature and displacement distribution in wall height

5.4.2. Material hysteretic models

The monotonic envelope curve of the hysteretic model for concrete in compression follows the monotonic stress-strain relation of modified Kent and Park model (Scott *et al.* 1982). The hysteretic behavior of concrete in both compression and tension were modeled using hysteretic unloading and reloading rules proposed by Yassin (1994) as a set of linear stress-strain relations. The numerical model used for reinforcing steel was based on Menegotto-Pinto model (Menegotto and Pinto 1973) as extended by Filippou *et al.* (1983) to include isotropic strain hardening effects. To include the effect of buckling of reinforcement, Dhakal and Maekawa (Dhakal and Maekawa 2002) model was implemented. Buckling length of reinforcement was evaluated based on Kato *et al.* (1995).

5.4.3. Simulation results and discussion

5.4.3.1. Flexural and shear drift components

Figure 5.18 and Figure 5.19 show the lateral load-drift relations of experimental and analytical results. For each tested wall specimen, flexural, shear and total drifts are presented. The Total drift is obtained by summation of flexural, shear and strain penetration drift components. Simulated lateral load-flexural drift relations agreed very well with experimental ones until the ultimate point, although analytical results tend to slightly underestimate the load carrying capacity for rectangular walls. In addition, simulated flexural curves captured very well loading and unloading branches as well as residual drifts. Experimental and simulated shear curves agreed well and demonstrate the effectiveness of the empirical equation used to evaluate shear deformation component. Influence of buckling model for longitudinal reinforcement was marginal in the case of the tested walls.

(a) BC40

(b) BC80

(c) NC40

(d) NC80
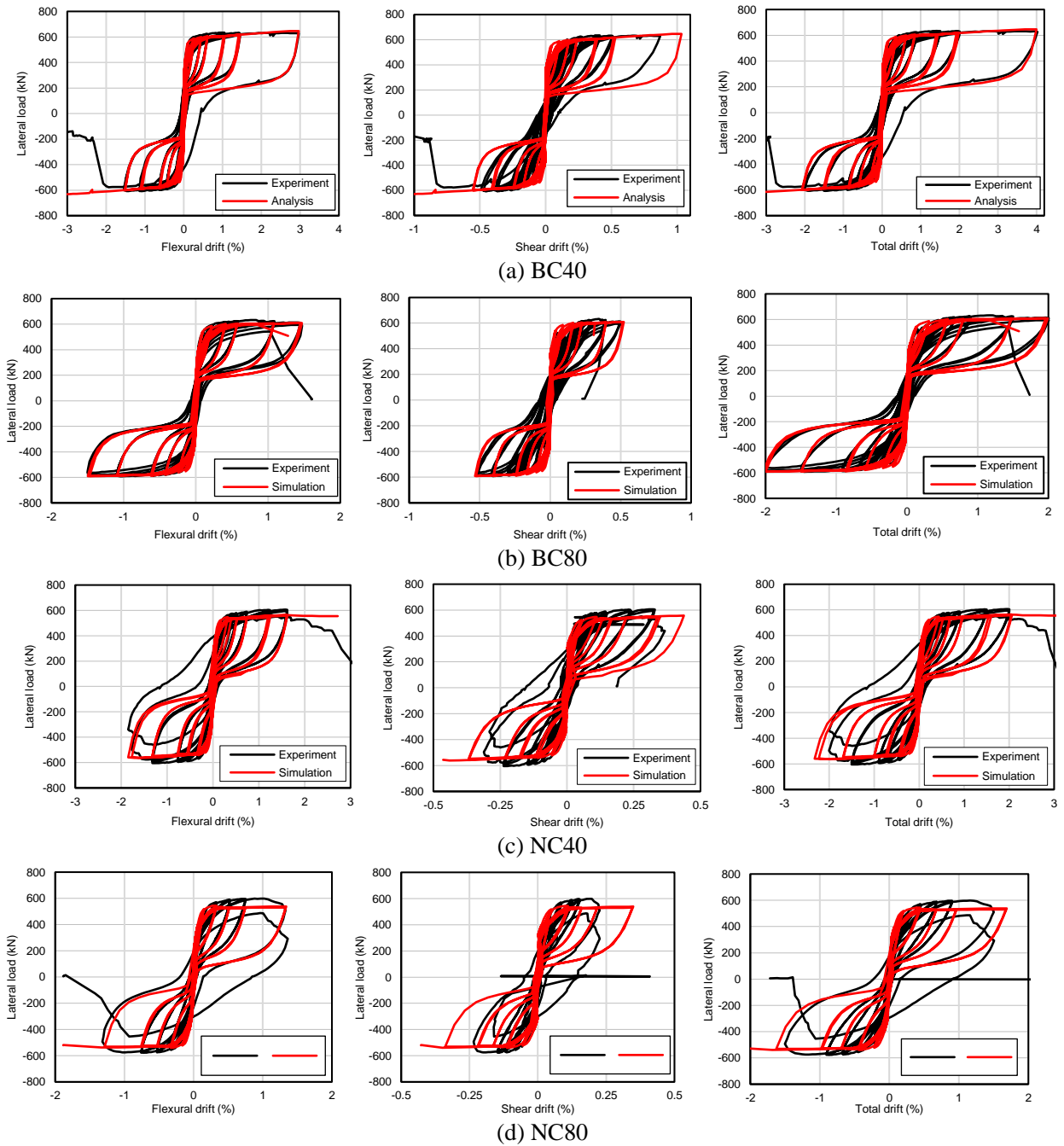
Figure 5.18 – Experimental and simulated lateral force - flexural, shear and total drift relations for BC's and NC's specimens

(a) MC

(b) SC

(c) HN
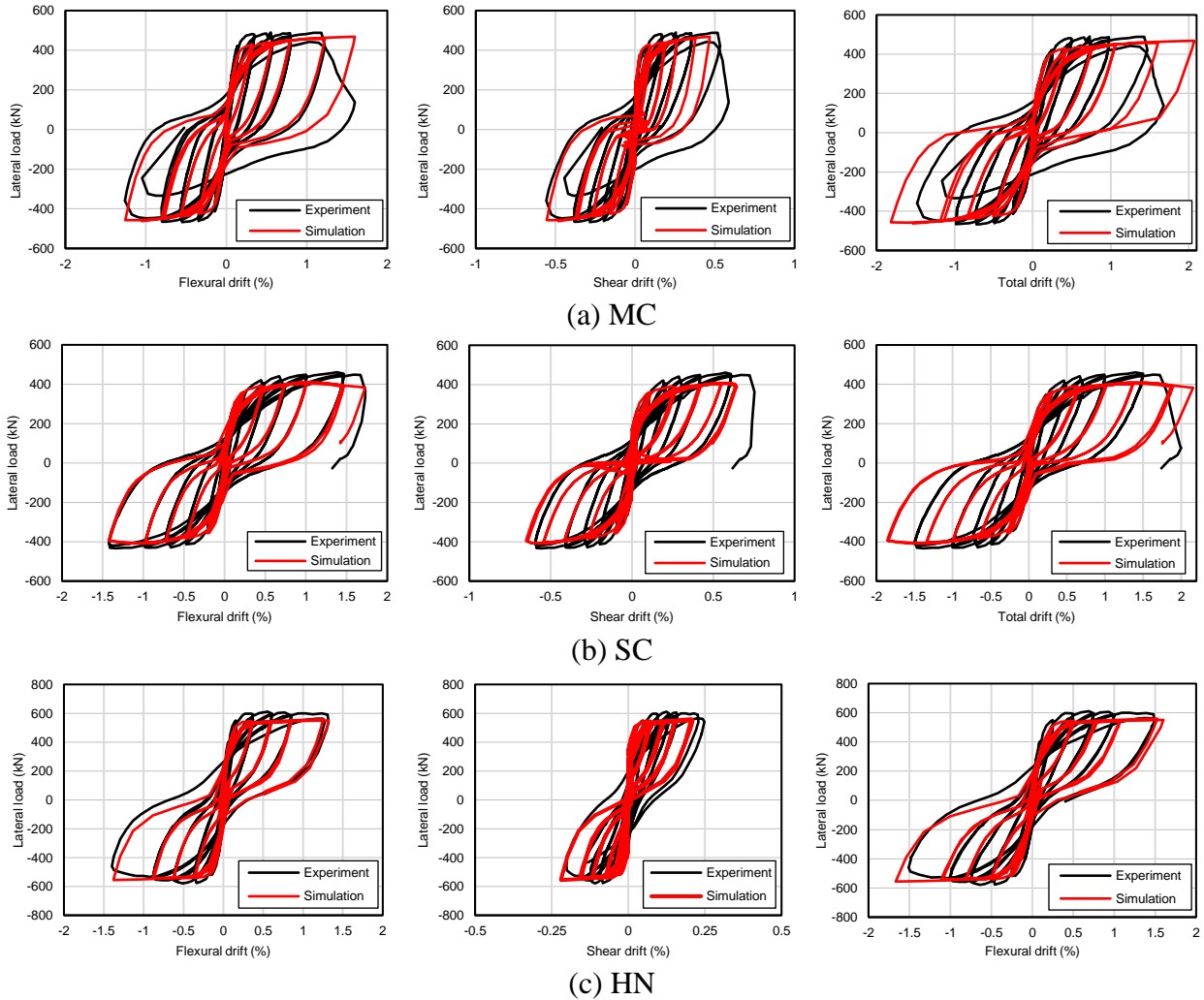
Figure 5.19 – Experimental and simulated lateral force - flexural, shear and total drift relations for MC, SC and HN specimens

5.4.3.2. Drift component due to strain penetration

Figure 5.20 shows comparison of experimental Z0 (pull) drift component with simulated drift component due to strain penetration. Experimental Z0 (pull) drift component is considered to represent strain penetration drift component. Comparison shows a reasonably good agreement between experiment and simulation especially for rectangular wall, while, an overestimation of the strain penetration component is observed in barbell shape walls under large drift angles.
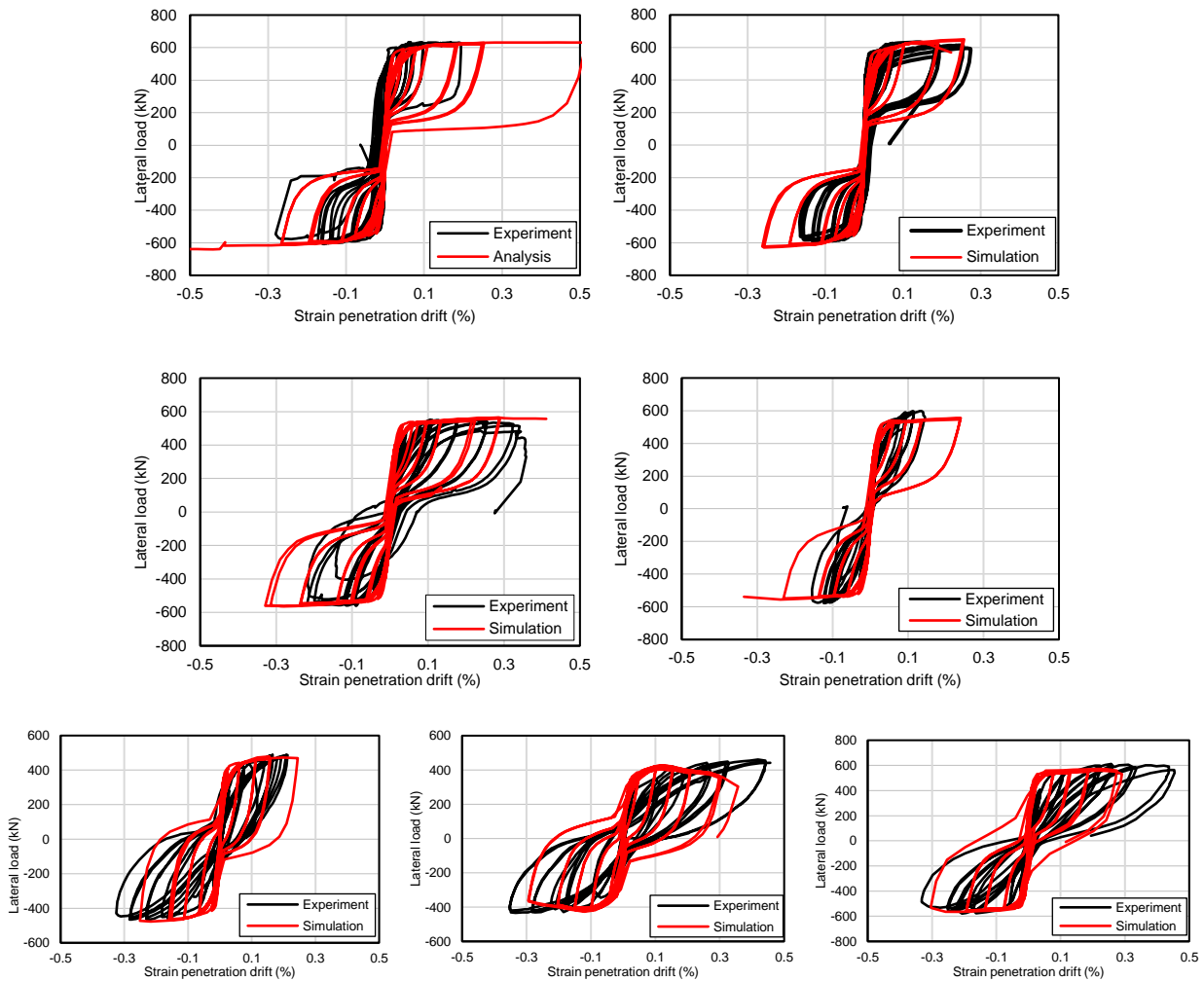
Figure 5.20 – Comparison of experimental and simulated strain penetration drift
component

5.4.4. Experimental vs. fiber-based strain distribution at wall bases

Design recommendations for longitudinal reinforcement layouts of reinforced concrete (RC) walls have been derived from plane section analyses. Such an analysis generally favors wall layouts with boundary elements containing large amounts of vertical reinforcement, providing higher moment resistance and larger ductility capacity than the same reinforcement distributed evenly along the wall length. Figure 5.21 shows comparison of experimental strain distribution at wall base with strain distribution derived from fiber-based sectional analysis for MC, SC, and HN wall specimens. Although it was shown experimentally that, the assumption of plane sections remain plane after deformation is not respected, especially for large drift and for tension strains, comparison shows that this assumption is reasonably acceptable.
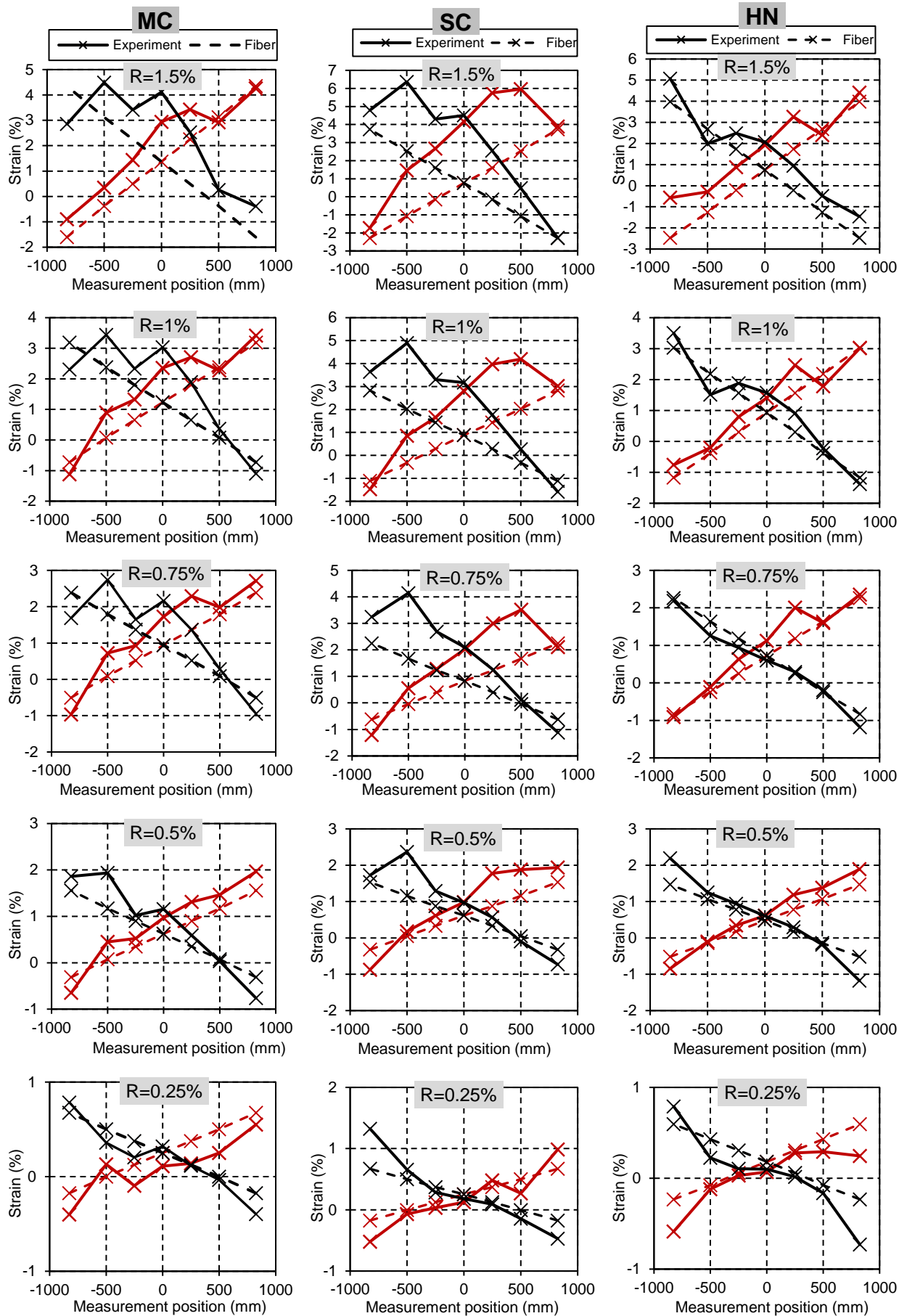
Figure 5.21 – Experimental vs. fiber-based strain distribution at wall base

5.4.5. Experimental vs. fiber-based strain distribution at wall bases

Various forms of imperfections of structures or structural members exist and are of different types: Geometrical imperfections due to fabrication imperfections, variance of dimensions or lack of verticality, straightness or flatness of a member, Material imperfections due to residual stresses or variance of material properties, and Structural imperfections due to variance of boundary conditions, loads eccentricities. The load-carrying capacity of certain classes of structures (e.g. steel members, slender RC columns, thin shell), may be significantly affected by the presence of physical imperfections.

Imperfections in structural analysis are usually introduced as equivalent geometrical imperfections or using buckling factors. Member geometrical imperfections are given in design codes (e.g. EC3) as values e_{0d}/L, which may be replaced by corresponding transverse uniform loadings giving the same bending moments. In global analysis of a structural system, usually these member imperfections are ignored and covered by reduction factors in member design, unless the frame is sensitive to 2nd order effects as for high slender members. Analytically, buckling is considered as an Euler elastic buckling or inelastic buckling, depending on slenderness.

As an initial condition, shrinkage may reduce the cracking resistance, stiffness as well as load carrying capacity of the members. Simulation of shrinkage is usually addressed as an initial strain.

Initial imperfections in the testing of prism element specimens may lead to additional moment and ultimately to local instabilities. A certain numbers of countermeasures were being taken to reduce the effects of initial geometrical imperfections. Mortar was cast on the top of the test specimens for a smooth and level loading surface. The bottom of the specimens, being cast against a flat wood plate, was adequately smooth and level. The test frame is secured from rotating during the test. Two displacement transducers were also installed between upper and lower stub at two opposite sides to check any possible inclination during test. The maximum observed difference in measurement between these two transducers were about 2.6mm.

Figure 5.22 shows an example of effect of concrete shrinkage and eccentric loading of 5mm for element specimen 3B. A free concrete shrinkage value of 600 microstrains was used according to the shrinkage model proposed by ACI 209R-92. These two conditions slightly reduce the stiffness and compressive strength.
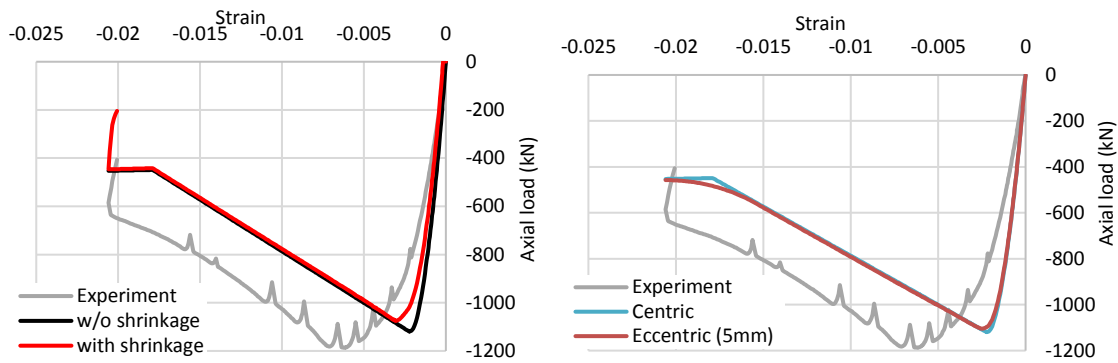
Figure 5.22 – Effect of shrinkage and eccentric loading

5.5. Conclusions

Based on the analysis of experimental and analytical results of the tested RC walls, the following conclusions were drawn:

- Boundary columns can effectively enhance the wall performance by increasing its ultimate deformation capacity and reducing damage level in the wall panel. However, the final failure of walls with boundary columns was more brittle compared to that of rectangular section walls.
- Damaged regions due to concrete crushing in rectangular walls spread widely over the lower portion of the walls. The damage tended to spread horizontally to the wall center and was limited in height.
- Flexure deformation was continuously dominant for rectangular walls while its contribution of flexural drift increased with the increase of drift ratios for walls with boundary columns. Results showed also that displacement component due to strain penetration is quite large and might be comparable to the shear component and, hence, should be considered in evaluation of the ultimate displacement.
- Transverse reinforcement spacing might be a key parameter when assessing detailing requirements when large drift capacity is desired. These failures need more studies to investigate the trends of ultimate drift as a function of transverse reinforcement and other key design parameters of RC wall.
- A simplified fiber section analysis based on the plastic hinge length and moment-curvature analysis is used to simulate cyclic lateral load-displacement relations for flexure, shear and strain penetration. Results of the simulation showed a very good agreement with experimental results for all drift components. This demonstrated the effectiveness of the empirical equation used to evaluate shear deformation component based on flexural component.
- The developed fiber model might be used to estimate ultimate deformation capacity for RC walls. A proper estimate of deformation capacity leads to an accurate

100

estimation of ductility capacity as well as a rational determination of the behavior factor for a structural system.

References

1. ACI, (2011), "Building code requirements for structural concrete (ACI 318-11) and commentary (ACI318R-11)", American Concrete Institute, MI, USA.

2. Bohl, A., Adebar, P., (2011), "Plastic Hinge Lengths in High-Rise Concrete Shear Walls", ACI Structural Journal, 108(2): 148-157.

3. Beyer, K., Dazio, A., Priestley, M. J. N., (2011), "Shear Deformations of Slender Reinforced Concrete Walls under Seismic Loading", ACI Structural Journal, 108(2): 167-177.

4. Dazio, A., Beyer, K., Bachmann, H., (2009), "Quasi-static cyclic tests and plastic hinge analysis of RC structural walls", Engineering Structures, 31(7): 1556-1571.

5. Dhakal R. P., Maekawa K., (2002), "Path-dependent cyclic stress–strain relationship of reinforcing bar including buckling", Engineering Structures, 24(11): 1383–1396.

6. Filippou, F. C., Popov, E. G., Bertero, V. V., (1983), "Effects of bond deterioration on hysteretic behavior of reinforced concrete joints", EERC Report No. UCB/EERC-83/19, Earthquake Engineering Research Center, University of California, Berkeley.

7. Hiraishi, H., (1984), "Evaluation of Shear and flexural deformations of flexural type shear wall". Bulletin of the New Zealand Society of Earthquake Engineering, 17(2):135–44.

8. Japan Building Disaster Prevention Association. Standard for seismic evaluation of existing reinforced concrete buildings. Tokyo; 2001.

9. Kazaz, I., (2013), "Analytical Study on Plastic Hinge Length of Structural Walls", ASCE Journal of Structural Engineering, 139(11.

10. Massone, L.M., Wallace, J. W., (2004), "Load deformation responses of slender reinforced concrete walls". ACI Structural Journal, 101(1):103–13.

11. Menegotto, M., Pinto, E., (1973), "Method of analysis for cyclically loaded reinforced concrete plane frames including changes in geometry and non-elastic behavior of elements under combined normal force and bending", Proceedings of IABSE Symposium on Resistance and Ultimate Deformability of Structures Acted on by Well-Defined Repeated Loads, Lisbon, 1973, pp. 15–20.

12. Mohamed, N., Farghaly, A. S., Benmokrane, B., Neale, K. W., (2013), "Flexure and Shear deformation of GFRP reinforced Shear walls". ASCE Journal of Composites for Construction 18(2): 04013044(1-8).

13. National Institute for Land and Infrastructure Management. Commentary of structural technique standard for buildings. Tokyo; 2015.

14. Parra, P. F., Moehle, J. P., (2014), "Lateral buckling in reinforced concrete walls", Proceedings of the 10th U.S. National Conference on Earthquake Engineering, Anchorage 21–25 July 2014.

12. Priestley, M. J. N., Calvi, G. M., & Kowalsky, M. J. (2007). Displacement-based Seismic Design of Structures. IUSS Press (p. 721).

13. Takahashi, S., Yoshida, K., Ichinose, T., Sanada, Y., Matsumoto, K., Fukuyama, H.,

Suwada, H., (2013), "Flexural Drift Capacity of Reinforced Concrete Wall with Limited Confinement", ACI Structural Journal, 110(1) 95-104.

14. Scott, B. D., Park R., Priestley, M. J. N., (1982), "Stress-strain behavior of concrete confined by overlapping hoops at low and high strain rates", Journal of the American Concrete Institute, 79(1), 13–27.

15. Yassin, M. H. M., (1994). "Nonlinear analysis of prestressed concrete structures under monotonic and cyclic loads", PhD Thesis, University of California, Berkeley.

CHAPTER 6 NUMERICAL AND ANALYTICAL STUDIES ON ULTIMATE DISPLACEMENT OF RC WALLS

6.1. Introduction

For accurate assessment of performance levels in reinforced concrete members, it is important to well define deformation limits at particular damage states. For RC walled building, investigation of the deformation limits of RC structural walls is required to define limit states and corresponding limiting values. Numerical investigations were carried out on barbell shape and rectangular RC walls with confined boundaries to evaluate response curves and ultimate deformations. Although FEM is superior and give more results, the main objective was to assess the ability of fiber sectional model in predicting the ultimate displacement compared to FEM analysis. In this manner, fiber sectional analysis might be used as simple alternative.

A nonlinear 2D and 3D finite elements models were built in order to simulate the load-deformation relations under monotonic loading as well as cracking and damage patterns of previously tested walls. A sectional fiber model combined with plastic hinge length and shear deformation component is used to simulate the backbone curves and the ultimate deformation with less computational cost compared to 3D FE analysis.

An analytical equation is proposed to estimate the ultimate displacement of RC structural walls with rectangular cross section. The proposed equation relate the ultimate deformation to key design parameters that is wall length, shear span, axial load ratio, and transverse reinforcement ratio at confined boundaries. The proposed equation was verified with existing experimental and simulation data.

6.2. Nonlinear Finite Elements Analysis

6.2.1. 2D Finite Element Analysis

Numerical analyses were conducted under monotonic loading to investigate the envelope of lateral load response of the tested walls as well as the damage distribution. Commercial FEM software called FINAL was user in this study (ITOCHU, 2011). Figure 6.1 shows FE mesh for BC's specimens. Four-node plane-stress quadrilateral elements were used to model the RC walls. The foundation and loading beams were assumed to behave elastically. All nodes at the bottom of the foundation beam were pin-supported to restrain vertical and lateral displacement. The constant axial loads on the top of boundary regions were applied in the first step and then the lateral load was applied at the loading beam center point under displacement control.
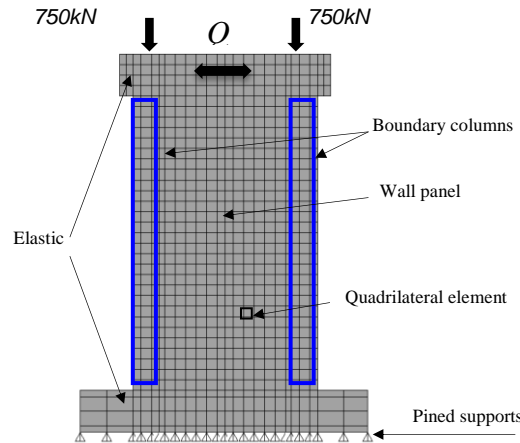
Figure 6.1 – FE mesh for BC's specimens

Truss elements were used to model the vertical reinforcements in confined boundary regions considering bond effect, which was modelled using Elmorsi model (Elmorsi *et al.*, 2000). Stress-strain relation for reinforcement material follows Ciampi's model (Ciampi *et al.*, 1982). All Horizontal and vertical reinforcements in wall panels as well as transverse reinforcement in confined regions were smeared assuming a perfect bond. The modified Ahmad model (Naganuma, 1995) for the compressive stress-strain relation of concrete was used for both ascending and descending branches for confined and unconfined concrete. Mechanical properties of material used in the analysis are thus given in Table 5.2 and Table 5.3 for concrete and reinforcement, respectively. The Kupfer-Gerstle's failure criterion was adopted for failure in biaxial compression and in tension-compression (Kupfer and Hilsdorf, 1969). The Naganuma model was adopted for concrete tension stiffing (Naganuma *et al.*, 2004). Uniaxial tensile strength is used for judging cracks under uniaxial and biaxial tension. Stress-strain relationship is assumed linear up to cracking. The smeared crack model with a fixed angle concept was used to express cracking of concrete. The shear transfer model after cracking proposed by

Naganuma was used (Naganuma, 1991). Effects of strain penetration was not considered in the analysis.

Figure 6.2 shows cyclic lateral load-drift angle relationships obtained experimentally and monotonic envelop obtained by 2D FE analysis. Table 6.1 compares damage characteristic points: flexural cracking, yielding of longitudinal reinforcement in confined end regions, and peak load derived from experiment and monotonic FE analysis. The ultimate deformation was defined by either 20% degradation of load carrying capacity from the peak load or the maximum observed drift. The results show that the model is capable of simulating the entire steps of the nonlinear behavior of the concrete wall such as initial stiffness, cracking, steel yielding, and peak load with good accuracy.

Table 6.2 shows comparison of ultimate deformation point between experimental and 2D FE analysis. Although the model tends to underestimate the ultimate deformation points, the model well captures their trend since ultimate drift of BC's specimens are larger than those of NC's specimens, and that for the same wall configuration, ultimate drift in specimens with 40mm transverse reinforcement spacing is larger than those with 80mm spacing.
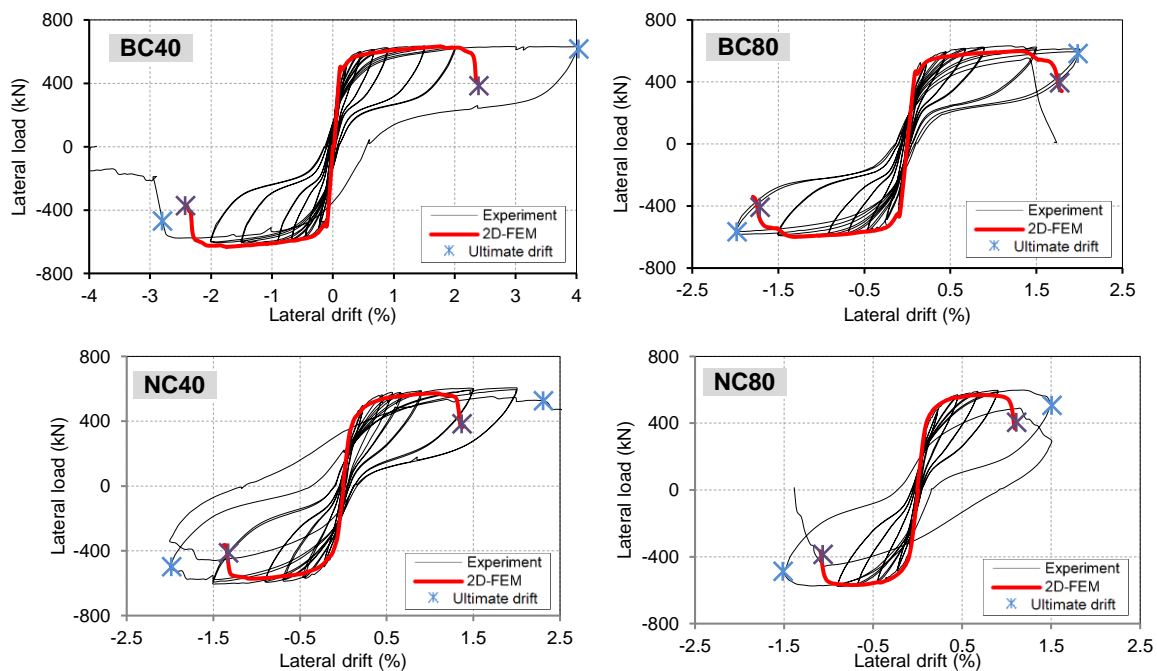
Figure 6.2 – Cyclic lateral load-drift angle relations and monotonic envelopes

Figure 6.3 illustrates cracks distribution and damage pattern at ultimate. Crack distribution is less spread in the case of walls with boundary elements compared to that of rectangular walls. Damage for walls with boundary column is concentrated at the outside bottom of boundary columns, while for walls without boundary damage extended along the bottom of confined regions. This is due to the boundary columns that carry a large amount of axial force to reduce axial stress level in wall panels resulting in less

106

damage. The built model predicted damage pattern quite well, and has predicted the ability of boundary columns in reducing damage level and crack distribution.
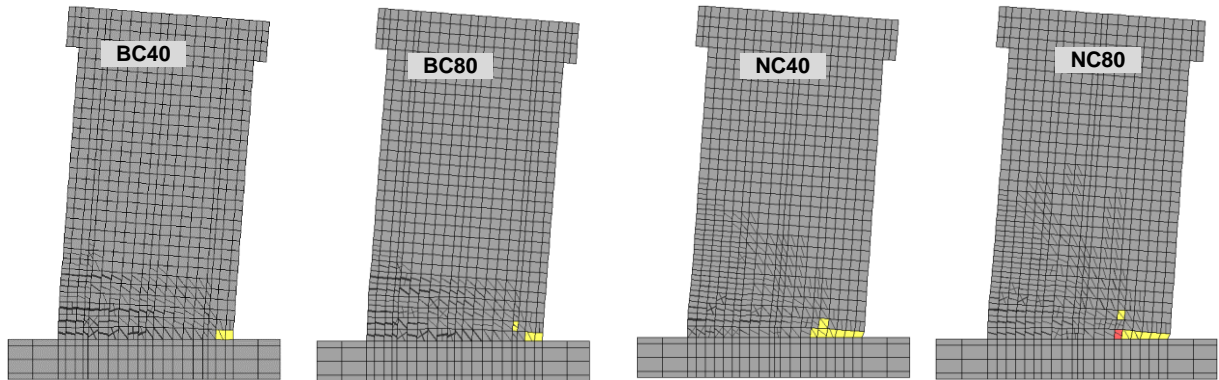
Figure 6.3 – Damage pattern at 1.5% lateral drift ratio.

Table 6.1 – Comparison of characteristic damage points

| Specimen | Flexural cracking point | | | | Steel yielding point | | | | Peak load point | | | |
| | Experiment | | Analysis | | Experiment | | Analysis | | Experiment | | Analysis | |
	R (%) (+)/(-)	Q (kN) (+)/(-)	R (%)	Q (kN)	R (%) (+)/(-)	Q (kN) (+)/(-)	R (%)	Q (kN)	R (%) (+)/(-)	Q (kN) (+)/(-)	R (%)	Q (kN)
BC40	0.12/-0.10	443/-441	0.06	346	0.29/-0.25	562/-521	0.11	546	1.41/-1.47	634/-608	1.75	633
BC80	0.08/-0.07	418/-338	0.07	400	0.26/-0.33	487/-507	0.11	546	1.17/-1.45	633/-592	1.29	599
NC40	0.07/-0.09	328/-379	0.05	231	0.19/-0.20	478/-449	0.17	505	1.91/-1.46	606/-604	1.06	573
NC80	0.09/-0.08	334/-331	0.05	231	0.30/-0.12	467/-332	0.17	505	1.16/-0.87	598/-578	0.69	570

Table 6.2 – Comparison between experiment and 2D-FEM analysis for ultimate drift point

| Specimen | Ultimate drift point | | |
| | Experiment | Analysis | Ratio |
	R_{exp} (%) (+)/(-)	R_{ana} (%)	R_{exp}/R_{ana}
BC40	4.00/-2.75	2.32	1.45
BC80	2.00/-2.00	1.72	1.16
NC40	2.38/-2.00	1.32	1.66
NC80	1.50/-1.50	1.07	1.40
Note: The ratio of experimental and analytical lateral drift was calculated based on the average value of the experimental ultimate drift between positive and negative loading directions.			

6.2.2. 3D Finite Element Analysis

Numerical analyses with 3D FE model were also conducted under monotonic loading to verify the ability of 3D modelling for the estimation of ultimate drift, since 2D model was not able to well capture it. In 3D FE model, eight-node elements were used to model the RC walls. The foundation and loading beams were assumed to behave elastically. Similar constitutive material models used for 2D analysis were also used for 3D analysis. All

reinforcements, including longitudinal reinforcing bars in confined regions were smeared assuming a perfect bond with concrete. The analysis employed Ottosen's four-parameter model (Ottosen, 1977) to define the failure criterion of concrete. Effects of strain penetration was not considered in the analysis.

Figure 6.4 shows cyclic lateral load-drift angle relationships obtained experimentally and monotonic envelop obtained by 3D FE analysis. The analysis tends to simulate slightly higher initial stiffness. However, the analytical backbone curve agrees very well with the experimental one until ultimate drift point, especially in positive loading direction. Similarly to 2D models, 3D models could predicted the ability of boundary columns in reducing damage level and crack distribution, since crack distribution is less spread in the case of walls with boundary elements compared to that of rectangular walls (Figure 6.5). Table 6.4 shows comparison of ultimate deformation point between experimental and 3D FE analysis. The model estimates very well the ultimate deformations of the tested wall specimens.
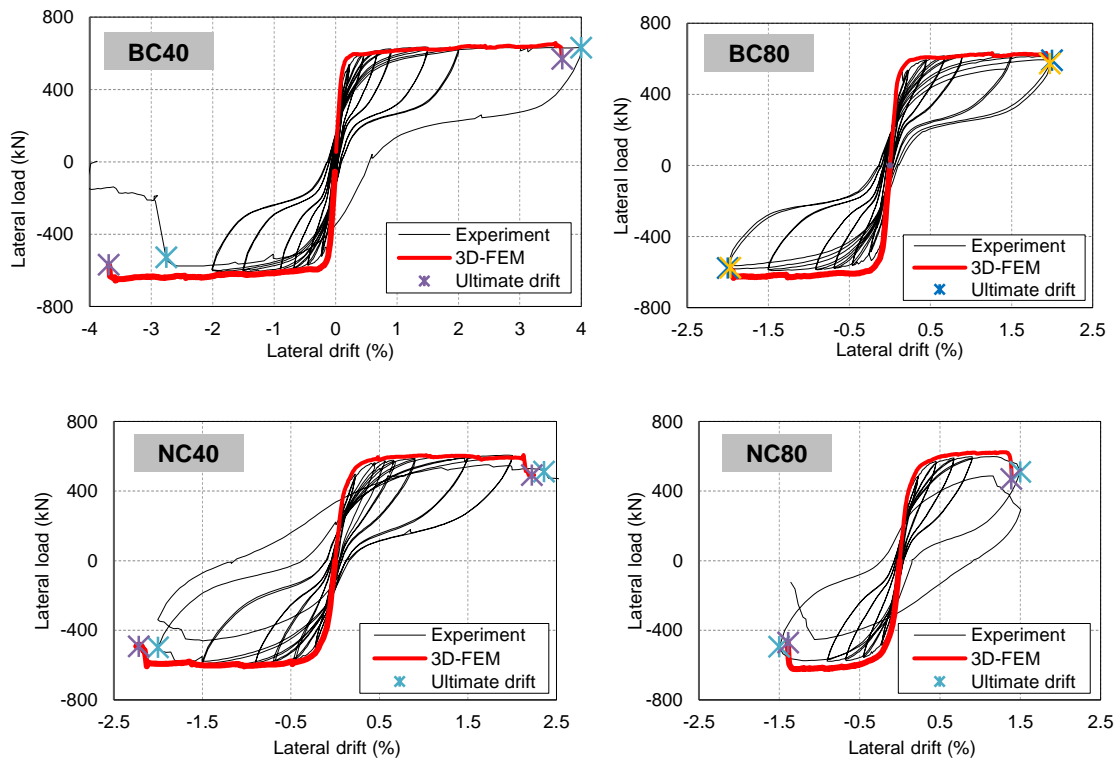
Figure 6.4 – Experimental hysteretic and 3D-FEM lateral load - drift angle relations
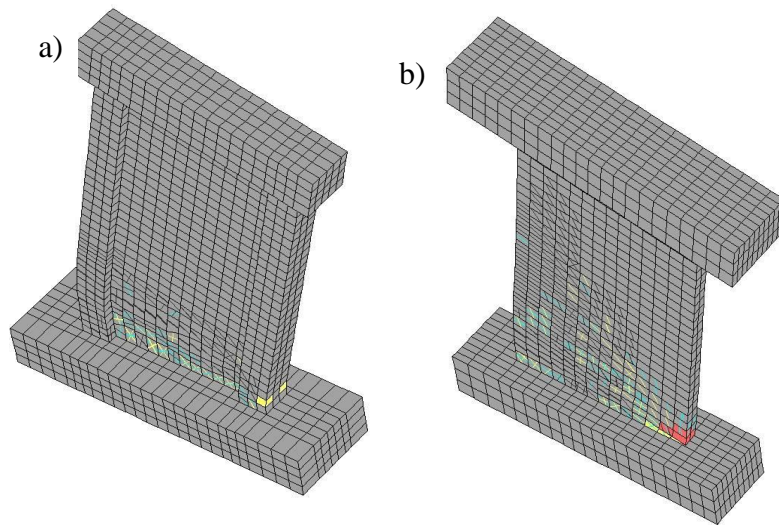
Figure 6.5 – Damage pattern at 1.5% drift ratio of (a) BC80 and (b) NC80

Table 6.3 – Comparison between experiment and 3D-FEM analysis for ultimate drift point

| Specimen | Ultimate drift point | | |
| | Experiment | Analysis | Ratio |
	R_{exp} (%) (+)/(-)	R_{ana} (%)	R_{exp}/R_{ana}
BC40	4.00/-2.75	3.69	0.92
BC80	2.00/-2.00	1.97	1.02
NC40	2.38/-2.00	2.22	0.99
NC80	1.50/-1.50	1.43	1.05
Note: The ratio of experimental and analytical lateral drift was calculated based on the average value of the experimental ultimate drift between positive and negative loading directions.			

6.3. Fiber Sectional Analysis

A sectional fiber model analysis was conducted to compute the backbone lateral load - drift angel relations as well as to estimate the ultimate lateral drift based on the plastic hinge length and moment-curvature analysis (Figure 6.6). The wall section was divided into small concrete elements along the width direction and each longitudinal reinforcing bar was modelled as an independent steel element (Figure 6.7). The monotonic envelope curve for plain and confined concrete in compression follows the modified Kent and Park model (Scott *et al.* 1982). The tensile contribution of concrete was neglected. The numerical model used for reinforcing steel was based on Menegotto-Pinto model as extended by Filippou (Filippou *et al.*, 1983) to include isotropic strain hardening effects.
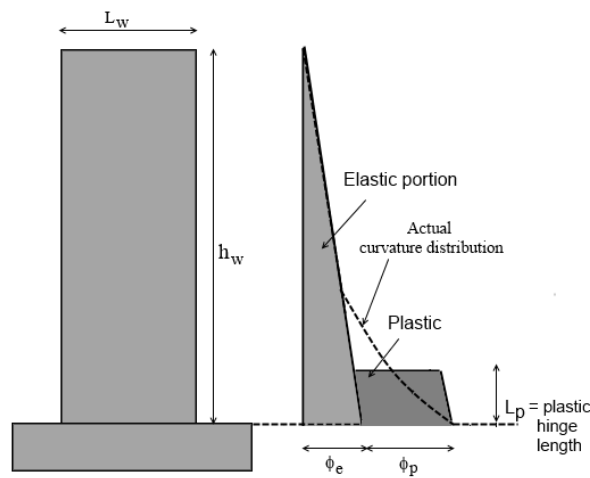
Figure 6.6 – Curvature and deformation distribution along the wall height
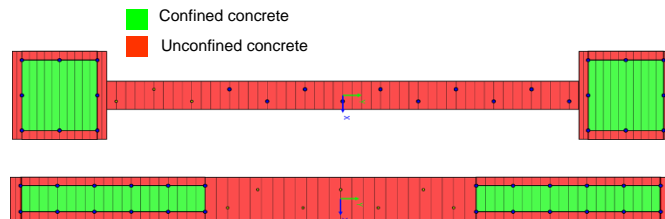
Figure 6.7 – Walls sectional fiber meshing

The total drift is obtained by the sum of the flexural component, the shear component, and the component due to strain penetration. The flexural displacement component is computed by Eq. (3) as the sum of the elastic and the plastic components based on the curvature distribution. The curvature is divided into elastic and plastic curvatures, and each curvature was used to derive elastic drift, Δ_{fe}, and plastic drift, Δ_{fp}, as Eq. (6.2) and Eq (6.3), respectively.

$$R_f(\%) = \frac{\Delta_{fe} + \Delta_{fp}}{H} \times 100 \tag{6.1}$$

with,

$$\Delta_{fe} = Q.H^3/(3EI) \tag{6.2}$$

$$\Delta_{fp} = \frac{1}{2}\phi_p l_p^2 + \phi_p l_p (H - l_p) \tag{6.3}$$

Where Q is the lateral load, H the wall height, E Young's modulus of concrete, I the second moment of inertia of the wall section, ϕ_p the plastic curvature, l_p the plastic hinge length.

The plastic hinge length corresponds to the yielding of longitudinal reinforcement and plastic curvature distribution. The plastic hinge length calculations significantly influence the estimation of the force-displacement response of that wall in the inelastic region. Existing plastic hinge length equations are usually proposed for RC columns and applicable for RC walls. Observations from the tested walls have shown that the damage region was limited in height and tends to spread more horizontally toward wall center. Similarly, observations from previous experimental studies indicate that the compressive failure region is quite limited within a height of about 2.5 times the wall thickness (Markeset and Hillerborg, 1995), Takahashi *et al.*, 2013). Hence, the plastic hinge length was estimated to be three times the wall panel thickness.

The shear displacement component of walls is estimated using the empirical equation developed by Beyer *et al.* (2011) as given by Eq. 6.4 This empirical equation was developed based on a series of experimental and analytical studies of slender reinforced concrete walls under seismic loading. The shear deformation component was added to the flexural component to obtain the total deformation without considering flexure - shear interaction.

$$\Delta_s = 1.5\Delta_f\left(\frac{\varepsilon_m}{\phi\tan\beta}\right)\frac{1}{H_w} \tag{6.4}$$

with

$$\tan\beta = \frac{j_d}{V}\left(f_l t_w + \frac{A_{sw}f_{yw}}{s}\right) \quad (\beta \le 90°) \tag{6.5}$$

where, Δ_f is the flexural lateral displacement, β is the crack angle (45° was considered), ε_m is the axial strain at the center of the wall section, ϕ is the curvature of the wall section, j_d is the lever arm between compression and tensile resultants, V is the shear force, f_l is the tensile strength orthogonal to the crack, t_w is the wall thickness, A_{sw} is the area of the shear reinforcement, f_{yw} is the yield strength of shear reinforcement, and s is the spacing of shear reinforcement.

The component due to strain penetration is given as:

$$\Delta_{sp} = \phi\, L_{sp} H_w \tag{6.6}$$

111

with,

$$L_{sp} = 0.022 f_y d_b \tag{6.7}$$

where H_w is the shear span, ϕ is the curvature of the wall section, ϕ_p is the plastic curvature, L_p is the plastic hinge length, L_{sp} is the strain penetration length, f_y yield strength of longitudinal reinforcement, d_b diameter of longitudinal bar.

The ultimate displacement was computed based on the limit compressive strain, ε_{cu}, proposed by Mander *et al.* (1988).

$$\varepsilon_{cu} = 0.004 + \frac{1.4 \rho_s f_{yh} \varepsilon_{sm}}{f'_{cc}} = \tag{6.8}$$

where ρ_s is the volumetric ratio of transverse reinforcement in confined end regions, f_{yh} the yield strength of confining reinforcement, ε_{sm} the fracture strain of confining reinforcement (0.005 was used based on reinforcing bars material test), f'_{cc} the compressive strength of confined concrete. Figure 6.8 shows stress-strain relations for confined concrete regions of the tested wall along with limit compressive strain, ε_{cu}, computed by Eq. 6.8 represented in the figure by red diamond. In the analysis, when the extreme compressive concrete fiber reached the limit compressive strain, ε_{cu}, the analysis was terminated and the corresponding drift was considered as the ultimate drift.

The computed relations between lateral load, Q, and lateral drift angle, R, are compared with the experimental hysteresis curves in Figure 6.9. Although the computed peak load is slightly smaller than the experimental value, the computed backbone curve well simulates envelop of experimental results. It is noted that the flexural ultimate drift is especially well simulated (Table 6.4) with less computational effort compared to 3D FE analysis.
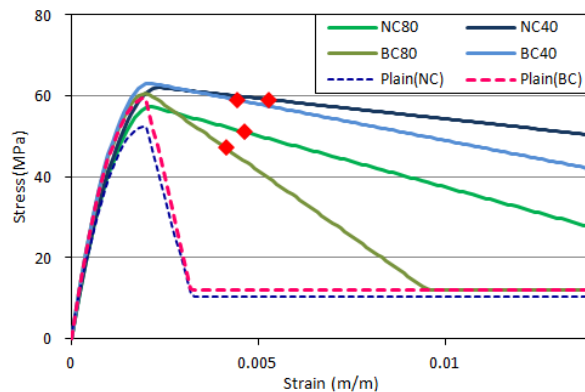
Figure 6.8 – Stress-strain relations for concrete with limit compressive strains
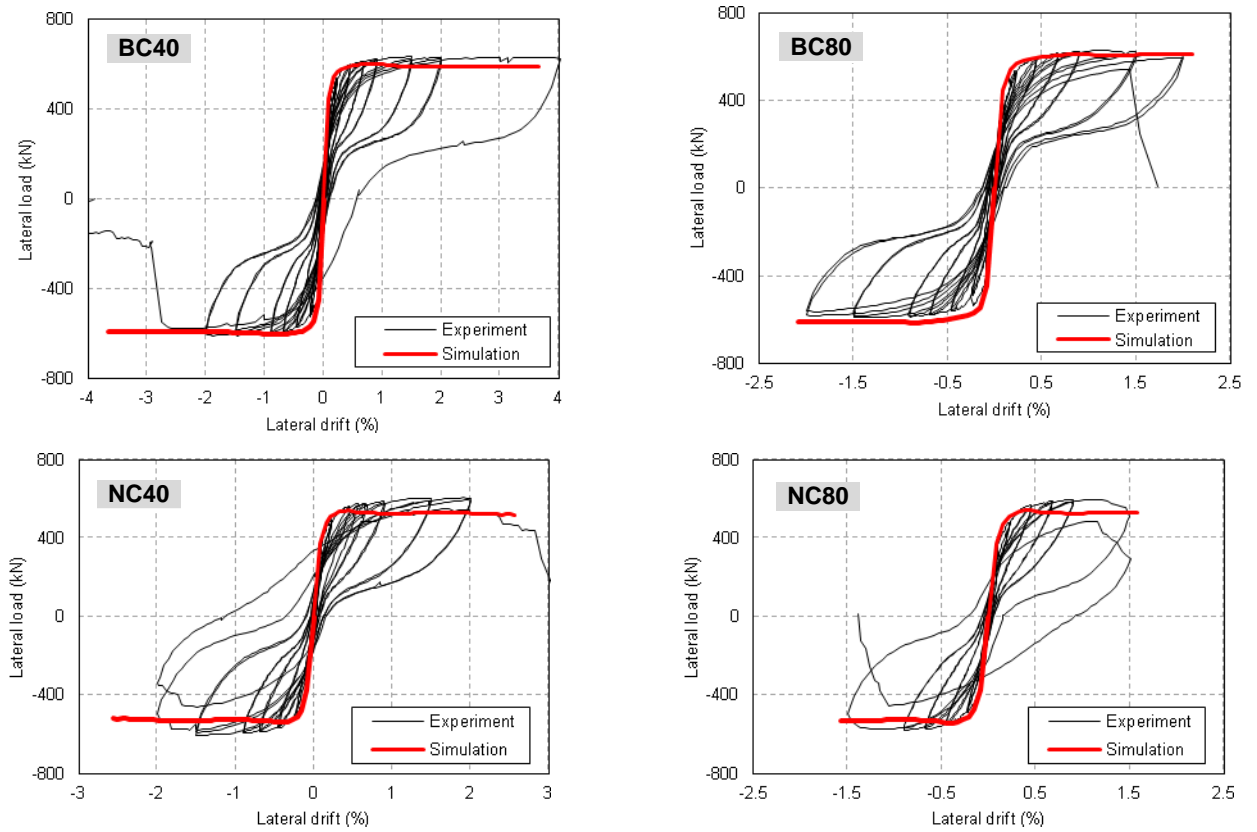
Figure 6.9 – Experimental hysteretic and sectional analysis lateral load - drift angle relations

Table 6.4 –Comparison between experiment and fiber analysis for ultimate drift point

| Specimen | Ultimate drift point | | |
| | Experiment | Analysis | Ratio |
	R_{exp} (%) (+)/(-)	R_{ana} (%)	R_{exp}/R_{ana}
BC40	4.00/-2.75	3.66	1.05
BC80	2.00/-2.00	2.09	0.98
NC40	2.38/-2.00	2.55	0.97
NC80	1.50/-1.50	1.58	0.97
Note: The ratio of experimental and analytical lateral drift was calculated based on the average value of the experimental ultimate drift between positive and negative loading directions.			

6.4. Analytical Prediction of Ultimate Displacement of RC structural walls for Performance-Based Design

Performance based assessment of RC buildings relies on comparison of deformations capacities with the performance based limits. These deformation limits significantly affect the assessment result so their accuracy plays a critical role. Provisions for performance assessment of reinforced concrete structures include deformation limits for RC wall members at specific limit states to estimate the performance of components and structures. The criteria are defined in terms of plastic hinge rotations and total drift ratios for the governing behavior modes of flexure or shear, respectively. Criteria related to strain limits are also defined for concrete in compression and steel in tension at serviceability and damage-control limit states as a vital component of direct displacement-based design procedures at specific limit states.

Although, the terminology used for damage states differs in the literature. Usually, three discrete component performance levels (damage limitation, life safety, collapse prevention) corresponding to two intermediate component performance ranges (damage control and limited safety) are defined. Collapse Prevention level deformation capacities for flexural members are taken at ultimate lateral displacement at which capacity begins to degrade rapidly, and limit safety range is usually limited by 75% of the ultimate lateral displacement. Thus, evaluation of the ultimate lateral displacement of flexural RC walls plays a significant role in defining these two later performance levels (life safety and collapse prevention)

An analytical equation is proposed to estimate the ultimate displacement of RC structural walls with rectangular cross section. The proposed equation relates the ultimate deformation to main key design parameters that is wall length and shear span, axial load ratio, and transverse reinforcement ratio at confined boundaries. The proposed equation is verified with existing experimental data, and with existing numerical simulation based on fiber analysis.

6.4.1. Proposed equation for ultimate displacement prediction

The total lateral displacement of cantilever RC walls is taken as the sum of the flexural and the shear displacement components as well as the component due to strain penetration:

$$\Delta = \Delta_f + \Delta_s + \Delta_{sp} \tag{6.9}$$

with Δ_f is the flexural displacement, Δ_s is shear displacement, Δ_{su} is displacement due to strain penetration.

For the displacement-based seismic design and assessment of reinforced concrete elements, Priestley *et al.* (2007) recommended that the flexural displacement capacity be estimated using the plastic hinge concept in which the flexural displacement at the top can be computed as the sum of the elastic and the plastic components (Figure 6.10(a)):

$$\Delta_f = \Delta_{fe} + \Delta_{fp} \tag{6.10}$$

Then,

$$\Delta = \Delta_{fe} + \Delta_{fp} + \Delta_s + \Delta_{sp} \tag{6.11}$$

The curvature at yielding ϕ_y is computed based on the yield strain of longitudinal reinforcement (Figure 6.10(b)):

$$\phi_y = \frac{\varepsilon_y}{d - c} \tag{6.12}$$

with ε_y is yield strain of longitudinal reinforcement, d is effective depth, defined as the distance between the compression edge and the center of the boundary column; and c is the neutral axis depth.

Based on extensive analyses of bridge columns and rectangular walls (Priestley *et al.* 1996, Priestley & Kowalski 1998) with axial load ratio of $0 \le N/f'_c A_g \le 0.4$ and longitudinal reinforcement ratio of $1\% \le \rho_l \le 4\%$, the yield curvature, ϕ_y, for RC walls with longitudinal reinforcement concentrated at boundaries can be expressed as :

$$\phi_y l_w = 2.0\varepsilon_y \pm 5\% \tag{6.13}$$

where l_w is wall length.

This implies that yield displacement can be expressed in the form:

$$\Delta_{fy} = \left(\frac{2\varepsilon_y}{l_w}\right)\frac{H_w^2}{3} \tag{6.14}$$

where H_w is wall shear span.

Based on plastic hinge concept, the plastic displacement is given by:

$$\Delta_{fp} = L_p \phi_p \left(H_w - 0.5L_p\right) \tag{6.15}$$

The shear displacement of walls is estimated using the semi-empirical equation developed by Beyer *et al.* (2011) given by:

$$\Delta_s = 1.5\Delta_f \left(\frac{\varepsilon_m}{\phi \tan \beta} \right) \frac{1}{H_w} \tag{6.16}$$

where ε_m and ϕ are the axial strain at the center of the wall section and the curvature of the wall section, respectively, and are derived from moment-curvature analysis, β is the crack angle (45° was considered).

The ultimate displacement can be written as:

$$\Delta_u = \Delta_{fy} + \Delta_{fpu} + \Delta_{su} + \Delta_{spu} \tag{6.17}$$

With,

$$\Delta_{fpu} = L_p \left(\phi_u - \phi_y \right) \left(H_w - 0.5L_p \right) \tag{6.18}$$

$$\Delta_{su} = 1.5\Delta_{fu} \left(\frac{\varepsilon_{mu}}{\phi_u} \right) \frac{1}{H_w} \tag{6.19}$$

$$\Delta_{spu} = \phi_u L_{sp} H_w \tag{6.20}$$

with,

$$L_{sp} = 0.022 f_y d_b \tag{6.21}$$

where H_w is the shear span, ϕ_u is the ultimate curvature of the wall section, ϕ_p is the plastic curvature, L_p is the plastic hinge length, ε_{mu} is the axial strain at the center of the wall section at ultimate, L_{sp} is the strain penetration length, f_y is the yield strength of longitudinal reinforcement in confined boundary, d_b is the diameter of longitudinal bar.

The ultimate curvature ϕ_u is computed based on the ultimate strain of concrete (Figure 6.10(c)), assuming plain sections remain plane at ultimate:

$$\phi_u = \frac{\varepsilon_{cu}}{c} \tag{6.22}$$

where ε_{cu} is the ultimate compressive strain of concrete, c is the neutral axis depth.
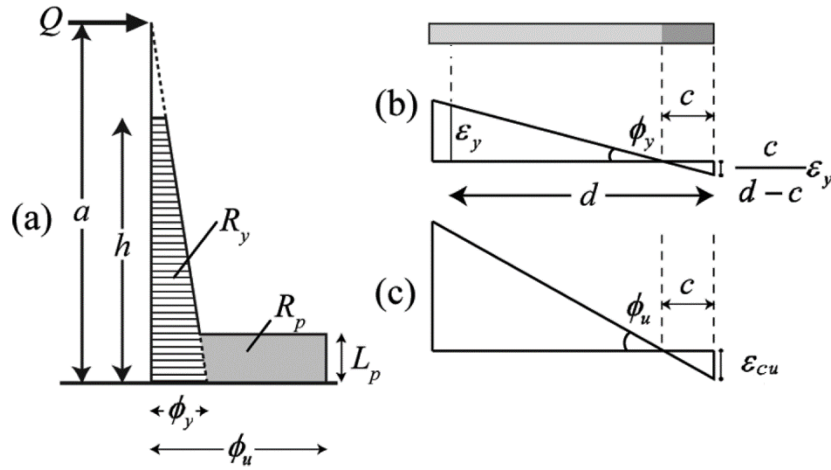
Figure 6.10 − Plastic hinge concept

The ultimate compressive strain, ε_{cu}, is given by Mander *et al.* (1988) as:

$$\varepsilon_{cu} = 0.004 + \frac{1.4\rho_s f_{yh}\varepsilon_{sm}}{f'_{cc}} = 0.004 + \frac{1.4\rho_s f_{yh}\varepsilon_{sm}}{Kf'_c} \tag{6.23}$$

where ρ_s is the volumetric ratio of transverse reinforcement in confined boundary, f_{yh} is the yield strength of confining reinforcement, ε_{sm} is the fracture strain of confining reinforcement, f'_c is the compressive strength of concrete, f'_{cc} the compressive strength of confined concrete, K is the a factor that accounts for the strength increase due to confinement. Based on the modified Kent and Park concrete model (1982), the K factor is given by:

$$K = 1 + \frac{\rho_s f_{yh}}{f'_c} \tag{6.24}$$

Substituting Eq. (6.22) into Eq. (6.23) gives:

$$\phi_u c = 0.004 + \frac{1.4\rho_s f_{yh}\varepsilon_{sm}}{Kf'_c} \tag{6.25}$$

The neutral axis depth can be determined from forces equilibrium at ultimate condition as:

$$N + \sum A_{st}f_y + \sum A_{sc}f_y = 0.85f'_c t_w c \tag{6.26}$$

where N is applied axial load, A_{st} is the area of longitudinal bars in tension, A_{sc} is the area of longitudinal bars in compression, f_y is the yield strength of the longitudinal reinforcement, f'_c is the concrete compressive strength, and c is the neutral axis depth.

By assuming $A_{st} = A_{sc}$, which is usually the case for RC structural walls with symmetric confined boundaries, and by normalizing by axial load ratio $\eta = N/(f'_c t_w l_w)$, Eq. (6.26) become:

$$c = \frac{l_w \eta}{0.85} \tag{6.27}$$

Substituting Eq.(6.26) into Eq.(6.24) gives the ultimate curvature as:

117

$$\phi_u = \frac{0.85}{l_w \eta}\left(0.004 + \frac{1.4\rho_s f_{yh}\varepsilon_{sm}}{Kf'_c}\right) \tag{6.28}$$

In Eq.(6.19) ε_m is the axial strain at the center of the wall section. By geometric compatibility, axial strain at the center of wall section at ultimate:

$$\varepsilon_{mu} = \varepsilon_{cu}\frac{0.5l_w - c}{c} \tag{6.29}$$

Substituting Eq. (6.27) into Eq. (6.29) gives:

$$\varepsilon_{mu} = \varepsilon_{cu}\left(\frac{0.425}{\eta} - 1\right) \tag{6.30}$$

Substituting Eq.(6.30) into Eq.(6.19), Eq.(6.13) into Eq. (6.18), and Eq.(6.28) into Eqs. (6.18) and (6.19), an analytical relationship is established between the ultimate displacement and key design parameters for RC walls as:

$$\Delta_u = \Delta_{fy} + \Delta_{fpu} + \Delta_{su} + \Delta_{spu}$$

where,

$$\Delta_{fy} = \frac{1}{3}\phi_y H_w^2$$

$$\Delta_{fpu} = L_p(\phi_u - \phi_y)(H_w - 0.5L_p)$$

$$\Delta_{su} = 1.5\Delta_{fu}\left(\frac{0.425 - \eta}{\eta\phi_u H_w}\right)\varepsilon_{cu}$$

$$\Delta_{spu} = 0.022 f_y d_b \phi_u H_w$$

with,

$$\phi_y = \frac{2\varepsilon_y}{l_w}$$

$$\phi_u = \frac{0.85}{l_w \eta}\varepsilon_{cu}$$

Key design parameters are wall length, wall shear span, axial load ratio, and transverse reinforcement ratio at boundaries.

6.4.2. Experimental and Numerical Verification

The accuracy of the proposed equation is verified with experimental data and results of fiber analysis. Parametric studies based on fiber based sectional analysis by Kono *et al.* (2015) compared eight equations for the equivalent plastic hinge length as shown in with different values of ε_m ranging from 1% to 8%. Based on their fourteen specimens, three

118

combinations of l_p and ε_m that give the best estimate of ultimate drift were found, namely $l_p=0.2l_w$ with $\varepsilon_m=6\%$, $l_p=0.33l_w$ with $\varepsilon_m=2\%$, and $l_p=0.5l_w$ with $\varepsilon_m=1\%$.

The equivalent plastic hinge length has been studied and several equations have been proposed. Although some researchers studied plastic hinge length in experiments to physically determine the plastic hinge in beams, columns, and walls, the procedure is still controversial. Kono *et al.* (2015) defined plastic hinge length as the ratio on wall length. Similarly, ACI 318 uses plastic hinge length of $0.5l_w$ to predict the design displacement.

6.4.2.1. Comparison with Tani et al. (2012) Database

The proposed equation to predict ultimate drift of RC walls was compared to experimental database from Tani *et al.* (2012) study. In this study, an experimental database of about 119 RC rectangular walls was made to study accuracy of ultimate flexural and shear capacity estimation methods, and to assess the influence of the key parameters on the ultimate deformation capacity of RC walls. The deformation where the capacity dropped to 80 % of the maximum capacity in the post-peak region was defined as the ultimate displacement. Twenty-two (22) specimens of rectangular RC walls with flexural failure mode were used. Walls with sliding or shear failure, without confined boundaries, or with low buckling index, $\rho_s d_b/d_t$, were excluded. As discussed in Chapter 4, the index $\rho_s d_b/d_t$, measures the effectiveness of transverse reinforcement to prevent buckling of longitudinal reinforcement in confined boundaries. It is suggested that keeping the buckling index below 1.2 will prevent buckling of longitudinal reinforcement. Table 6.5 shows the properties of the selected shear wall specimens and Table 6.6 shows the ratio of experimental and computed ultimate drifts ($_eR_u/_cR_u$) along with the mean and standard deviation of this ratio. Figure 6.11 shows the comparison between experimental and computed ultimate drifts. It can be seen from Table 6.6 that the combination of $l_p=0.5l_w$ and $\varepsilon_m=1\%$ gives the mean closest to 1 and the lowest standard deviation of $_eR_u/_cR_u$ among the three sets. Its mean and standard deviation of $_eR_u/_cR_u$ were 1.13 and 0.50, respectively.

Table 6.5 – Properties of RC wall specimens (Tani *et al.*, 2012)

No.	Specimen	Reference	Size (mm) $l_w \times h$	Thickness (mm) t_w	Confined region Size(mm)	Ver. rebar	f_y (MPa)	Transv. rebar	ρ_s (%)	f'_c(MPa)	ALR	SSR
1	RW1	Thomson et al.(2004)	1220x3658	102	102x190.5	8-#3	429	D4.8@76.2	0.50	31.6	0.10	3.12
2	RW2							D4.8@50.8	0.37	34.0	0.07	3.12
3	No.2	Tabata et al. (2003)	1500x2350	150	150x300	16-D10	569	D4@45	0.52	65.8	0.21	5.00
4	No.3									72.8	0.29	5.00
5	07N10	Kimura et al. (2006)	1500x2250	150	150x300	14-D13	704	D6@65	0.97	74.9	0.09	2.00
6	07N15									74.9	0.14	2.00
7	10N10									109.1	0.10	2.00
8	No.1	Hosoya (2007)	1070x1940	134	134x268	16-D10	433	D4@40	0.92	63.8	0.19	2.00
9	No.2					22-D10			0.87	63.8	0.19	2.00
10	I-1	Murakami et al.(2009)	1120x2140	140	140x210	16-D10	409	D4@40	0.67	65.2	0.15	2.00
11	I-2					16-D10		D4@35	1.15	65.2	0.20	2.00
12	M3	Greifenhagen et al.(2005)	900x610	80	80x90	2-D6	504	/	0.00	20.1	0.21	0.77
13	B112b	Hirosawa et al. (1970)	1700x1600	160	160x170	2-D19	377	/	0.00	18.3	0.11	1.00
14	SW9	Zhang et al.(2000)	700x1500	100	100x100	4-D20	375	D6@75	0.75	35.4	0.24	2.14
15	WSH5	Dazio et al.(2009)	2000x4030	150	150x260	6-D8	584	D4.2@50	0.21	38.3	0.13	2.28
16	WSH6					150x385	6-D12	576	D6@50	0.44	45.6	0.11	2.26
17	RCW-1	Takeda et al. (1999)	1200x1800	120	120x240	18-D10	712	D6@90	0.88	66.5	0.10	5.00
18	RCW-2									69.8	0.25	5.00
19	OFW-1	Furukawa et al. (2003)	1200x2000	120	120x240	10-D10	402	D6@90	0.88	51.0	0.10	5.00
20	OFW-2									53.0	0.10	5.00
21	OFW-3									51.0	0.25	5.00
22	OFW-4									52.0	0.25	
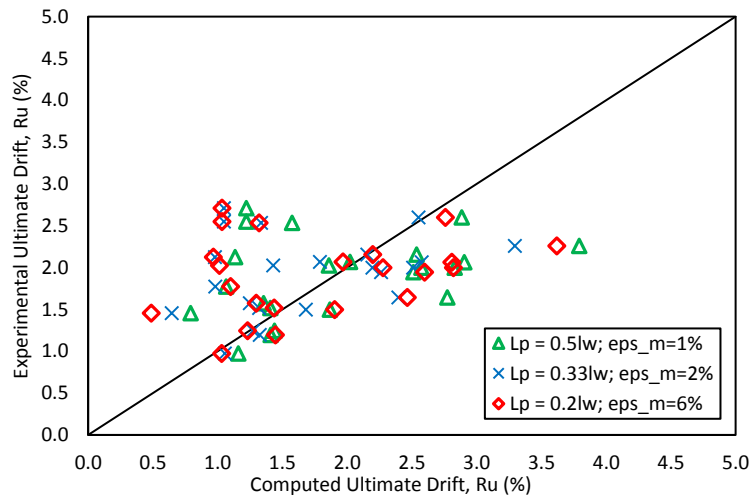
Figure 6.11 – Comparison of experimental (Tani *et al.*, 2012) and calculated ultimate drift

Table 6.6 – Ratio of experimental and calculated ultimate drifts of RC wall specimens

No.	Specimen	Reference	$_eR_u$	$0.2l_w+\varepsilon_m=6\%$		$0.33l_w+\varepsilon_m=2\%$		$0.5l_w+\varepsilon_m=1\%$	
				$_cR_u$ (%)	$_eR_u/_cR_u$	$_cR_u$ (%)	$_eR_u/_cR_u$	$_cR_u$ (%)	$_eR_u/_cR_u$
1	RW1	Thomson *et al.*(2004)	2.16	2.20	0.98	2.16	1.00	2.54	0.85
2	RW2		2.26	3.62	0.62	3.30	0.69	3.79	0.60
3	No.2	Tabata *et al.* (2003)	1.25	1.23	1.01	1.27	0.98	1.44	0.87
4	No.3		0.97	1.03	0.94	1.06	0.92	1.16	0.84
5	07N10	Kimura *et al.* (2006)	2.00	2.82	0.71	2.51	0.80	2.83	0.71
6	07N15		1.50	1.90	0.79	1.68	0.89	1.87	0.80
7	10N10		2.00	2.28	0.88	2.20	0.91	2.57	0.78
8	No.1	Hosoya (2007)	2.55	1.03	2.46	1.05	2.43	1.22	2.09
9	No.2		2.71	1.04	2.62	1.05	2.58	1.22	2.22
10	I-1	Murakami *et al.*(2009)	2.54	1.32	1.92	1.34	1.90	1.58	1.61
11	I-2		2.13	0.97	2.20	0.98	2.17	1.14	1.87
12	M3	Greifenhagen *et al.*(2005)	1.46	0.49	2.98	0.65	2.25	0.79	1.84
13	B112b	Hirosawa *et al.* (1970)	2.02	1.01	2.00	1.43	1.42	1.86	1.09
14	SW9	Zhang *et al.*(2000)	1.77	1.10	1.61	0.98	1.80	1.07	1.66
15	WSH5	Dazio *et al.*(2009)	2.07	1.97	1.05	1.79	1.16	2.02	1.02
16	WSH6		1.95	2.60	0.75	2.26	0.86	2.51	0.77
17	RCW-1	Takeda *et al.* (1999)	1.64	2.46	0.67	2.40	0.69	2.77	0.59
18	RCW-2		1.57	1.30	1.21	1.25	1.26	1.35	1.16
19	OFW-1	Furukawa *et al.* (2003)	2.07	2.81	0.74	2.58	0.80	2.90	0.71
20	OFW-2		2.60	2.76	0.94	2.55	1.02	2.89	0.90
21	OFW-3		1.20	1.45	0.83	1.33	0.90	1.41	0.85
22	OFW-4		1.52	1.44	1.06	1.32	1.15	1.41	1.08
				Mean	1.32	Mean	1.30	Mean	1.13
				SD	0.72	SD	0.60	SD	0.50

6.4.2.2.Comparison with Chanipa et al. (2017)

The proposed equation to predict ultimate drift of RC walls was also compared to experimental database and numerical results based on fiber analysis from Chanipa *et al.* 2017 study. In this study, the ultimate drift capacity of RC walls that fail by crushing of concrete and fracture of longitudinal reinforcement failure modes was assessed by a calibrated fiber-based model. The ultimate drift of tested RC wall specimens were compared to the ultimate drifts calculated by the proposed model using these three sets of l_p and ε_m in order to decide which combination of plastic hinge length and steel strain at the maximum tensile stress give the best estimation of ultimate drift (Figure 6.12). The test specimens used in this verification process cover experiments over the last 15 years and were selected by considering flexural failure, symmetry, good end region confinement, no shear sliding effect and $\rho_s d_b/d_t$ under 4. RC walls with very high buckling indexes were considered prone to errors in estimating ultimate drift and were excluded from the calibration process. Twenty-eight specimens were considered in this study.

Table 6.7 shows the properties of the selected shear wall specimens. Figure 6.13 Figure 6.14, and Figure 6.15 show comparison of experimental with computed ultimate drift for fiber analysis (Chanipa *et al.*, 2017) and proposed equation for the three sets of l_p and ε_m: $l_p=0.2l_w$ with $\varepsilon_m=6\%$, $l_p=0.33l_w$ with $\varepsilon_m=2\%$, and $l_p=0.5l_w$ with $\varepsilon_m=1\%$, respectively.

Table *6.8* shows the ratio of experimental and computed ultimate drifts ($_eR_u/_cR_u$) along with the mean and standard deviation of this ratio. It can be seen from

Table *6.8* shows that the combination of $l_p=0.2l_w$ with $\varepsilon_m=6\%$ gives the mean closest to 1 and the lowest standard deviation of $_eR_u/_cR_u$ among the three sets but in unconservative manner. Its mean and standard deviation of $_eR_u/_cR_u$ were 0.97 and 0.67, respectively. Although the model did not evaluate the experimental ultimate drift with very high accuracy, the proposed design equation could capture the trend of ultimate displacement and gives slightly conservative estimation depending on the set of l_p and ε_m.

Table 6.7 – Properties of RC wall specimens (Chanipa *et al.*, 2017)

No.	Specimen	Reference	Size (mm) l_wxh	Confined area size(mm)	Ver. rebar	f_y (Mpa)	Shear rebar	ρ_s (%)	f'_c (MPa)	Axail Level	Shear span ratio
1	WR-20	Oh et al. 2002 [19]	1500x2000	200x200	4-D13	449	D10@200	0.99	34.2	0.1	2.00
2	WR-10						D10@100	1.97	36.2		
3	WB			240x240	8-D13		D10@150	0.94	33.7		
4	No.1	Ando Corp. 2003 [20]	1500x2250	300x150	16-D10	569	D4@45	1.14	71.8	0.1	1.77
5	No.2								65.8	0.15	
6	No.3								72.8	0.2	
7	07N10	Takenaka Corp. 2006 [21]	1500x2250	300x150	14-D13	704	D6@65	1.9	74.9	0.1	2.00
8	07N15									0.15	
9	10N10								109.1	0.1	
10	No.1	Okumura Corp. 2007 [22]	1070x1940	268x134	16-D10	433	D4@40	1.56	63.8	0.2	2.00
11	No.2			402x134	22-D10			1.52			
12	No.3			268x134	17-D10	397	D4@35	2.65	66.9		
13	No.4						D4@40	1.97			
14	No.5	Okumura Corp. 2008	1070x1865	201x134	15-D10	435	D4@40	1.81	65.5	0.2	2.00
15	No.6		1070x2935						67.9		3.00
16	HPCW-01	Deng et al. 2008 [24]	1000x2000	240x100	4-D12+2-D6.5	D12=433.3 D6.5=361.6	D4@60	1.02	61.3	0.14	2.10
17	HPCW-02			340x100	4-D12+4-D6.5		D6@60	1.7			
18	HPCW-03				6-D12+2-D6.5		D5,D4@40	2.24			
19	HPCW-04			440x100	5-D12+6-D6.5		D6,D5,D4@40	2.1			
20	WSH1	Dazio et al. 2009 [25]	2000x4030	200X150	6-D10	547.3	D6@75	1.22	45	0.05	2.28
21	WSH2					583.1		1.25	40.5	0.06	
22	WSH3			260x150	6-D12	601		1.13	39.2	0.06	
23	WSH5			160x150	6-D8	583.7	D4@50	1.18	38.3	0.13	
24	WSH6			385x150	6-D12+2-D8	576	D6@50	1.82	45.6	0.11	2.26
25	I-1	Murakami et al. 2009 [26]	1120x2140	210X134	16-D10	409	D4@40	1.42	65.2	0.15	2.00
26	I-2						D4@35	2.32		0.2	
27	SW6-1	Zhang et al. 2010 [27]	1000x2000	200X125	6-D10	352	D4@80	0.66	37.5	0.3	2.20
28	SW6-3						D6@60	2.25			
29	SW-2		850x1600	188X125	4-D10		D4@83	0.56	32.6	0.16	2.06
30	SW-3						D6@63	2.2			
31	RW-A20-P10-S38	Tran and Wallace 2012 [28]	1220x2440	210X150	8-D13	475	D6@50	1.85	48	0.07	2.00
32	RW-A20-P10-S63				8-D19			1.76	48		
33	RW-A15-P10-S51		1220x1830		8-D13			1.85		0.08	1.50
34	RW-A15-P10-S78				4-D19+4-D16			1.76	56	0.06	
35	RW-A15-P2.5-S64									0.02	
36	WA	Kabeyasawa et al.2014 [29]	1650x1250	150x250	10-D10	375	D4@33	0.57	32.1	0.23	1.40
37	WB			250x150				0.68	31.3		1.32
38	WC		1750x1250	300x150	8D13	345		0.57	29.1	0.25	1.10
39	WD			450x100	12D10	365		0.85	31.2		
40	NC40	Kono et al. 2014 [9]	1750x2800	540x280	12-D10	377	D6@40	3	52.5	0.11	1.71
41	NC80						D6@80	1.87			
42	BC40			250x250	8-D10		D6@40	2.01	59.5		
43	BC80						D6@80	0.72			

Figure 6.12 – Comparison of experimental and computed ultimate drift by fiber sectional analysis (Chanipa *et al.*, 2017)

Figure 6.13 – Comparison of experimental with computed ultimate drift for fiber analysis (Chanipa *et al.*, 2017) and proposed equation ($L_p=0.5l_w$, and $\varepsilon_m=1\%$)
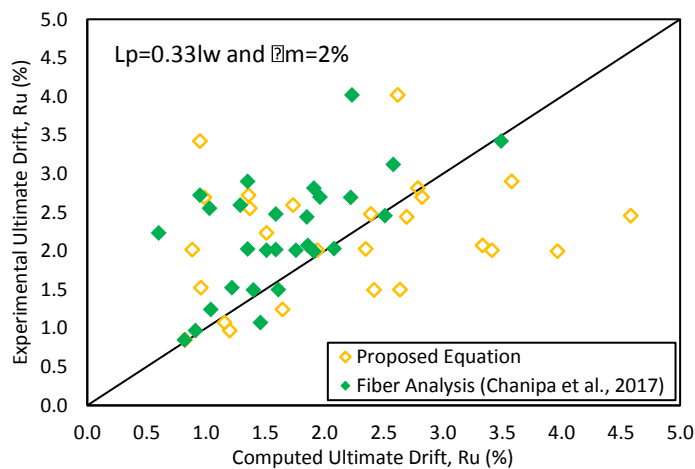
Figure 6.14 – Comparison of experimental with computed ultimate drift for fiber analysis (Chanipa *et al.*, 2017) and proposed equation ($L_p=0.33l_w$, and $\varepsilon_m=2\%$)
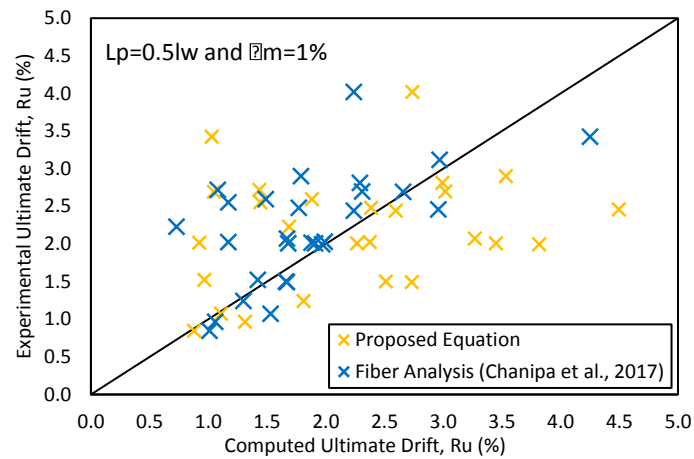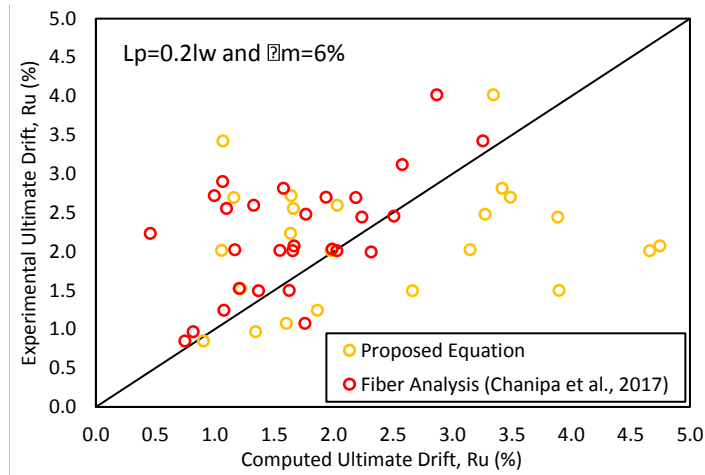
Figure 6.15 – Comparison of experimental with computed ultimate drift for fiber analysis (Chanipa *et al.*, 2017) and proposed equation ($L_p=0.2l_w$, and $\varepsilon_m=6\%$)

Table 6.8 – Ratio of experimental and calculated ultimate drifts of RC wall specimens

No.	Specimen	$_eR_u$	$0.2l_w+\varepsilon_m=6\%$		$0.33l_w+\varepsilon_m=2\%$		$0.5l_w+\varepsilon_m=1\%$	
			$_cR_u$ (%)	$_eR_u/_cR_u$	$_cR_u$ (%)	$_eR_u/_cR_u$	$_cR_u$ (%)	$_eR_u/_cR_u$
1	WR-20	2.70	3.49	0.77	2.82	0.96	3.02	0.89
2	WR-10	2.90	5.07	0.57	3.58	0.81	3.53	0.82
3	WB	2.81	3.42	0.82	2.79	1.01	3.00	0.94
4	No.1	1.49	2.67	0.56	2.42	0.62	2.73	0.55
5	No.2	1.24	1.87	0.67	1.65	0.75	1.81	0.69
6	No.3	0.97	1.35	0.72	1.20	0.81	1.31	0.74
7	07N10	2.00	5.86	0.34	3.97	0.50	3.82	0.52
8	07N15	1.50	3.90	0.38	2.64	0.57	2.51	0.60
9	10N10	2.01	4.66	0.43	3.41	0.59	3.45	0.58
10	No.1	2.55	1.67	1.53	1.37	1.86	1.44	1.77
11	No.2	2.72	1.64	1.65	1.36	2.00	1.44	1.89
12	HPCW-01	2.02	3.15	0.64	2.35	0.86	2.38	0.85
13	HPCW-02	2.48	3.28	0.76	2.39	1.04	2.39	1.04
14	HPCW-03	2.44	3.89	0.63	2.69	0.91	2.60	0.94
15	WSH3	2.03	6.90	0.29	5.22	0.39	5.44	0.37
16	WSH6	2.07	4.75	0.44	3.33	0.62	3.27	0.63
17	I-1	2.59	2.03	1.28	1.73	1.50	1.88	1.38
18	SW6-1	0.85	0.91	0.93	0.82	1.03	0.88	0.96
19	SW6-3	1.07	1.61	0.67	1.16	0.93	1.11	0.97
20	SW-2	2.23	1.64	1.36	1.51	1.48	1.69	1.32
21	RW-A20-P10-S38	3.12	7.29	0.43	5.15	0.61	5.12	0.61
22	RW-A15-P10-S51	2.46	6.56	0.37	4.58	0.54	4.50	0.55
23	WA	3.42	1.07	3.20	0.95	3.61	1.03	3.32
24	WB	2.69	1.16	2.32	0.99	2.73	1.05	2.57
25	WC	2.02	1.06	1.90	0.88	2.28	0.92	2.19
26	WD	1.52	1.22	1.25	0.96	1.59	0.97	1.58
27	BC40	4.02	3.35	1.20	2.62	1.53	2.74	1.47
28	BC80	2.01	1.98	1.01	1.94	1.04	2.27	0.89
			Mean	0.97	Mean	1.18	Mean	1.13
			SD	0.67	SD	0.75	SD	0.69

124

6.5. Plastic hinge length for ultimate displacement

6.5.1. Proposed equation for plastic hinge length

A simulation of proper ultimate deformation capacity leads to an accurate estimation of ductility capacity as well as a rational determination of the behavior factor for a structural system. In order to obtain an accurate force-displacement relationship from moment-curvature response of a wall section, a realistic value or empirical equation to compute the plastic hinge length is required.

Equivalent plastic hinge length, L_p, is a distance used by plastic hinge method that correspond to the height over which the inelastic curvatures are usually idealized to be uniform. Plastic hinge lengths is not necessarily directly related to quantities measured in the experiments; it is only important that when the strain limits in the form of the corresponding curvatures and the plastic hinge length are combined for a good estimate of the wall displacement for the considered limit state. The actual physical length over which the plasticity spreads is larger and referred as plastic zone. Plastic zone has been typically calibrated for the tension side corresponding to yielding region.

Although numerous empirical equations have been proposed in extant literature for prediction of plastic hinge length L_p, accuracy (or even the definition) of L_p remains an open issue, yet to be addressed adequately.

Previous studies on plastic hinge length mostly focused on developing empirical models based on the test results of RC beams and columns. However, the inelastic rotation performance of RC walls would differ from that observed for beams. Large differences has been noted among different expressions of plastic hinge length suggesting that the performance of these expressions in estimating ultimate displacement has not been systematically evaluated. The plastic hinge length for RC walls has been studied by several authors, including Paulay and Uzumeri (1975), who adapted an equation that was proposed for beams, as demonstrated by Eq.(6.31). Paulay and Priestley (1993) recommend $\alpha_1 = 0.5$ and $\beta_1 = 0.044$ for a lower limit in Eq.(6.31).

$$L_p = \alpha_1 0.8 l_w + \beta_1 h_w \tag{6.31}$$

Other expressions have incorporated effects such as shear, strain penetration (Hines *et al.*, 2004) or the level of axial load (Bohl and Adebar, 2011). Shear or strain penetration, one should consider the impact over the wall top displacement and its effect over the local strain within the plastic hinge. Shear in relatively slender walls accounts for approximately 30% of the lateral displacement at the location of the plastic hinge; however, this value reduces to approximately 10% for the top displacement (Massone and Wallace, 2004). This result indicates that its effect on the top displacement can be

neglected if a conservative analysis is required. Strain penetration only affects the top displacement. Experimental evidence from the tested RC walls has shown that strain penetration may contribute in more then 20% of the lateral displacement. Experimental evidence in RC walls from other experiments (Dazio *et al.*, 2009) indicates that strain penetration may account for approximately 10% of the top displacement for RC walls with an aspect ratio of 2.3 and therefore can be neglected.

Regarding the axial load, Bohl and Adebar (2011) investigated the dependency of the plastic hinge length to the axial load from a finite element model, resulting in Eq. (6.32), which is limited to $0.8l_w$.

$$L_p = \left(0.2l_w + 0.05h_w\right)\left(1 - 1.5\eta\right) \tag{6.32}$$

Where, η is the axial load ratio.

The expression indicates that high levels of axial load may considerably reduce the plastic hinge length compared with the case without axial load. It has been also recognized that the plastic hinge length typically increases with increase of drift levels (Kazaz, 2013).

A regression analysis was performed to modify the expression proposed by Bohl and Adebar (2011), as shown in Eq. (6.33). The proposed L_p equation additionally includes effects of strain penetration, and is intended to estimate ultimate lateral displacement. The proposed equation for equivalent plastic hinge length was developed using the proposed analytical model for ultimate lateral displacement of flexural RC walls. The expected failure mode shall be crushing of compressive concrete after yielding of tensile reinforcement. Buckling of longitudinal reinforcement and global boundary buckling is not considered.

$$Lp = (0.4l_w + 0.08h_w)(1 - 1.5\eta) + 0.022d_bf_y \tag{6.33}$$

Where l_w and h_w are the wall length and shear-span, respectively; η is the axial load ratio; d_b and f_y are the longitudinal reinforcement diameter and yield strength, respectively.

6.5.2. Evaluation of existing plastic hinge length equations

The empirical equations available in literature to estimate the plastic hinge length in rectangular walls based on experimental results are shown in Table 6.9. Some of these expressions were initially developed for RC beams and columns. For a given rectangular concrete wall, the plastic hinge length calculations significantly influence the estimation of the force-displacement response of that wall in the inelastic region. In order to obtain an accurate force-displacement relationship from moment-curvature response of a wall section, a realistic value or empirical equation to compute the plastic hinge length is required. The accuracy of the above plastic hinge length equations in predicting ultimate

displacement is the force-displacement behavior of reinforced concrete walls using the proposed equation for ultimate displacement prediction is evaluated using experimental results for rectangular walls given in Table 6.5.

The comparison of estimated ultimate displacements with the experimental values using the different plastic hinge length equations are presented in Figure 6.16. In the figure, mean and standard deviation of the ratio of experimental to analytical ultimate drift is presented for each equation of plastic hinge.

It is shown that all evaluated equations predict the ultimate displacement in a conservative manner. Equation by Paulay and Priestley (1993) and equation given as $L_p = 0.5l_w$ give good estimation with a mean of experimental to analytical ultimate drift of respectively 1.10 and 1.11, respectively, and with a standard deviation of 0.52 and 0.49, respectively. The best estimation is given by using the proposed equation (Eq. 6.33) with a mean and standard deviation of 1.00 and 0.50 respectively.

Although Eq.(1) and Eq.(6) in Table 6.9 simulated well ultimate lateral displacement for RC wall based on data matching, these equations do not physically reflect all influencing parameters. The proposed equation for equivalent plastic hinge length depends on the main factors previously identified as affecting the length of plastic hinge for RC walls (Bohl and Adebar, 2011, Kazaz, 2013). The proposed equation modify the expression proposed by Bohl and Adebar (2011) and is intended to the prediction of the ultimate lateral displacement of RC walls.

Based on experimental database used to validate the proposed equations for ultimate displacement and equivalent plastic hinge length, axial load ratio of $0 \leq P/f'_cA_g \leq 0.3$ and transverse reinforcement ration of $\rho_l \leq 1.2\%$ are added as required conditions.

Table 6.9 – Expressions of plastic hinge length

| Nb.	Reference	Plastic hinge length equation (L_p)
①	Paulay and Priestley, 1993	$0.4l_w + 0.044H_w$
②	Priestley *et al.*, 1996	$0.08H_w + 0.022d_b f_y$
③	Priestley *et al.*, 2007	$\min\left(0.2\left(\dfrac{f_u}{f_y}-1\right),0.08\right)L_s + 0.2l_w + 0.022d_b f_y$
④	Priestley *et al.*, 2007	$\min\left(0.2\left(\dfrac{f_u}{f_y}-1\right),0.08\right)L_s + 0.1l_w + 0.022d_b f_y$
⑤	Panagiotakos and Fardis, 2001	$0.12H_w + 0.014d_b f_y$
⑥	Kowalski, 2001	$0.5l_w$
⑦	Thomson and Wallace, 2004	$0.33l_w$
⑧	EC8 Part 3 (CEN, 2005)	$L_s/30 + 0.2l_w + 0.11d_b f_y/\sqrt{f'_c}$
⑨	Berry *et al.*, 2008	$0.05H_w + 0.1d_b f_y/\sqrt{f'_c}$
⑩	Biskinis and Fardis, 2010	$0.2l_w\left(1+\dfrac{1}{3}\min\left(9,\dfrac{L_s}{l_w}\right)\right)$
⑪	Bohl and Adebar, 2011	$\left(0.2l_w + 0.05H_w\right)\left(1-1.5\dfrac{P}{A_g f'_c}\right) < 0.8l_w$
⑫	Kazaz, 2013	$0.27l_w\left(1-\dfrac{P}{A_w f'_c}\right)\left(1-\dfrac{f_y \rho_{sh}}{f'_c}\right)\left(\dfrac{M/V}{l_w}\right)^{0.45}$
⑬	Aaleti *et al.*, 2014	$0.07H_w\left(1-10e^{-0.6\rho_l}\left(\dfrac{P}{A_w f'_c}\right)\right)+0.15d_b f_y \geq 0.01H_w + 0.15d_b f_y$
⑭	This study	$\left(0.4l_w + 0.044H_w\right)\left(1-1.5\eta\right)\left(1+0.55\rho_s\right)+0.1d_b f_y/\sqrt{f'_c}$
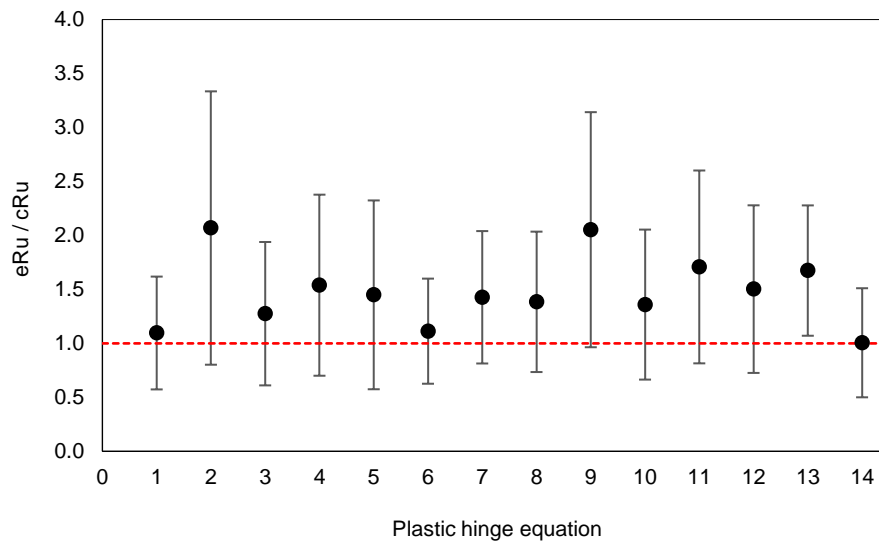
Figure 6.16 – Accuracy of plastic hinges equations for ultimate displacement prediction

6.6. Conclusions

Different numerical methods were used to simulate backbone curves and ultimate displacement of RC walls with confined boundaries. In addition, analytical expression for estimation of ultimate displacement and plastic hinge length were also proposed. From this study, the following conclusions were drawn:

- The built 2D and 3D FE models were able to simulate the entire steps of the nonlinear behavior of the concrete wall such as elastic region, cracking, steel yielding and peak load with relatively good accuracy. 3D model could simulate the ultimate deformation points with very good accuracy; however, the 3D nonlinear FE models are time consuming. Both 2D and 3D FE models predicted the ability of boundary columns in reducing damage level and crack distribution since boundary columns carry a large amount of axial force that reduce axial stress level in wall panels.

- The fiber model based on the plastic hinge length and moment-curvature analysis is an easy and interesting alternative for FE method for simulating the envelop response curve for RC walls with confined boundaries. In this manner, the limit compressive strain proposed by Mander *et al.* (1988) is a good measure for the ultimate drift.

- An analytical equation is proposed to estimate the ultimate displacement of RC structural walls with rectangular cross section. The proposed equation relate the ultimate deformation to main key design parameters that is wall length and shear span, axial load ratio, and transverse reinforcement ratio at confined boundaries. The accuracy of the proposed equation was verified with experimental data and results of fiber analysis. Although the proposed equation did not evaluate the experimental ultimate drift with very high accuracy, it would give a conservative estimation.

- From parametric study using proposed equation for ultimate displacement, a regression analysis was performed to modify the expression proposed by Bohl and Adebar (2011) for plastic hinge length of RC rectangular walls to include effects of transverse reinforcement ratio and strain penetration.

References

1. Aaleti, S., Dai, H., Sritharan, S., (2014), "Ductile Design of Slender Reinforced Concrete Structural Walls", 10th US National Conference on Earthquake Engineering, July 21-25, Anchorage, Alaska.

2. Berry, M., Lehman. D., Lowes, L., (2008) "Lumped-plasticity models for Performance Simulation of Bridge columns", ACI Structural Journal, 105(3): 270-279.

3. Beyer, K., Dazio, A., Priestley, M.J.N., (2011), "Shear Deformations of Slender Reinforced Concrete Walls under Seismic Loading", ACI Structural Journal, 108(2): 167-177.

4. Biskinis, D., Fardis, M.N., (2010), "Deformations at flexural Yielding of Members with Continuous or Lap-spliced Bars", Structural Concrete, 11(3): 127-138.

5. Bohl, A., Adebar, P., (2011), "Plastic hinge lengths in high-rise concrete shear walls", ACI Structural Journal 108(2): 148‑157.

6. CEN (2005) "Eurocode 8: Design of structures for earthquake resistance – Part 3: Assessment and retrofit of buildings," European Standard, European Committee for Standardization, Brussels, Belgium.

7. Ciampi, V., Eligehausen R., Bertero V. V., Popov E. P., (1982), "Analytical model for concrete anchorages of reinforcing bars under generalized excitations", Report No. UCB/EERC82-23, EERC, Berkeley, California.

8. Dazio, A., Beyer, K., Bachmann, H., (2009), "Quasi-static cyclic tests and plastic hinge analysis of RC structural walls", Engineering Structures 31(7): 1556‑1571.

9. Elmorsi, M., Kianoush, M. R., Tso, W. K., (2000), "Modeling bond-slip deformations in reinforced concrete beam-column joints", Canadian Journal of Civil Engineering. 27(3): 490-505, 2000.

10. Filippou, F. C., Popov, E. G., Bertero, V. V., (1982), "Effects of bond deterioration on hysteretic behavior of reinforced concrete joints", EERC Report No. UCB/EERC-83/19, Earthquake Engineering Research Center, University of California, Berkeley.

11. ITOCHU Techno-Solutions Corporation, FINAL/V11, Finite elements analysis program for the nonlinear behavior of concrete structures, 2011.

12. Kazaz, I., (2013), "Analytical study on plastic hinge length of structural walls", Journal of Structural Engineering 139(11):1938‑1950.

13. Kono, S., Obara, T., Taleb, R., Watanabe, H., Tani, M., Sakashita, M. (2015). "Simulation of drift capacity for RC walls with different section configurations". 10th Pacific Conference on Earthquake Engineering, Sydney, Australia, 6-8 November, 181-188.

14. Kowalski, M. J., (2001). "RC structural walls designed according to UBC and displacement-based methods", ASCE structural Journal, 127(5): 506-516.

15. Kupfer, H., Hilsdorf, H. K., (1969), "Behavior of Concrete under Biaxial Stress", ACI Journal Proceedings, 66(8): 656-666.

16. Mander, J. B., Priestley, M. J. N., Park, R., (1988), "Observed Stress-Strain Behavior of Confined Concrete", ASCE Journal of Structural Engineering, 114(8): 1827-1849.

17. Markeset, G., Hillerborg, A., (1995), "Softening of concrete in compression localization and size effects", Cement and Concrete Research, 25(4): 702-708.

18. Massone, L.M., Wallace, J.W., (2004), "Load-deformation responses of slender reinforced concrete walls. ACI Structural Journal 101(1): 103‑113.

19. Naganuma, K., (1995), "Stress-strain Relationship of Concrete under Triaxial Compression", AIJ Journal of Structural and Construction Engineering. 474: 163-170. (in Japanese)

20. Naganuma, K., Yonezawa, K., Kurimoto, O., Eto, H., (2004), "Simulation of nonlinear Dynamic response of Reinforced Concrete Scaled Model Using Three-Dimensional Finite Element Method", Proceedings of the 13th WCEE, Vancouver, Canada, Aug. 1-6, Paper 586.

21. Naganuma, K., (1991), "Nonlinear Analytical Model for Reinforced Concrete Panels under In-Plane Stresses", AIJ Journal of Structural and Construction Engineering, 421: 39-48. (in Japanese)

22. Netrattana C., Taleb R., Watanabe H., Kono S., Mukai D., Tani M., Sakashita S., (2017), "Assessment of ultimate Drift Capacity of RC Shear Walls by Key Design Parameters", Bulletin of the New Zealand Society for Earthquake Engineering, 50(4): 482-493.

23. Ottosen N. S., (1977), "A failure criterion for concrete". Journal of Engineering Mechanics, 103(EM4): 527–535.

24. Paulay., T., Priestley, M.J.N., (1993), Stability of ductile structural walls. ACI Structural Journal 90(4): 385‑392.

25. Paulay, T., Uzumeri, S.M., (1975), "A critical review of the seismic design provisions for ductile shear walls of the Canadian Code", Canadian Journal of Civil Engineering 2: 592‑601.

26. Panagiorakos, T.B., and Fardis, M.N. (2001). "Deformations of Reinforced Concrete Members at Yielding and Ultimate", ACI Structural Journal, (98)2: 135-148.

27. Priestley, M. J. N., Calvi, G. M., & Kowalsky, M. J. (2007). "Displacement-based Seismic Design of Structures". IUSS Press (p. 721).

28. Priestley, M.J.N., Kowalsky, M.J., (1998), "Aspects of Drift and Ductility Capacity of Rectangular Cantilever Structural Walls", Bulletin of New Zealand Society of Earthquake Engineering, 1998.

29. Priestley, M.J.N., Seible, F., Calvi, E.M., (1996), "Seismic Design and Retrofit of Bridges", John Wiley & Sons, New York, 686 pages.

30. Scott, B. D., Park R. Priestley M. J. N., (1982), "Stress-strain behavior of concrete confined by overlapping hoops at low and high strain rates", ACI Journal Proceedings, 79(1): 13-27.

31. Takahashi S., Yoshida K., Ichinose T., Sanada Y., Matsumoto K., Fukuyama H., Suwada H., (2013), "Flexural drift capacity of reinforced concrete wall with limited

confinement", ACI Structural Journal, 110(1): 95-104.

32. Tani, M., Fukuyama, H., and Kono, S., (2012), "Study on Deformation Capacity of R/C Bearing Walls with Rectangular Cross-section Based on Experimental Database", 15th World Conference on Earthquake Engineering, Lisbon. Portugal.

33. Thomsen, J. H. IV and Wallace, J. W., (2004). "Displacement-based design of slender reinforced concrete structural walls - experimental verification" ASCE Journal of Structural Engineering, 130(4): 618-630

CHAPTER 7 SUMMARY, CONCLUSIONS AND RECOMMENDATIONS

This chapter provides a summary of and presents the conclusions from the research described in this dissertation. In addition, possible areas of future work are discussed.

7.1. Summary

Observed damages in reinforced concrete wall buildings following some recent earthquakes raised concerns about the seismic performance of rectangular RC walls with confined boundaries. This research project was initiated following observations on the seismic performance of RC walls in recent earthquakes that have demonstrated the vulnerability of RC rectangular walls. The research was undertaken to study the influence of confinement details in wall boundary on strength and deformation of structural RC walls. In particular, there is concern about the compressive response of confined boundary elements of flexural RC walls.

In accordance with the research need statement above, the broad objective of the dissertation is to, experimentally and analytically; evaluate the seismic behavior of reinforced concrete structural walls with confined boundaries. The research has three specific objectives as follows: (1) experimentally and analytically investigates the influence of different confined boundary elements detailing on their cyclic lateral load behavior, and evaluates and proposes design rules for RC confined boundaries; (2) experimentally investigates the seismic performance of rectangular and barbell shape RC walls with confined boundaries, as well as the potential of numerical simulation using fiber-based sectional models; and (3) Investigates the ultimate displacement capacity of RC walls for performance-based seismic design using fiber-based sectional model and proposed analytical equations

To achieve these objectives, an experimental program included sixteen (16) prism element as isolated confined RC wall boundary, and seven (7) RC wall with confined boundaries, tested with a reversed-cyclic loading protocol.

7.2. Conclusions

The following main conclusions are made based on the research activities summarized above.

7.2.1. Confined boundaries of RC walls

- Dense transverse reinforcement detailing in thin confined boundaries may not improve the performance of walls. Imposing a minimum wall thickness would be an alternative means to suppress failures due to global buckling of thin walls and efficiently use the confinement. It was also shown that failure due to global buckling was affected by both large tensile strain prior to compressive strain and prior crushing of compressive concrete.

- Large transverse reinforcement spacing may result in buckling of longitudinal reinforcement following even limited tensile strain excursions. Intermediate unsupported bars are more susceptible to buckling. Supporting all intermediate bars at the wall confined boundary should be considered.

- Transverse reinforcement index was proposed that takes into account the case of large longitudinal to transverse reinforcing bar diameters. The proposed longitudinal-to-transverse reinforcement index along with the ratio of transverse reinforcement spacing to longitudinal bar diameter present a simple but effective anti-buckling measures of reinforcement. The proposed longitudinal-to-transverse reinforcement index needs to be validated with more experimental data.

- A procedure was proposed for the design and evaluation of RC walls confined boundaries to prevent or evaluate global buckling and reinforcement buckling vulnerabilities.

7.2.2. RC walls with confined boundaries

- Boundary columns can effectively enhance the wall performance by increasing its ultimate deformation capacity and reducing damage level in the wall panel. However, the final failure of walls with boundary columns was more brittle compared to that of rectangular section walls. Damaged regions due to concrete crushing in rectangular walls spread widely over the lower portion of the walls. The damage tended to spread horizontally to the wall center and was limited in height.

- Flexure deformation was continuously dominant for rectangular walls while its contribution of flexural drift increased with the increase of drift ratios for walls with boundary columns. Results showed also that displacement component due to strain

penetration is quite large and might be comparable to the shear component and, hence, should be considered in evaluation of the ultimate displacement.

- A simplified fiber section analysis based on the plastic hinge length and moment-curvature analysis was used to simulate cyclic lateral load-displacement relations for flexure, shear and strain hardening. Results of the simulation showed a very good agreement with experimental results for all drift components. This demonstrated the effectiveness of the empirical equation used to evaluate shear deformation component based on flexural component, as well as the effectiveness of strain penetration used model.

7.2.3. Ultimate displacement of RC walls

- The built 2D and 3D FE models were able to simulate the entire steps of the nonlinear behavior of the concrete wall such as elastic region, cracking, steel yielding and peak load with relatively good accuracy. 3D model could simulate the ultimate deformation points with very good accuracy; however, the 3D nonlinear FE models are time consuming.
- The fiber model based on the plastic hinge length and moment-curvature analysis easy and interesting alternative for FE method for simulating the envelop response curve for RC walls with confined boundaries.
- An analytical equation is proposed to estimate the ultimate displacement of RC structural walls with rectangular cross section. The proposed equation relate the ultimate deformation to main key design parameters that is wall length and shear span, axial load ratio, and transverse reinforcement ratio at confined boundaries. The accuracy of the proposed equation was verified with experimental data and results of fiber analysis. Although the proposed equation did not evaluate the experimental ultimate drift with very high accuracy, it would give a conservative estimation.
- From parametric study using proposed equation for ultimate displacement, a regression analysis was performed to modify the expression proposed by Bohl and Adebar (2011) for plastic hinge length of RC rectangular walls to include effects of transverse reinforcement ratio and strain penetration.

7.3. Recommendations for future research

The research shows that there are gaps in the experimental data for both walls and boundary elements as well as needs for nonlinear simulation. The following recommendations for future work are proposed.

- The database of boundary element tests developed as a part of this study and in the literature evaluated a wide range of detailing parameters. However, still there were some untested parameter values (e.g. effect of testing length, improvement due to restrained intermediate longitudinal bars, horizontal spacing of confining bars). In

addition, the existing database of boundary elements is limited, and therefore a statistical analysis may not specifically be applicable. Enhanced set of boundary element tests is recommended in order to provide enough data to perform statistical analyses, and to further support the proposed transverse reinforcement index.

- The simulated and experimental data show that axial loads has greater effect on the drift capacity of RC walls. The experimental data is relatively limited in terms of higher axial load ratios, and therefore a series of tests investigating the effects of significant axial loads, up to 40%, on wall performance.